Durham E-Theses

Dynamic analysis of long run-out rock avalanches: A view from the Vaigat Strait, West Greenland

BENJAMIN, JESSICA

Dynamic analysis of long run-out rock avalanches: A view from the Vaigat Strait, West Greenland

Jessica Benjamin

Department of Geography

University of Durham

October 2014

Thesis submitted for the degree of Master of Science

Declaration

I confirm that no part of the material presented in this thesis has previously been submitted for a degree in this or any other university. In all cases the word of others, where relevant, has been fully acknowledged.

Jessica Benjamin
University of Durham
October 2014

Cover image: View onto the source area of a large rock avalanche event in Vaigat, West Greenland. The scar is characterised by clear, fresh surfaces and local accumulations of burnt lithologies produced by self-combustion of carbon-rich shales.

Abstract

Risk assessments of the threat posed by rock avalanches conventionally rely upon numerical modelling of potential run-out. Such models are contingent upon a thorough understanding of the flow dynamics inferred from deposits left by previous events. Few records exist of multiple rock avalanches with boundary conditions sufficiently consistent to develop a set of more generalised rules for behaviour. This thesis uses a numerical modelling approach to investigate the emplacement dynamics of 20 adjacent events in Vaigat, West Greenland, which are sourced from a stretch of coastal mountains of relatively uniform geology and structure. Rheological calibration of the numerical flow code *VolcFlow* was performed using a well-constrained event at Paatuut (AD 2000). The best-fit simulation assumes a constant retarding stress with a collisional stress coefficient and simulates run-out to within ±0.3% of that observed. Despite being widely used to simulate rock avalanche propagation, other models, that assume either a Coulomb frictional or a Voellmy rheology, failed to reproduce the observed event characteristics and deposit distribution at Paatuut. This calibration was then applied to 19 other events, simulating rock avalanche motion across 3D terrain of varying levels of complexity. The findings illustrate the utility and sensitivity of modelling a single rock avalanche satisfactorily as a function of rheology, alongside the validity of applying the same parameters elsewhere, even within similar boundary conditions. *VolcFlow* can plausibly account for the observed morphology of a series of deposits emplaced by events of different types, although its performance is sensitive to a range of topographic and geometric factors. These exercises show encouraging results in the model's ability to simulate a series of events using a single set of parameters obtained by back-analysis of the Paatuut event alone, suggesting that first-order run-out prediction is possible.

Acknowledgments

Contents

List of Figures

CHAPTER 5 – METHODOLOGY

CHAPTER 6 – RESULTS

CHAPTER 7 – DISCUSSION

List of Tables

List of Symbols

a	Acceleration	m s^{-2}
A	Area	m^2
c	Shear strength	kg m^{-2}
C	Chézy coefficient	m$^{1/2}$ s^{-1}
g	Gravitational acceleration	m s^{-2}
h	Flow depth	m
h_n	Flow depth (normal)	m
h_v	Flow depth (vertical)	m
H	Vertical drop height	m
$k_{actpass}$	Earth pressure coefficient	-
L	Total travel distance (maximum run-out)	m
m	Mass	kg
n	Manning roughness coefficient	m$^{1/3}$ s^{-1}
r_u	Pore-pressure ratio	-
t	Time	s
T_0	Cohesion	kg m^{-1} s^{-2}
u	Pore fluid pressure at the base of the flow	kg m^{-1} s^{-2}
v	Flow velocity	m s^{-1}
v_d	Depth-averaged flow velocity	m s^{-1}
v_m	Mean velocity	m s^{-1}
v_x	x-component of the flow velocity	m s^{-1}
v_y	y-component of the flow velocity	m s^{-1}
V	Volume	m^3
z	Surface elevation	m
Δ	Normalised index	-
α	Local ground slope	°
β	Fahrböschung angle ($= \tan^{-1} H/L$)	°
ϕ	Dynamic basal friction angle	°
η	Dynamic fluid viscosity	kg m^{-1} s^{-1}
φ_{bed}	Bulk friction angle	°
φ_{int}	Internal angle of friction	°
μ	Coefficient of friction ($= \tan\varphi_{int}$)	°

$\boldsymbol{\theta_z}$	Horizontal azimuth of the local ground slope	°
$\boldsymbol{\rho}$	Bulk density of the landslide and path material	kg m^{-3}
$\boldsymbol{\sigma}$	Normal stress	kg m^{-1} s^{-2}
$\boldsymbol{\sigma_z}$	Total normal stress	kg m^{-1} s^{-2}
$\boldsymbol{\sigma_z'}$	Effective bed normal stress at the base of the landslide	kg m^{-1} s^{-2}
$\boldsymbol{\tau}$	Basal shear stress	kg m^{-1} s^{-2}
$\boldsymbol{\tau_{yield}}$	Threshold yield stress	kg m^{-1} s^{-2}
$\boldsymbol{\xi}$	Collisional stress coefficient	-
∇	Gradient operator	-

Chapter 1

Introduction

Long run-out rock avalanches constitute one of the most hazardous geomorphic processes. Also known as rockslide-avalanches (Mudge, 1965), rockfall avalanches (Crandell *et al.*, 1974) or sturzströms (Heim, 1882; Hsü, 1978), they are one of a number of forms of massive rock-slope failure (MRSF). Other forms of MRSF include rockfalls, rockslides, deep-seated gravitational bedrock landslides, large submarine landslides, and syn-eruptive flank collapses of volcanoes (Evans *et al.*, 2006). Rock avalanches result from catastrophic rock-slope failure, and are so-named to emphasise the post-failure phenomena of rapid and excessive run-out (observed or inferred velocities can exceed 100 m s^{-1}) and subsequent emplacement of large volumes (> 1x10^6 m^3) of intensely fractured rock over distances commonly five to ten times the total fall height (Hewitt *et al.*, 2008). Notable examples include the Elm rock avalanche in the Swiss Alps, Frank Slide in the Canadian Rockies, Blackhawk in the Californian San Bernardino Mountains, and the largest known terrestrial (non-volcanic) rock avalanche: the pre-historic Saidmarreh event in the Zagros Mountains of Iran (Table 1.1).

Table 1.1) Characteristics of several well-known rock avalanche events.

Name	Year	Volume (x10^6 m^3)	Inferred velocity (m s^{-1})	Reference(s)
Blackhawk, California	ca. 10-55 ka	300	118	Shreve (1968)
Saidmarreh, Iran	ca. 9 ka	38,000	100	Harrison and Falcon (1938)
Elm, Switzerland	1881	10-11	70	Heim (1882; 1932)
Frank, Canada	1903	30	49	McConnell and Brock (1904)

The exceptional run-out of rock avalanches represents a conspicuous divergence from the physics described by simple frictional models of granular motion, which assume that the shear stress at the base of a granular flow is proportional to the normal stress (Savage and Hutter, 1989). Frictional models are widely used to explain the mobility of small-scale landslides, and so the unusual behaviour of rock avalanches has thus been the subject of considerable debate (Hsü, 1975). This apparent decrease in frictional resistance is commonly attributed to the internal dynamics of rock avalanches, although the underlying mechanisms responsible remain contentious (Legros, 2003), with a number of theories having been proposed. This constitutes one of several unique features of rock avalanches, which can be briefly summarised as follows:

1. Run-out exceeds that predicted by simple frictional models, with rock avalanche mobility increasing with volume (Corominas, 1996);

2. Despite being intensively comminuted, the source stratigraphic sequence tends to be

remarkably well-preserved in rock avalanche deposits (Hewitt, 2002), meaning that specific units and their shear histories can in theory be directly traced back through the deposit (Dunning, 2006);

3. The complex surface morphologies (e.g. a coarse clastic carapace) and distinctive features (e.g. patterns of reflection and refraction) characteristic of rock avalanche deposits allow an insight into their emplacement dynamics (Smith *et al.*, 2006).

The distinctive dynamics, landforms and hazards involved in catastrophic rock-slope failure not only exert a significant influence upon landscape development but they can also be devastating, and mitigating this risk requires contributions from a range of scientific disciplines.

1.1 Geomorphic significance of rock avalanches

Catastrophic rock-slope failures exert a major and long-lasting influence on landscapes by virtue of their ability to mobilise large volumes of material (Fischer *et al.*, 2012a), thereby limiting topographic relief and modulating sediment flux (Fort and Peulvast, 1995; Korup, 2006). Rock avalanches can also choke fluvial systems through blocking or saturation of loose material, which can represent a substantial long-term imprint upon orogens and their evolution (Korup *et al.*, 2007). The long-term geomorphic significance of catastrophic rock-slope failures has come under increased scrutiny in recent years owing to the reinterpretation of a number of deposits formerly attributed to glacial deposition as rock avalanche deposits (e.g. Wright, 1998; Hewitt, 1999; Fort, 2000; Shulmeister *et al.*, 2009; Kirkbride and Winkler, 2012; Ostermann *et al.*, 2012; Reznichenko *et al.*, 2012a). In addition, many deposits are poorly preserved owing to their frequent emplacement in narrow valleys or onto glacier surfaces, where they are subsequently modified or completely removed (as in the Southern Alps and the St. Elias Mountains; Whitehouse and Griffiths, 1983; Spotila *et al.*, 2004), as well as their tendency to occur in regions of high precipitation, uplift and denudation (as in the Himalayas; Burbank *et al.*, 1996). It has therefore been suggested that such events have been systematically under-sampled, particularly in areas of mountainous terrain, leading to suggestions that their role is probably much more significant than is currently believed (Hewitt *et al.*, 2008).

1.2 Rock avalanches as a geohazard

Rock avalanches occur with a measurable frequency in mountainous regions (ca. 1 yr^{-1}), and have been responsible for some of the most destructive natural disasters in recent history (Evans, 2006). In particular, glacier retreat in the Cordillera Blanca, Peru, has triggered some of the deadliest rock avalanches, including the 1970 Huascarán rock-debris avalanche, which is estimated to have caused up to 25,000 fatalities (Keefer and Larsen, 2007). This event is thought to represent the deadliest landslide disaster in history (Evans *et al.*, 2009). Notable more recent examples include the Hattian Bala rock avalanche triggered by the 2005 Kashmir earthquake, which is thought to have accounted for ca. 4% (700) of the deaths caused by coseismic landsliding (Dunning *et al.*, 2007), as well as the 2006 Guinsaugon landslide in Leyte, the Philippines, which buried a village and resulted in 1,119 fatalities (Catane *et al.*, 2008). Today, a number of rock avalanche deposits are densely populated, including that at Flims, Switzerland (ca. 8.2 ka; von Poschinger *et*

al., 2006), raising important questions about the potential severity of future catastrophic rock-slope failures in these regions.

The consequences of rock avalanches can often be more far-reaching and severe than the events themselves, with far-field hazards such as dam breach and, where they run-out into water, tsunami, posing a much more extensive risk. The displacement waves generated by rock avalanches that enter water bodies in narrow fjords or confined bays are particularly destructive (Evans *et al.*, 2006), and represent a major natural hazard for coastal communities in the fjord regions of New Zealand (Dykstra, 2013), Norway (Olesen *et al.*, 2004), British Columbia (Murty, 1979; Bornhold *et al.*, 2007), Alaska (Miller, 1960), Chile (Sepúlveda and Serey, 2009), and Greenland (Dahl-Jensen *et al.*, 2004). One of the best-known historical examples of an impact tsunami occurred in Lituya Bay, Alaska, following a M_w 7.7 earthquake along the Fairweather Fault in 1958 (Miller, 1960). The earthquake triggered a 30×10^6 m^3 rock avalanche, which generated a displacement wave that reached a height of ca. 100-150 m, and ran up the opposite mountainside to an elevation of over 500 m, constituting the highest wave run-up in recorded history (Weiss *et al.*, 2009).

Large-scale, on-going deformation can often be a precursor to catastrophic rock-slope failure. This is currently being witnessed at a number of rock-slopes, most notably in Storfjorden, western Norway, where the $30-40 \times 10^6$ m^3 Åknes rockslide has been continuously moving at rates of up to 10 cm yr^{-1} for over 40 years (Jaboyedoff *et al.*, 2011). The unstable slopes in the Norwegian Fjord represent a major threat for coastal communities with three major rock avalanche-generated tsunami events having occurred in the last century, causing 174 fatalities (Blikra *et al.*, 2006). Considerable emphasis has therefore been placed on quantifying the associated risks of actively deforming rock-slopes, such as Åknes, based on the identification and monitoring of potential failures, estimation of rockslide properties and the modelling of slope stability, potential run-out, wave propagation and run-up using a combination of laboratory models and mathematical simulations (e.g. Blikra *et al.*, 2005; Willenberg *et al.*, 2009; Gigli *et al.*, 2011).

1.3 Risk assessments and the role of numerical modelling

Risk assessments of the future threats posed by possible rock avalanches rely upon numerical modelling of slope stability, potential run-out and tsunami propagation. This is contingent upon a thorough understanding of the emplacement dynamics and rheology inferred from deposits left by previous events (Rickenmann, 2005). However, the poor preservation of deposits and infrequent occurrence of rock avalanches often confutes the validation of models (Korup *et al.*, 2007). This is compounded by difficulties in simulating the complex behaviour of the rock avalanche mass during propagation, where successful modelling is reliant upon the selection of appropriate approximations of the emplacement dynamics and rheology (Pirulli and Mangeney, 2008). In addition, there exist few records of multiple rock avalanche events with boundary conditions sufficiently consistent to permit sensitivity analysis to changes in key variables. As a result, most research involving numerical modelling to date has consisted of the back analysis of individual events. This approach only provides a broad envelope of rheological properties unsuited to predictive scenario modelling, thereby precluding the development of a set of more generalised rules for behaviour across events in different settings (Evans *et al.*, 2006).

1.4 Vaigat, West Greenland: A natural laboratory for investigating rock avalanche dynamics

A unique cluster of 20 large rock avalanche deposits in the Vaigat Strait, West Greenland, offers an unparalleled opportunity to model a large sample of rock avalanches over a short stretch of coastline (ca. 25 km) of relatively uniform geology and structure. Unlike past events in other settings, the rock avalanches in Vaigat are characterised by their simple and unrestricted run-out, both on land and into water, permitting direct comparison of deposits from events of different sizes and ages. In particular, a tsunamigenic rock avalanche that occurred at Paatuut (AD 2000) represents one of the best-documented events of its type, and is therefore well-suited for calibration of numerical models by back-analysis (Pedersen *et al.*, 2002; Dahl-Jensen *et al.*, 2004). As many of the key variables are constant between Paatuut and neighbouring failures, it is then possible to investigate the variations in dynamics and emplacement style related to changes in landslide volume, drop height and thinning/spreading by applying this calibration to other events (Pedersen *et al.*, 2002; Dahl-Jensen *et al.*, 2004).

1.5 Research aims and questions

The research presented in this thesis aims to increase our understanding of rock avalanche dynamics by considering a suite of well-preserved analogous rock avalanche deposits with comparable boundary conditions. This will be used to undertake a sensitivity analysis of run-out uniquely validated by a proximal population of rock avalanche deposits, which will be achieved by back-analysing a well constrained event for model calibration before applying these parameters to a series of neighbouring failures. This aim will be achieved by addressing the following set of research questions:

RQ1) **What are the characteristics of rock avalanche run-out in the Vaigat Strait?**

RQ2) **How suitable are simple rheological laws for simulating rock avalanche run-out in Vaigat?**

RQ3) **Can a single set of rheological parameters successfully reproduce the dynamics of a series of events emplaced within comparable morphological and geophysical conditions?**

RQ4) **What factors have the most influence on model performance?**

1.6 Thesis structure

In this thesis, I focus on the propagation mechanisms and mobility of a series of rock avalanches in Vaigat, West Greenland. Specifically, I investigate the utility of modelling a single rock avalanche satisfactorily as a function of rheology, alongside the validity of applying the same parameters elsewhere. The thesis comprises seven chapters following the Introduction.

Chapter 2 gives an overview of the Quaternary glacial history and relative sea-level change in the Vaigat Strait, West Greenland. This chapter describes the geology of the surrounding

Nuussuaq basin and discusses mechanisms of paraglacial rock-slope failure and its role in modulating post-glacial sediment fluxes. Evidence of rock avalanching in the area is presented and the recent tsunami-generating rock avalanche at Paatuut is described. The chapter concludes by describing the uniqueness of this site and its importance for this research.

Chapter 3 discusses the current state-of-knowledge on long run-out rock avalanches and their emplacement dynamics, avalanche-substrate interactions and the geomorphological and sedimentological characteristics of their deposits.

Chapter 4 briefly reviews a number of numerical approaches to modelling the post-failure behaviour of rock avalanches discussed in *Chapter 3*. The use of simple rheological laws to govern the motion and run-out of mass movements in these models is discussed and the mathematical expressions of several commonly used laws are given. The chapter concludes by identifying one continuum dynamic model in particular, *VolcFlow*, which has shown particularly encouraging results in its ability to demonstrate process representation and is therefore used later in this work.

Chapter 5 outlines the successive pre-, syn- and post-processing steps required to back-analyse the Paatuut event using *VolcFlow*. This is followed by a summary of the methods used to apply this calibration to a series of other rock avalanche events in the Vaigat Strait.

Chapter 6 presents the results of the calibration and modelling procedures outlined in *Chapter 5*. This chapter first describes the characteristics of rock avalanche run-out in Vaigat, before presenting the results of the rheological calibration undertaken using data from the Paatuut event. The ability of the model to simulate a series of events of variable volumes, run-out and stalling characteristics using a single set of parameters is then assessed.

Chapter 7 discusses the results presented in *Chapter 6* with regards to the use of simple rheological laws in numerical run-out models and their implications for model requirements. The implications of these results for forward modelling and for the incorporation of numerical run-out models into a risk assessment framework is also discussed, placing particular emphasis on their implications for tsunami hazard and risk assessments.

Chapter 8 summarises the major findings of this work and discusses directions for future research.

Chapter 2

Rock avalanches in West Greenland

The north Vaigat coast, West Greenland, constitutes a unique geophysical setting that has generated a cluster of 20 large rock avalanche deposits. This offers the unprecedented opportunity to model a series of rock avalanches along a short stretch of coastal mountains (ca. 25 km) of relatively uniform geology and structure. In addition, Vaigat provides an unparalleled test-bed for assessing paraglacial slope response as the Greenland Ice Sheet retreats and rock-slopes are debuttressed. This chapter introduces the study site in *Section 2.1* and gives an overview of the stratigraphic succession of the surrounding Nuussuaq Basin, conditions thought to be favourable to the generation of rock avalanches. The Quaternary glacial history and relative sea-level change in the area is also described before discussing mechanisms of paraglacial rock-slope failure and its role in modulating post-glacial sediment fluxes. In *Section 2.2*, the history of rock avalanching in the area is outlined before focussing on the recent tsunami-generating rock avalanche at Paatuut (AD 2000), which constitutes an important case study later in this research.

2.1 Regional setting

2.1.1 Geology

In most parts of Greenland, where gneisses and granites dominate, the relative strength of rock-slopes means that they are not conducive to catastrophic failure (Pedersen *et al*., 1989). By contrast, the stratigraphic succession in the Nuussuaq Basin, central West Greenland, comprises weakly consolidated sedimentary rocks such as sandstones interbedded with shales, which are overlain by a layer of dense basalts (Fig. 2.1). Due to local uplift during the Neogene (ca. 23.03-2.58 Ma), the Nuussuaq Basin represents the only exposed Cretaceous-Palaeocene (ca. 145-56 Ma) sedimentary basin in West Greenland (Dam *et al*., 2009). The succession along the Vaigat Strait comprises hyaloclastite breccias and subaerial lava flows of the Palaeocene Vaigat and Maligât formations that overlie siliciclastic sediments of the Cretaceous Atane and the Danian Quikavsak formations (Pedersen and Pulvertaft, 1992; Dam and Sønderholm, 1998). The presence of dense, hard basalts underlain by weakly consolidated sedimentary rocks is favourable to the generation of landslides, rockfalls and rock avalanches in this area (Fig. 2.1), especially where erosion exposes the underlying soft units and rock-slope deformation is not inhibited by buttressing afforded by rock or glaciers (Strom, 2004).

2.1.2 Quaternary glacial history and relative sea-level change

The Vaigat Strait constituted a major northern drainage route for ice flowing from the Greenland Ice Sheet during the last glaciation (Long and Roberts, 2003). Its morphology therefore represents that of a typical glaciated fjord, with a U-shaped cross-section and depths reaching over
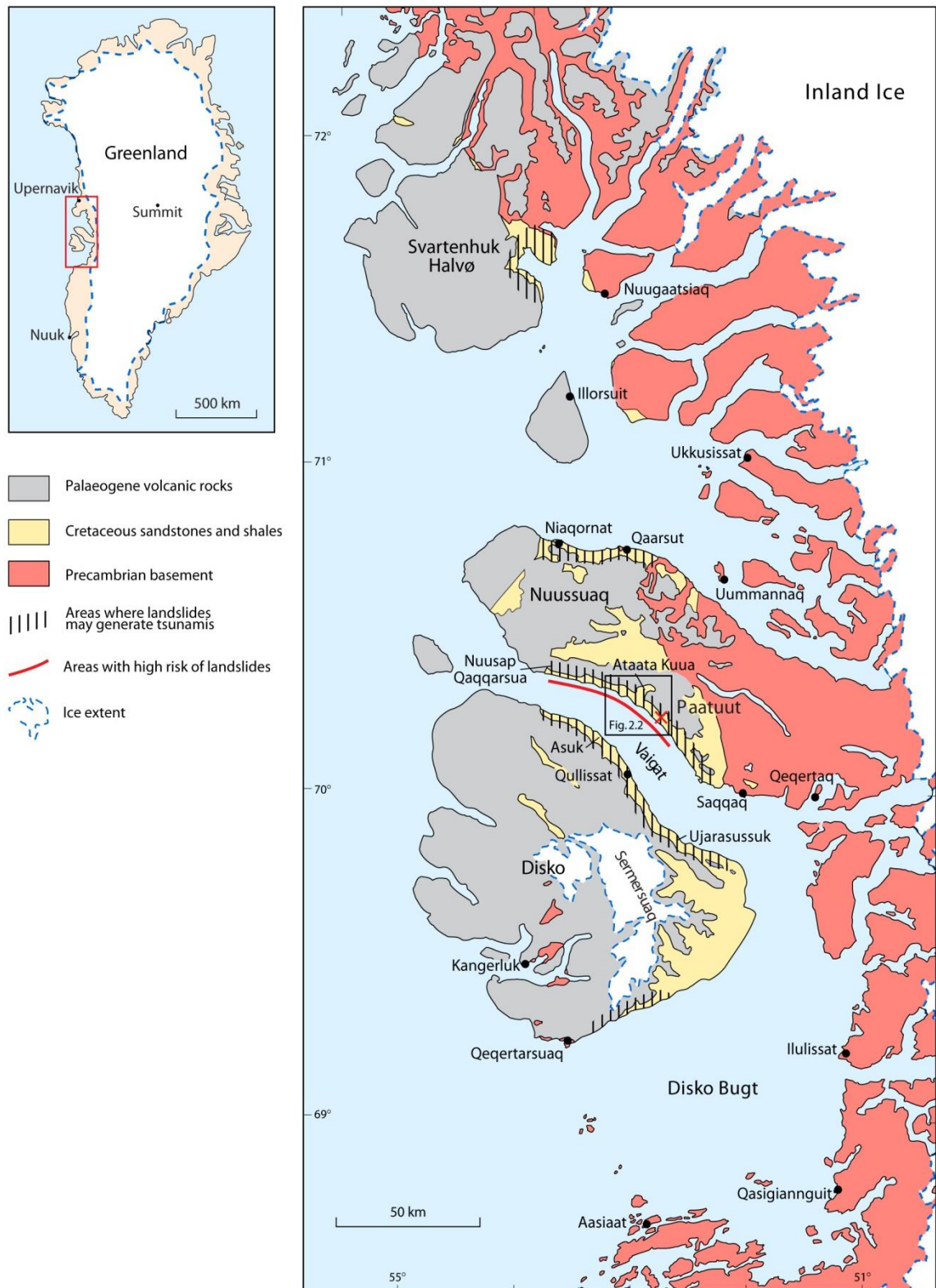
Figure 2.1) Geological map of the Nuussuaq basin with areas prone to rock-slope failure indicated. The basin comprises weakly consolidated sedimentary rocks, such as Cretaceous sandstones and shales, overlain by a thick pile of dense, Palaeogene volcanic rocks. This stratigraphical succession is favourable to (catastrophic) rock-slope failures. As a consequence, large parts of Disko, Nuussuaq and Svartenhuk Halvø are affected by landslides and rock avalanches. Adapted from Pedersen *et al.* (2002).

600 m in its south-eastern part (Hogan *et al.*, 2012). At the Last Glacial Maximum (LGM), the margin of the Greenland Ice Sheet extended to the shelf break where it remained until the early Holocene when it then began to retreat, depositing Quaternary sediments several hundred metres thick into the Vaigat Strait (Denham, 1974). The retreat of the Ice Sheet is thought to have occurred in two stages, with initial retreat driven by sea-level rise (Weidick and Bennike, 2007). This caused the calving of ice grounded below sea-level and retreat of the ice sheet from the continental shelf, with relative sea-level (RSL) falling rapidly during the early Holocene and reaching close to the present coastline by ca. 10 ka BP (Funder and Hansen, 1996). Driven by surface melting, the ice sheet then retreated to a position inland of the present margin, reaching its minimum post-LGM volume by the end of the Holocene thermal optimum (ca. 5 ka BP; Simpson *et al.*, 2009). During the mid-Holocene, RSL fell at rates of 10-30 m ka^{-1} to levels below present before beginning to rise to the present level in the Late Holocene (ca. 3 ka BP), a development that largely reflected a direct isostatic response to the ice-margin history (Long *et al.*, 2011). Mass balance observations of the Greenland Ice Sheet show that it is currently undergoing rapid change (e.g. Rignot and Kanagaratnam, 2006; Holland *et al.*, 2008; Joughin *et al.*, 2008; Rignot *et al.*, 2011), which may be a response to regional warming or natural variability in ice sheet behaviour (Roberts *et al.*, 2009).

2.1.3 Paraglacial rock-slope deformation and failure

The potential response of rock-slope stability to climate change, particularly at high latitudes, has generated a considerable amount of interest, although relatively little research has been undertaken to date (Deline, 2009; Allen *et al.*, 2011). The majority of cases indicate that large (>10^6 m^3) post-glacial failures occurred some thousands of years after ice retreat (McColl, 2012). This lag-time has been attributed to the dynamic adjustment of rock-slopes to glacial debuttressing through gradual stress-redistribution (Ballantyne, 2002). However, whether these progressive processes of rock-slopes alone can sufficiently explain these lag-times is contentious, with some researchers instead suggesting that these slopes remain in a state of critical stability for a long time following deglaciation before being driven to failure by seismic or climatic processes (see McColl, 2012 for a review). For example, one potential factor is enhanced seismicity resulting from regional glacio-isostatic rebound (Bungum *et al.*, 2010). Although this link is widely accepted in the literature, it is unlikely to play a major role in Vaigat, which is characterised by a sparse record of seismic activity (Voss *et al.*, 2007). Catastrophic rock-slope failures are also known to have a causal link with climatic change at various temporal scales, including extreme rainfall events, melting of snow and ice and permafrost degradation (Gruber and Haeberli, 2007). These processes are particularly relevant in Vaigat, where rock avalanches are known to be influenced by permafrost, glacial ice, high topographic relief and repeated freezing and thawing (Pedersen *et al.*, 1989).

Certainly, many historic rock avalanches have sources on slopes that were, until recently, supported by glacier ice (e.g. Fischer *et al.*, 2006; Geertsema *et al.*, 2006; Huggel *et al.*, 2010; Allen *et al.*, 2011). The potential association between glacial debuttressing and catastrophic rock-slope failure therefore raises important questions about the frequency of rock avalanching on steep, unstable alpine slopes as glaciers continue to retreat in the future (Hewitt *et al.*, 2008). Widespread rock-slope destabilisation following deglaciation has significant implications for rock avalanche

hazard, understanding long-term erosion rates, paraglacial sediment budgets and landscape evolution (Kargel *et al.*, 2013). The length and reach of the Vaigat Strait from the Greenland Ice Sheet therefore provides an unparalleled test-bed for assessing paraglacial slope response as the ice sheet retreats and rock-slopes are debuttressed.

2.2 Rock-slope instability in the Vaigat Strait

2.2.1 Rock avalanche history

As discussed in *Section 2.1*, the stratigraphic succession in Vaigat is favourable to the generation of rock avalanches, especially where erosion exposes the underlying, weakly consolidated rocks of the Atane Formation and the rock-slopes are not buttressed by hard rock or glaciers. Field observations and aerial photographs taken in 1985 (scale 1:150,000) show that the north Vaigat coast is characterised by a series of 20 large rock avalanche deposits that have been generated over a small area (ca. 25 km of coastline) of relatively uniform geology and structure (Fig. 2.2). None of the deposits show glacial reworking and their superimposition over the underlying Quaternary cover indicates that they post-date the last glaciation. The deposits are likely to be younger than ca. 3 ka based upon their stratigraphic relationship with sea-level markers such as marine terraces and raised beaches (Pedersen *et al.*, 2002), which were formed during the mid-Holocene when RSL fell (*Section 2.1.2*). Active faulting in Vaigat is minimal with only limited seismicity (Voss *et al.*, 2007), suggesting that the rock avalanches in this area are more likely to have been triggered by progressive deformation of the valley side-walls in response to glacial over-steepening, as discussed in *Section 2.1.3*.

A number of source areas are characterised by self-combustion of carbon-rich shales in the Atane Formation, producing local accumulations of brick-red, hard and fissile burnt lithologies (Fig. 2.3a). In most cases spontaneous combustion is reported ca. 1 year after the event, when the slipped shales have been exposed to the atmosphere long enough for exothermic oxidation reactions to take place and provide heat for combustion (Henderson, 1969). These lithologies are prominent at Paatuut and Ataata Kuua (Fig. 2.1), and indicate a high frequency of landslides (Dam *et al.*, 2009). The 20 events are characterised by variable failure volumes, run-out and stalling characteristics, with some halting on or above topographic benches (Fig 2.3b) or alluvial fans, some running out to sea level and some collapsing into the sea, thereby generating tsunami (Fig. 2.3c). The landscape north-west of Paatuut is characterised by large tongues of blocks, stones and fines that can be seen from the coastline (Fig. 2.2). A number of the deposits are relatively younger with sharper, more well-defined morphologies, with steep terminals (Fig. 2.4a) and a carapace of coarse, clastic material (Fig. 2.4b). The surfaces of these deposits are well preserved and highly textured, with extensive fields of small, conical mounds ('molards') and longitudinal pressure ridges (Dahl-Jensen *et al.*, 2004). These features have sometimes been associated with the incorporation of ice into the flow, either within the failing rock-ice mass itself or through frictional heating of any ice entrained from the basal substrate (Huggel *et al.*, 2005). In a number of cases, such as at Paatuut, the source stratigraphic sequence has also been preserved in the corresponding deposit (Fig. 2.4c).

Seismic profiles in Vaigat show chaotic local accumulations of sediment, which have been interpreted as the deposits of old submarine slides or subaqueous aggradations from subaerial rock
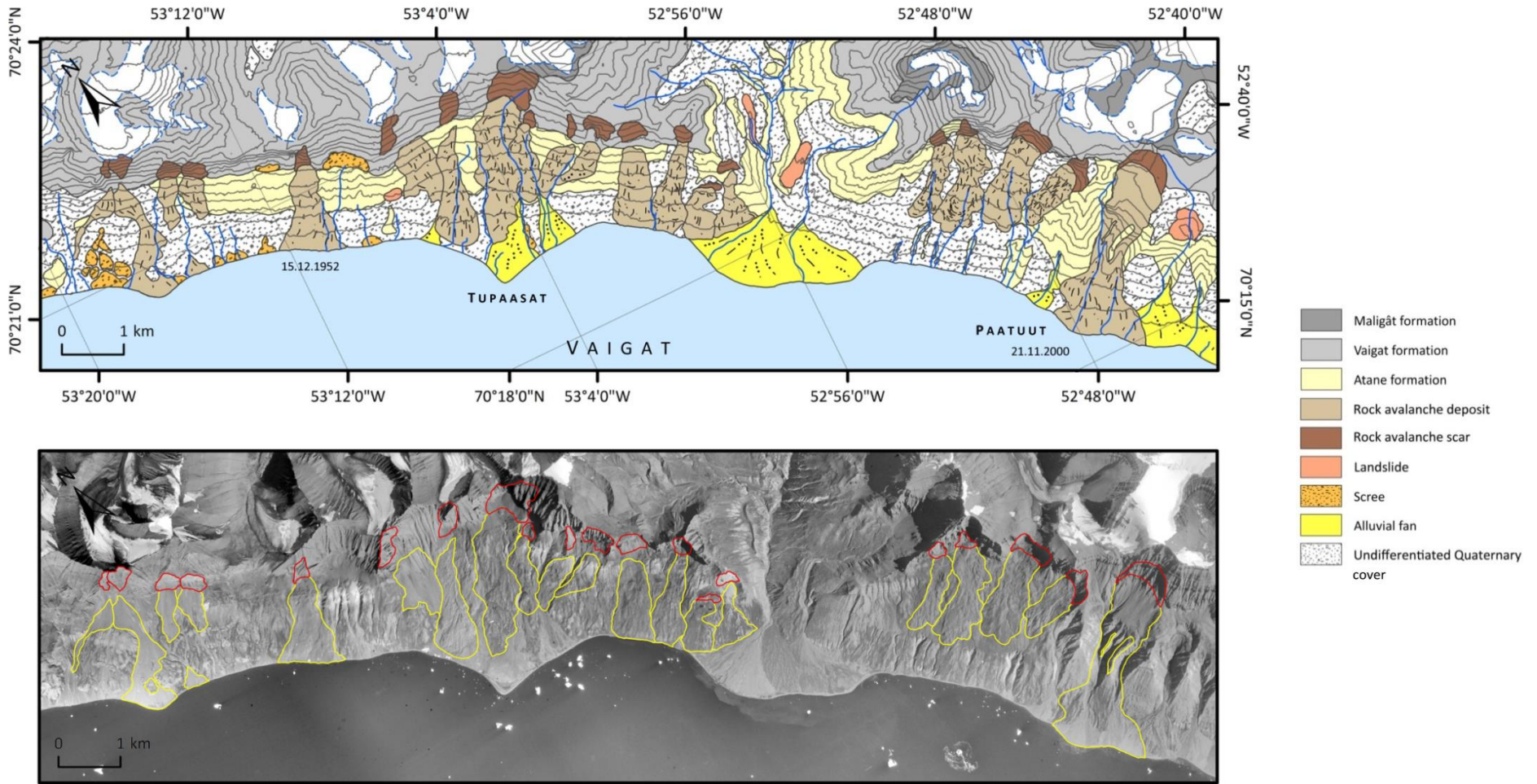
Figure 2.2) Top – map of the south coast of Nuussuaq, West Greenland, showing 20 large rock avalanche deposits. The events occur over a short length of coastline (ca. 25-30 km) of relatively uniform geology and structure. Contours are drawn in 100 m intervals from the 25 m GIMP DEM (Howat *et al.*, 2014). Bottom – vertical aerial photographs taken in 1985 (scale 1:150,000) showing the mapped rock avalanche deposits (yellow) and their source areas (red).

Figure 2.3) a) View onto the source area of event 4. The scar is characterised by clear, fresh surfaces and burnt lithologies (A). The scar measures approximately 600 m in height and has a maximum width of ca. 500 m, **b)** view onto event 2 (white dashed line), which stalled on a topographic bench ca. 350 m above sea level. Scar dimensions are ca. 400 x 350 m, and **c)** view ca. 100 m offshore looking onto the deposit at Paatuut (white dashed line). The rock avalanche initiated ca. 1,000-1,400 m above sea level and ran out over 4 km. The toe of the deposit collapsed into the sea, leaving a steep escarpment ca. 25 m in height (B) and generating a tsunami. Source areas are delimited with red dashed lines.
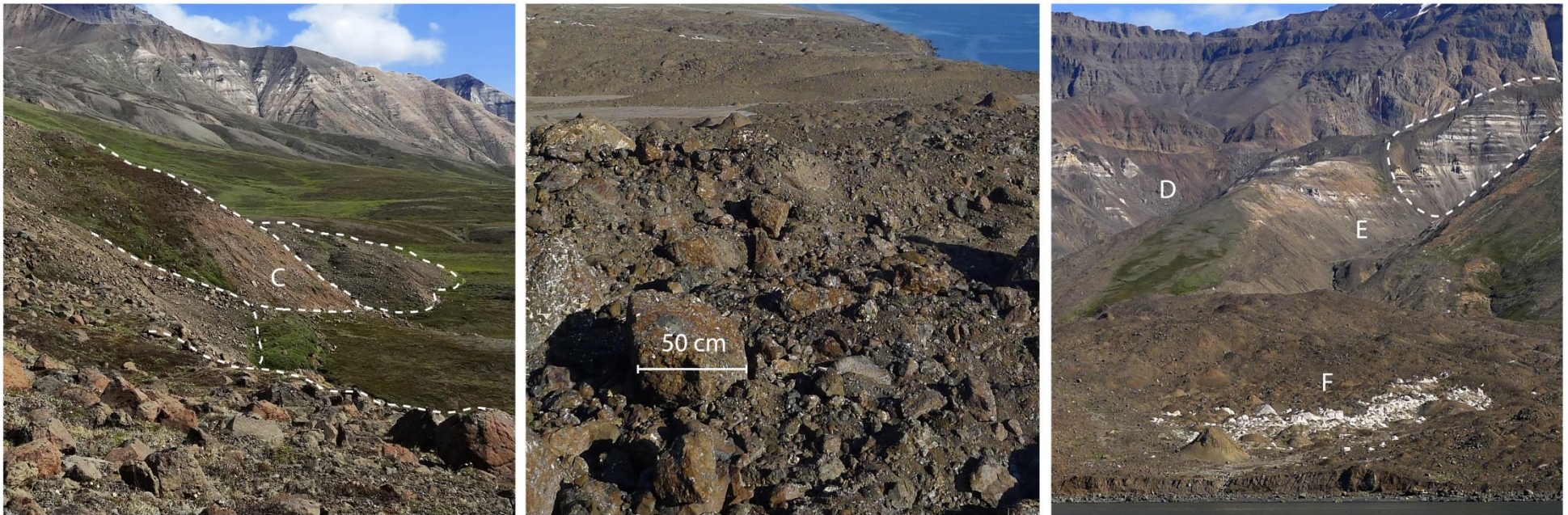
Figure 2.4) a) Lobate deposits emplaced by event 4 (white dashed line). Near their terminations the deposits are thick, standing ca. 3-4 m high, and have slopes close to the angle of repose (C), **b)** view onto the surface of the deposit at Paatuut, which is covered by a carapace of coarse, clastic material, and **c)** view offshore looking onto the deposit at Paatuut. Of particular note is the superelevation of the flow down through the two adjacent gullies (D and E). There are also several areas (F) in the distal reaches of the deposit that have preserved the stratigraphy of the Atane Formation at ca. 600-800 m above sea level (white dashed line). Source areas are delimited with red dashed lines.

The main escarpment at Paatuut comprises two steep (ca. 60°) release surfaces that meet at a high angle, ca. 1,400 m above sea level (a.s.l). The eastern escarpment surface is thought to be a pre-existing fault plane where repeated freeze-thawing in the days prior to the event caused instantaneous fracturing, triggering a large rockfall (Dahl-Jensen *et al.*, 2004). The mechanism by which the rockfall transformed into a rock avalanche is unknown, although it may have involved lubrication of the falling rock mass by black shales and/or snow. At the base of the escarpment lies a platform (800-900 m a.s.l; Fig. 2.6), which was covered in glacial drift prior to the event. Field observations made by Pedersen *et al.* (2002) indicate that the platform is now strewn with large blocks (some > 10 m in height), chaotic accumulations of material and frost mounds. Following the initial collapse, the material was channelled through two deeply incised gullies in the Atane Formation (ca. 300-900 m a.s.l; Figs. 2.5 and 2.6), where it has been suggested that a combination of grain flow and debris flow processes prevailed during transport (Pedersen *et al.*, 2002). The material was then deposited on an alluvial fan below ca. 300 m a.s.l. where it aggraded to depths of up to 60 m. Blocks of all the volcanic and intrusive lithologies described in *Section 2.1.1* have been recognised in the deposit. The subaerial part of the deposit terminates at a steep escarpment (ca. 37°) where ca. 30×10^6 m^3 of material collapsed into the sea (Fig. 2.5). The resultant tsunami caused heavy damage in the coastal areas of Vaigat, partially inundating the then abandoned mining town of Qullissat 20 km across the Strait (Fig. 2.1).
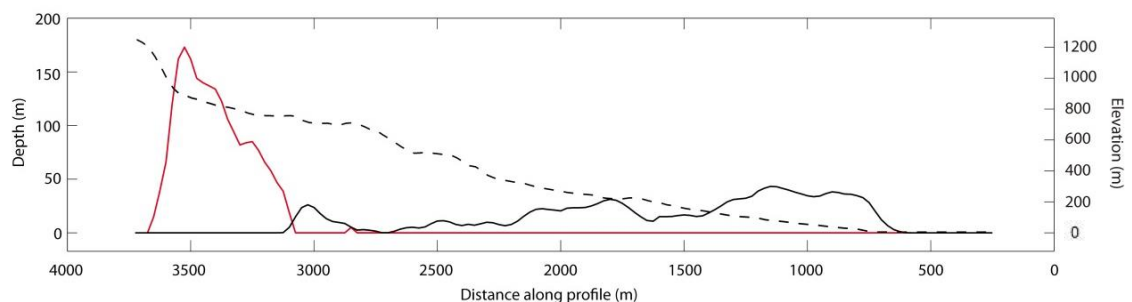
Figure 2.6) Longitudinal transect through the deposit at Paatuut, trending from NE-SW. The transect shows the elevation of the path topography (black dashed line) and the vertical depth profiles of the source mass (solid red line) and deposit (solid black line). Profiles were taken using the Greenland Ice Mapping Project DEM, which has an overall RMS error of ±9.1 m (Howat *et al.*, 2014).

The cold climate and remote nature of this environment means that evidence for the rock avalanche and corresponding tsunami remains remarkably well preserved. In addition, three broadband seismic stations positioned at Qeqertarsuaq (Fig. 2.1), Upernavik (ca. 250 km to the north of Paatuut) and Summit (ca. 550 km to the east) registered two seismic signals generated at Paatuut, the first of which resulted from the initial collapse with the second, stronger signal reflecting the surface waves generated by the movement of the rock avalanche (Pedersen *et al.*, 2002). These data indicate that the main event lasted for ca. 80 s. Owing to these records, the event at Paatuut is one of the best-documented events of its type. In addition, the boundary conditions (e.g. morphological and geophysical characteristics) at Paatuut are well constrained, which presents an excellent opportunity for calibration of numerical models by back-analysis and for further testing the use of a numerical modelling approach for investigating the emplacement dynamics of these events.

avalanches (Marcussen *et al.*, 2001). The majority of the sediments are from the southern coast of Nuussuaq and are known to exceed 200 m in thickness in some places (Pedersen *et al.*, 2002). Rock avalanches that enter water bodies in narrow fjords or confined bays are particularly destructive as the resulting displacement wave may cause large oscillations, leading to a series of incident waves (Evans *et al.*, 2006). The material flux at the point of entry into the water determines the magnitude of this wave, as the rock avalanche must almost instantly displace large volumes of water to generate a tsunami (Harbitz *et al.*, 2014). This condition is more likely to be satisfied along steep coastlines such as the southern coast of the Nuussuaq peninsula where erosion rates are rapid (Humlum, 1992). Several tsunamigenic rock avalanches have occurred in Vaigat including an event in 1952, which generated a tsunami that inundated areas 50-100 m from the shoreline on the northern coast of Disko Island, and the AD 2000 event at Paatuut (*Section 2.2.2*).

The majority of the rock avalanches in Vaigat are sourced from generally uniform lithologies and are characterised by open slope run-out zones, both on land and into water, permitting direct comparison of deposits of events of different sizes and ages. These diverse emplacement 'styles' may result from variable failure modes and mechanisms, volumes, drop heights and thinning/spreading, as well as the slope of the path topography and any interaction of the flowing mass with rugged terrain and/or deformable substrates. This distinctive setting clearly identifies a rationale for exploratory numerical modelling, which could be used to examine the sensitivity of rock avalanche run-out to changes in key variables.

2.2.2 Tsunami-generating rock avalanche at Paatuut, AD 2000

During the afternoon of the 21 November 2000 a large ($>90 \times 10^6$ m^3) rock avalanche occurred at Paatuut, ca. 40 km north-west of the town of Saqqaq on the south coast of the Nuussuaq peninsula (Fig. 2.1). The rock avalanche ran out into the Vaigat fjord at velocities of 140-200 km h^{-1}, where ca. 30×10^6 m^3 of the partly submerged deposit toe then failed again into the sea, generating a submarine slide and a tsunami with a run-up of ca. 20 m at Paatuut and up to 10 m on the opposite coast (Fig. 2.5; Szczuciński *et al.*, 2012).
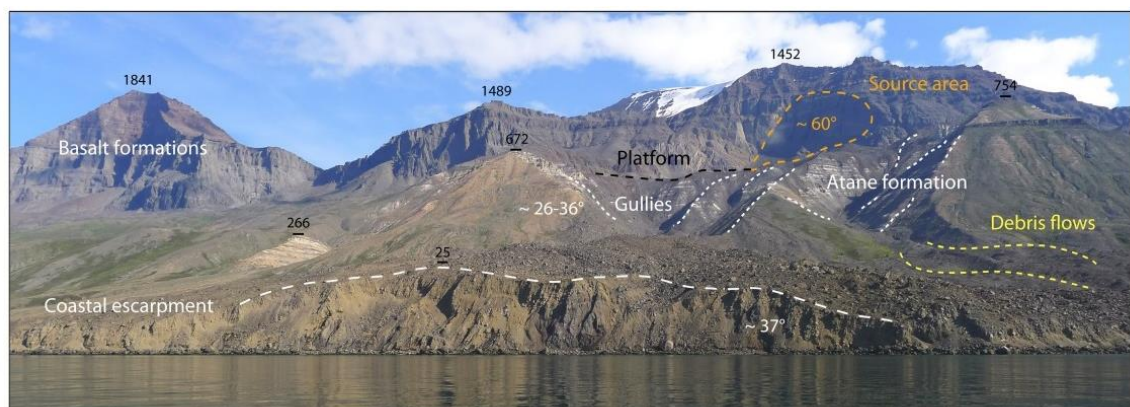
Figure 2.5) View offshore looking onto the deposit at Paatuut. The source area of the rock avalanche is outlined in orange and situated between ca. 1,000-1,400 m above sea level. Gullies through the Atane Formation, which formed a bypass zone for the material, are approximately delimited by the white dotted lines. The lower section of the deposit comprises two lobes that merge downwards into one and have been reworked at the edges by debris flows (yellow). A steep escarpment terminates the subaerial part of the slide. All elevations are in m above sea level.

2.3 Summary

Risk assessments of the threats posed by rock avalanches rely upon numerical modelling of potential run-out and spreading, which itself is contingent upon a thorough understanding of the flow dynamics and rheology inferred from deposits left by previous events. Few records exist of multiple rock avalanches with boundary conditions sufficiently consistent to develop a set of more generalised rules for behaviour across events. A unique cluster of 20 large rock avalanche deposits along the Vaigat Strait, West Greenland, offers a unique opportunity to model a large sample of adjacent events sourced from a stretch of coastal mountains of relatively uniform geology and structure. In particular, the event and corresponding tsunami at Paatuut (AD 2000) represents one of the best-documented events of its type and presents an excellent opportunity for calibration of numerical models by back-analysis. This series of rock avalanches therefore presents the unique opportunity to investigate the utility and sensitivity of modelling a single rock avalanche satisfactorily as a function of rheology, alongside the validity of applying the same parameters elsewhere, even within similar boundary conditions. This approach is also important for developing our process understanding of (paraglacial) rock avalanches in confined fjord settings, where correctly modelling the material flux at the point of entry into the water is critical in tsunami generation.

Chapter 3

Rock avalanches (I) Occurrence and processes

Although considerable emphasis has been placed on assessing the associated risks of catastrophic rock-slope failure, quantifying risk remains a challenge due to the complex initial failure processes and, in particular, the unpredictable post-failure behaviour of rock avalanches (Crosta *et al.*, 2006a). The unusual characteristics of rock avalanches outlined in *Chapter 1* have prompted researchers to propose a number of modes of transportation and deposition, some of which are based on the standard physics of granular materials, and some of which invoke more unusual mechanisms (De Blasio, 2009). Such hypotheses remain controversial despite decades of research. The majority of the relevant literature on rock avalanches comprises studies of individual events, with little consideration of multiple or suites of rock avalanches such as those in Vaigat (*Chapter 2*) and their relation to other surface processes. The following discussion draws upon this literature in order to address questions relating to the conditions that lead to rock avalanching and the various factors controlling run-out. The preconditioning of rock-slopes to failure and common triggering mechanisms of rock avalanches are first considered (*Section 3.1*) before more fully reviewing the current state of knowledge on rock avalanche dynamics (*Section 3.2*), avalanche-substrate interactions (*Section 3.3*) and the associated depositional processes (*Section 3.4*). The chapter concludes by highlighting some of the outstanding issues to be resolved that underpin the scope of this research (*Section 3.5*).

3.1 Rock-slope instability and common trigger mechanisms

While it is commonly known that the majority of catastrophic rock-slope failures occur in massive, hard rocks exposed on incised valleys or fjord walls, there remains a paucity of research concerning the necessary conditions for rock avalanche initiation (Friedmann *et al.*, 2003). One view suggests that tectonic histories 'predesign' the potential form and scale of rock-slope failure, with rock avalanches occurring on slopes that are predetermined to fail by virtue of a particular set of static tectonic, lithologic and slope characteristics (Scheidegger, 1998). A compilation of 814 global *in situ* stress measurements suggests that the strength of rock in the upper, brittle crust depends on the stress and damage history of the rock mass during exhumation (Leith *et al.*, 2014). The magnitude and distribution of near-surface stresses therefore reflects aspects of (i) the tectonic and exhumation history of the brittle crust, and (ii) topographic perturbation (Leith *et al.*, 2014). An analysis of the basement terranes of a number of areas where rock avalanches have occurred has revealed that this typically includes conditions such as high relief (permitting >150 m drop height), steep slopes (>25°) and a pre-fractured (effectively granular at scale) rock mass (Keefer, 1984).

Attention has also been drawn to the role that 'memory' of antecedent shear could play both in the subsequent distribution of slope deformation and in setting the failure threshold of rock-slopes, with some suggesting that this memory could explain the spatial clustering of rock avalanche deposits (Friedmann *et al.*, 2003). Detailed knowledge of the geomechanical properties of a rock-slope such as bedding, joints, foliation, and faults is required for a thorough understanding of patterns of rock-slope deformation and failure, as such factors govern the overall ability of a slope to resist the stresses acting on it and thus determine its stable geometry (Hoek and Bray, 1981). However, while these preconditioning factors may set the inherent strength of a slope, grouping characteristics in such a way ignores a number of dynamic ('preparatory') processes that act to reduce slope stability. These processes vary in both time and space, leading to a range of distributions of rock-slope deformation in a single slope over time and differentially across landscapes (Glade and Crozier, 2005).

Preparatory factors for rock-slope failure include changes in the boundary conditions of a slope and the associated redistribution of stress (e.g. via glacial debutressing, as in Vaigat; *Chapter 2*), near-surface chemical and physical weathering, and cyclic loading (e.g. thermal- and/or hydro-mechanical; Gruber and Haeberli, 2007). These, in turn, can act to connect previously non-persistent discontinuities in the intact rock mass through the progressive propagation of stress fractures and ultimately cause a reduction of rock mass strength over the long-term, conditioning the rock-slope towards failure (Prudencio and Van Sint Jan, 2007).

Rock avalanche triggers are defined as the direct stimuli that initiate rock avalanche emplacement (Wieczorek, 1996). Gradual stress release in steep rock-slopes may cause the dilation of joints, formation of sheeting joints, exfoliation joints and stress corrosion through fatigue (Fig. 3.1), leading to the occurrence of some rock avalanches without a recognisable triggering event (e.g. for ca. 50% of those events that have occurred in the Sierra Nevada; Wieczorek, 2002). For those events where a trigger is known or can be inferred, the most common are those related to seismic shaking (e.g. Jibson *et al.*, 2006) and heavy precipitation (e.g. Frayssines and Hantz, 2006). It should also be noted that a small number of historical rock avalanches have been attributed to human influences, including the 1881 event in Elm, Switzerland, where slope undercutting by a slate quarry caused an 11×10^6 m^3 rock avalanche that resulted in 115 fatalities (Heim, 1932).
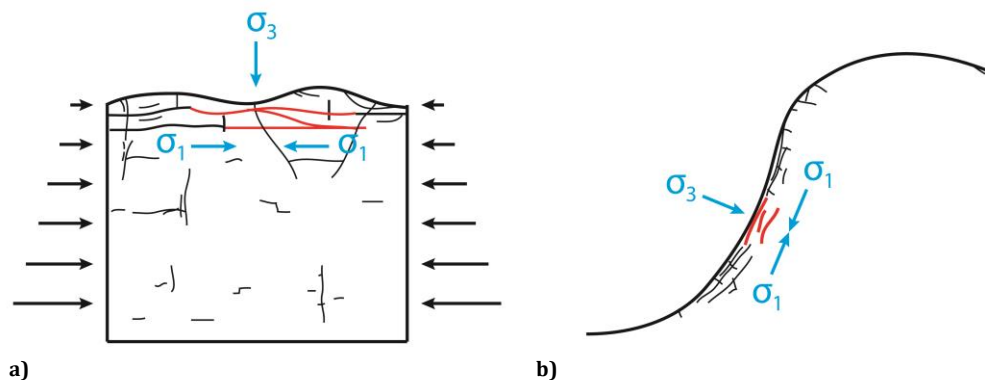
Figure 3.1) Examples of extensional fracture systems developed under high differential stress conditions: **a)** sheeting joints in a previously glaciated craton, and **b)** exfoliation joints on post-glacial valley walls. Blue arrows indicate maximum (σ_1) and minimum (σ_3) principal stress orientations, while red lines represent fractures formed in response to the illustrated stress state. Diagram adapted from Leith *et al.* (2014).

3.2 Emplacement dynamics

3.2.1 Theoretical considerations: quantifying avalanche mobility

Following initial bedrock failure, the rock mass detaches itself from the source surface and disintegrates, collapsing into large blocks that progressively fragment during motion (Evans *et al.*, 2006). This property is unique to rock avalanches (Hewitt *et al.*, 2008). Rock avalanche mobility is often quantified by the *Fahrböschung*, or apparent coefficient of friction, which is expressed as the ratio of vertical drop height, H (measured from the crest of the pre-failure rock mass to the lowest point of its path) to horizontal run-out, L (measured horizontally from the crest of the pre-failure rock mass to the most distal point of its path; Fig. 3.2).
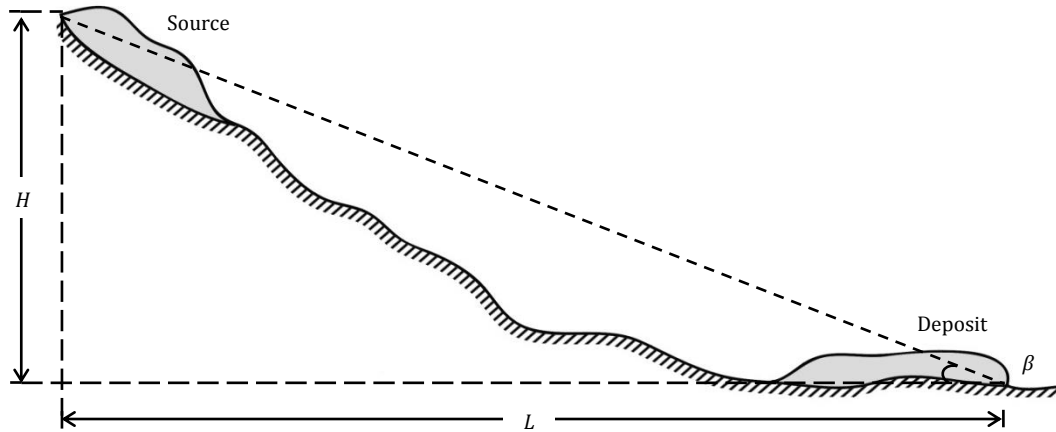
Figure 3.2) Common metrics used to quantify run-out mobility: vertical drop height (H), horizontal run-out (L) and the Fahrböschung angle (β).

The Fahrböschung angle, β, of a rock avalanche may therefore be expressed as:

$$\beta = tan^{-1}\left(\frac{H}{L}\right)$$
[Eq. 3.1]

with low values indicating high levels of mobility (Heim, 1932). Since the introduction of this concept by Heim (1932), it has been applied to a number of types of mass movements, ranging from debris flows (Rickenmann and Zimmermann, 1993) to large landslides, debris and rock avalanches (Hsü, 1975; Corominas, 1996), volcanic debris avalanches (Dade and Huppert, 1998), submarine mass movements (Legros, 2003), ice avalanches (Alean, 1985), glacial lake outburst floods (Huggel *et al.*, 2003) and mass movements on both the moon and Mars (Harrison and Grimm, 2003).

If a rock avalanche is simplified to a sliding block on an inclined plane then Coulomb's frictional law states that, as the block descends under the influence of gravity, it is resisted by a frictional force, F_F (Körner, 1976). This force is proportional to the compressive forces acting perpendicular to the contact surface (Fig. 3.3). The apparent coefficient of friction of the sliding block is therefore assumed to be dependent upon characteristics of the contact surface (e.g. basal composition, amount of surface water) but independent of its mass. This frictional force may be expressed as:

$$F_F = -mg\mu \cos \alpha$$
[Eq. 3.2]

where m is the avalanche mass, g the gravitational acceleration, α the local slope angle and $\mu = \tan\varphi_{int}$, which is the coefficient of friction expressed in terms of the internal angle of friction, φ_{int}, an experimental property of rocks on the order of ca. 35-40° (Middleton and Wilcock, 1994).

As the kinetic energy of the block is zero in the initial, I, and final, F, states, the overall change in potential energy of the mass must be equal to the work performed by F_F. If δI is an infinitesimal displacement along the run-out path, the change in potential energy of the mass is given by:

$$\Delta mgH = -\int_{I}^{F} F_F \delta I \qquad \text{[Eq. 3.3]}$$

Upon substitution of F_F (Equation 3.2), the change in potential energy is of the form:

Figure 3.3) Free body diagram of a block sliding down an inclined plane under Coulomb's frictional law. Here, *mg* is the gravitational force, *mgsinα* the component accelerating the mass, *mgcosα* the normal force and *mgμcosα* the frictional force Adapted from Erismann and Abele (2001).

$$\Delta mgH = -\int_{I}^{F} -mg\mu \cos\alpha \, \delta I \qquad \text{[Eq. 3.4]}$$

With solution of Equation 3.4 therefore yielding:

$$\Delta mgH = mg\mu - \int_{I}^{F} \cos\alpha \, \delta I \qquad \text{[Eq. 3.5]}$$

$$H = \mu - \int_{I}^{F} \cos\alpha \, \delta I \qquad \text{[Eq. 3.6]}$$

If the overall slope of the event in question is built up by vectorial addition of n partial lines of length δI, the overall run-out, L, may then be expressed as:

$$L = -\int_{I}^{F} \cos\alpha \, \Sigma\delta I \qquad \text{[Eq. 3.7]}$$

With division of Equation 3.6 by Equation 3.7 thus yielding:

$$\frac{H}{L} = \mu \qquad \text{[Eq. 3.8]}$$

It can therefore be shown that, under a simple Coulomb frictional law and taking typical values for φ_{int} (ca. 35-40°), $\mu \approx 0.78\text{-}0.84$. Under these conditions L should only be marginally greater than H, and the relative run-out of a rock avalanche should be independent of gravity and event size (Dade and Huppert, 1998). This behaviour has been confirmed by laboratory experiments with granular flows of sand as well as observations of small-scale landsliding and rockfalls (e.g. Hutter *et al.*, 1995; Iverson, 1997; Denlinger and Iverson, 2001; Pudasaini and Hutter, 2003; Ancey, 2005; Jop *et*

al., 2006; Pudasaini and Domnik, 2009).

Conversely, the most remarkable feature of rock avalanches, and one that has been widely discussed in previous work, is their exceptional run-out (e.g. Hungr, 1995; Kilburn and Sørensen, 1998; Davies *et al*., 1999; Hungr and Evans, 2004 and references therein). This behaviour is inconsistent with predictions made by simple Coulomb frictional laws described above. This is most apparent when considering the plot shown in Fig. 3.4, which is characterised by a marked decrease in *H/L* as avalanche volume increases from ca. 10^5-10^6 m^3 to 10^9 m^3. Over this range the displaced material ceases to assume a frictional behaviour, characterised by $H/L > 0.6$ ($\beta \geq 32°$), and instead adopts a fluid-like behaviour, with *H/L* reaching

Figure 3.4) Plot of *H/L* against volume for subaerial volcanic rock avalanches (black crosses), subaerial non-volcanic landslides and rock avalanches (blue crosses) and rock avalanches onto glaciers (red crosses). The Paatuut event (AD 2000) is labelled in yellow. Data compiled from a literature review of rock avalanche events (*Appendix A*).

values as low as 0.01 ($\beta < 6°$; Fig. 3.4). This has been labelled the 'volume effect', and many researchers have sought to identify a possible mechanism by which friction could be reduced in such large events (Legros, 2003).

3.2.2 Rock avalanche mobility and run-out

The complex behaviour of rock avalanches adds greatly to their destructive potential and hinders efforts to model their behaviour (Catane *et al*., 2008). The decrease in frictional resistance causes rock avalanches to exhibit excessive mobility such that they are able to:

1. Run over and around significant obstacles in their paths (Hewitt *et al*., 2008);
2. Abruptly change direction, commonly running perpendicular to the original direction of movement and at times reflecting off topography (Eisbacher, 1979);
3. Run a considerable distance up distal slopes, leaving elevated deposits on opposing valley slopes and evidence of super-elevation in topographic bends (Evans, 1989; Evans *et al*., 1994).

Although topography is widely recognised to be an important influence upon rock avalanche dynamics, topographic constraints alone are unable to fully account for the excessive mobility of rock avalanches (Mudge, 1965; Shreve, 1968; Whitehouse and Griffiths, 1983; Evans, 1989). Potential mechanisms for the extensive propagation of rock avalanche masses remain contentious but principally involve two processes: the first, translation, is guided by basal friction, while the second, deformation, is driven by internal friction (Davies *et al.*, 1999). A reduction in either basal or internal friction would cause the rock mass to run out further than dictated by the volume effect alone (Imre *et al*., 2010). This discussion therefore distinguishes between theories that involve variations in: a) the translation process, and b) the deformation process.
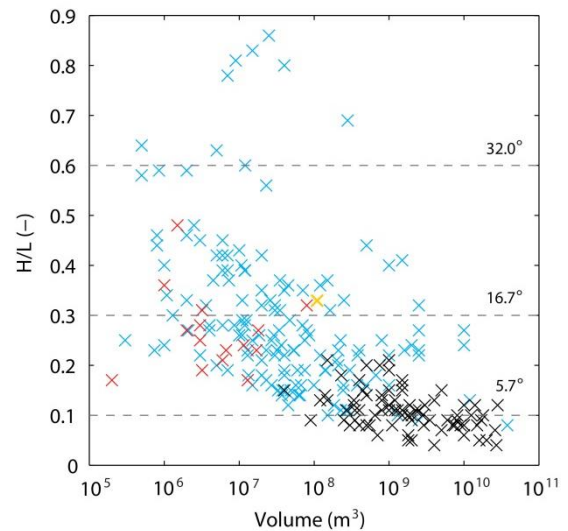
3.2.2.1 Basal friction

A number of authors have sought to explain the enhanced mobility of rock avalanches using mechanisms that infer a reduction in basal friction of the rock mass, effectively treating the movement as a slide rather than a flow. A distinction should therefore be made between lubrication, which is restricted to a thin basal layer, and fluidisation, which affects the internal dynamics of a considerable portion of the deforming mass (Erismann and Abele, 2001). The mechanism driving reduced basal friction is most commonly conceptualised as consisting of lubrication of the rock mass via either: a cushion of trapped air (Shreve, 1968); low-friction sliding on dissociated or melted rock confined along the basal sliding plane (Johnson, 1978; Erismann, 1979); the presence of a wet basal shear zone (Voight and Sousa, 1994); or the liquefaction of saturated sediments entrained from the run-out path (Abele, 1974; Sassa *et al.*, 1998).

The absence of evidence for massive air jetting, normally graded sediments and the elutriation of fines in rock avalanche deposits all counter theories that involve air cushioning of the rock mass (Cruden and Hungr, 1986). These theories were formerly challenged by observations of such events on the moon and Mars, where minimal air and/or water was thought to be available to act as a lubricant (Lucchitta, 1979), although recent evidence strongly implicates the presence of moisture or carbon dioxide in their emplacement (Quantin *et al.*, 2004). Evidence for enhanced sliding due to the dissociation and/or melting of rocks under friction (frictionites) remains similarly limited, and although there exist several examples, including Kanchenjunga in the Sikkim Himalaya and Arequipa in Peru, these represent only a minority of cases (Legros *et al.*, 2000; De Blasio and Elverhøi, 2008; Weidinger and Korup, 2009).

The longest standing hypothesis for the excessive mobility of rock avalanches involves basal liquefaction by rapid undrained loading as a mechanism for lubrication (Heim, 1882). Implicating water as a lubricant is considered to be more realistic than air owing to its incompressibility as well as its higher density and viscosity (Legros, 2003). Changes in pore pressure at the base of the moving mass can be initiated by shearing within a highly saturated layer, entrainment of river water and/or water-saturated valley-fill deposits, or the melting of ice or snow by frictional heating (Evans and Clague, 1988; Voight and Sousa, 1994; Prager *et al.*, 2006). However, an interesting case is presented by rock avalanches that are confined to narrow valleys, such as those in the Karakoram Himalaya, which can reach hundreds of metres in depth (Hewitt *et al.*, 2008). Detailed sedimentological investigations of these deposits have shown that, during such events, the majority of deformation takes place within and not at the base of the rock avalanche mass, indicating the importance of deformation processes and internal friction in their movement.

3.2.2.2 Internal friction

Fluidisation of the rock avalanche mass involves an overall reduction in frictional resistance to shear, developing differential strain throughout the entire failed volume. This could be driven by: trapped air or steam generated by the vaporisation of groundwater (Goguel and Pachoud, 1972); the presence of interstitial fluids (Crosta *et al.*, 2009); or dilatation of the grain mass via 'acoustic fluidisation' (Melosh, 1979), 'mechanical fluidisation' (Scheidegger, 1973), or dynamic fragmentation (Davies *et al.*, 1999).

A number of theories invoke an intergranular medium to account for the excessive mobility of rock avalanches, and although some suggest that high gas pressures are responsible (Goguel and Pachoud, 1972), rock avalanche deposits would be expected to exhibit features characteristic of the upward escape of gas, such as normal grading, elutriation of fines and cratering, none of which have been observed. Instead it has been proposed that, upon mixing the fines of rock avalanche debris with water, the rheology of the flow shifts towards that of a non-Newtonian fluid (McArdell *et al.*, 2007). Unlike Newtonian fluids, in which the viscous stresses are directly proportional to the local strain rate, non-Newtonian fluids are characterised by a load-independent shear resistance that is thought to result in the volume effect illustrated in *Section 3.2.1* (Iverson *et al.*, 2010).

The role of dispersive pressure, where the grain mass is dilated by high impulsive contact pressures, also remains contentious (Davies, 1982). The dispersive grain flow theory first proposed by Hsü (1975) invokes fluidisation of the rock mass via the internal sorting of fines, which is then thought to fluidise coarser particles. However, this does not account for the volume effect, as larger volumes of debris would instead compact these particles and reduce fluidisation (Erismann, 1986). The energy required to cause these grain fluctuations has also been proposed to originate from acoustic-frequency vibrations at the boundaries of the moving mass (Melosh, 1979). Although this has been experimentally demonstrated, this mechanism would require a continuous source of energy and so is not deemed permissible unless the vibrations were self-perpetuating (Collins and Melosh, 2003). A similar decrease in shear resistance may be induced by mechanical fluidisation, which has been proposed to occur when rapid shearing of a granular mass causes the friction angle to spontaneously decrease, resulting in dynamic interactions within the mass that force particles away from each other (Davies, 1982). This is also yet to be shown experimentally.

It has been suggested that dispersive pressure can be generated by dynamic fragmentation, whereby particles undergo an increase in elastic strain until they are crushed and the energy is converted into kinetic energy as particles fracture (McSaveney and Davies, 2007). Fragments are then forced away from the original centre of mass, causing a reduction of inter-granular friction and an increase in lateral and longitudinal spreading (Rait *et al.*, 2012). Pressure-induced melting of any ice contained within the rock mass can also fluidise the moving mass and further increase mobility (Davies *et al.*, 1999). Although gradual fragmentation does not increase the mobility of the centre of mass, it has been shown to more fully account for the energy budget of rock avalanches and is supported by some field (preserved but fragmented clasts) and laboratory (high particle surface areas, equivalent to fault gouge) evidence (Smith *et al.*, 2006; Bowman *et al.*, 2012).

The majority of theories of rock avalanche mobility discussed here are consistent with local observations but, crucially, they remain inconsistent with universal observations or physical constraints (Friedmann, 1997). All require either novel physics (e.g. fluidisation via air-cushioning or acoustic vibrations), or particular environmental conditions (e.g. undrained loading failure of a water-saturated substrate), meaning that there is no unifying theory that can adequately explain the wide range of conditions under which excessive mobility occurs (Davies and McSaveney, 2009).

3.3 Rock avalanche-substrate interactions

Although it is commonly known that the interaction with and subsequent entrainment of

rock avalanche run-out path materials can exert a significant influence on their emplacement dynamics and run-out behaviour, the specific processes acting at the base of rock avalanches during travel over (non-)deformable and erodible substrates remain poorly understood, exceedingly challenging to observe, and therefore difficult to model (Dufresne, 2012).

3.3.1 Substrate erosion and entrainment

During the failure process, fragmentation of the rock mass causes an initial increase in volume in the region of 7-26% (Hungr, 1981). Further increases in volume of up to 800% may then occur by entrainment of substrate material (Hungr and Evans, 2004). A detailed review of the main processes of entrainment is provided by Dufresne (2009). Rock avalanches must first exceed a minimum basal shear stress before substrate entrainment occurs. This entrainment rate is related to substrate properties, such as shear strength, as well as the velocity of the moving rock mass, avalanche loading, the heterogeneity of surficial materials and their stability on an incline (Crosta *et al.*, 2008). Entrainment may therefore proceed progressively, or failure of the substrate may occur at greater depths where weaknesses are found between different substrates (McDougall, 2006). The entrainment of surficial materials into a rock avalanche can lead to changes in its bulk and/or basal composition to such an extent that the overall mechanical behaviour, or rheology, of the rock avalanche is affected (Hungr and Evans, 2004). It is well documented that, when rock avalanches entrain substantial amounts of saturated substrates and/or surface water, ice or snow, they develop a highly mobile flow regime that can increase run-out by several orders of magnitude (e.g. Pandemonium Creek, British Columbia: Evans *et al.*, 1989; Huascarán, Peru: Keefer and Larsen, 2007). Where the rock avalanche mass interacts with saturated sediments without significant entrainment, complex substrate deformation features may develop, which are discussed below.

3.3.2 Substrate deformation

Rock avalanches emplaced across deformable substrates may entrain, transport and compress large masses of sediment, generating prominent constructional landforms such as complex fold and fault structures (Yarnold, 1993; Abdrakhmatov and Strom, 2006; Hewitt *et al.*, 2008; Dufresne and Davies, 2009), shearing (Hewitt, 2006), erosion surfaces and bulldozer facies (Belousov *et al.*, 1999). While thick, yielding substrates tend to deform, consuming momentum and thereby impeding rock avalanche mobility, run-out over more resistant substrates expends little energy and is thought to induce the basal shear stress and agitation necessary for dynamic internal processes to increase avalanche mobility (*Section 3.2*; Dufresne, 2012). The effect of deformable and erodible substrate conditions on the emplacement mechanisms and subsequent run-out of rock avalanches is therefore a balance between: (i) the energy required to mobilise substrate material, (ii) the reduction of frictional resistance within the failing substrate, (iii) how efficiently the substrate is mobilised (for example, whether or not the substrate deforms and impedes rock avalanche motion), and (iv) whether the rock avalanche mass entrains significant quantities of water or saturated substrates. Although numerical models are able to account for changes in topography as a result of these processes, the results are sensitive to the assumed erosion rate and maximum erosion depth, which remain difficult to quantify (McDougall and Hungr, 2005).

3.4 Deposit characteristics

The energy dissipation and subsequent run-out of rock avalanches is strongly influenced by a number of factors, leading to a range of depositional features, surface morphologies and, at a local level, specific internal tectonic and facies characteristics (Okura *et al.*, 2003).

3.4.1 Sedimentology and internal structure

Research on rock avalanches has primarily been driven by the need to quantify the frequency of such events for risk assessments, to understand their relative contribution to sediment budgets and landscape evolution, and to back-analyse specific case studies (Weidinger *et al.*, 2014). This is reliant upon the successful detection of deposits emplaced by past events. However, few studies systematically examine the sedimentary and petrographic characteristics of rock avalanche deposits in non-volcanic settings (Wassmer *et al.*, 2004). Some authors have attempted to create a set of diagnostic criteria for the identification of rock avalanche deposits, which include sedimentological characteristics such as:

1. Surface matrix of angular boulders and megaclasts, commonly termed a carapace (Hewitt, 2002);
2. An abundance of finely comminuted rock within the main rock avalanche body (McSaveney and Davies, 2007);
3. A 'mélange' of basal facies, including fluvial and glacigenic boulders that have been entrained into the base, which form banded layers of pervasively fragmented though otherwise coherent clasts (Weidinger *et al.*, 2014);
4. Preservation of source stratigraphy (Strom, 1999);
5. Internal grain size distributions that are controlled by source lithological variation rather than variations in the transport mechanism (Dunning, 2006).
6. Fine-sediment signatures, such as fines-coated grains and agglomerates, which are characteristic of rapid, high-stress comminution (Reznichenko *et al.*, 2012b).

These sedimentological facies are considered to be important criteria for distinguishing rock avalanches from macro- and microscopically similar glacial deposits, tectonic fault-zone breccias and impact breccias (Weidinger *et al.*, 2014).

3.4.2 Morphology

A number of authors have defined a series of morphological criteria for identifying rock avalanche deposits, including:

1. Evidence of the deposit having conformed to the local topography during its emplacement (Heim, 1932; Nicoletti and Sorriso-Valvo, 1991);
2. Sharply-defined margins and steep terminations, with little spreading of any debris beyond these (Cruden and Hungr, 1986);
3. Surfaces that are characterised by ridges and troughs (Dufresne and Davies, 2009);
4. Evidence of super-elevation in topographic bends and elevated deposits where the rock avalanche has run up opposing valley slopes (Evans, 1989; Evans *et al.*, 1994).

Topographic interference can involve both longitudinal and transverse confinement of the rock

avalanche mass, as well as the effects of changes in slope, valley geometry, and junctions that can act to block, confine or diverge flow (Fig. 3.5; Hewitt, 2002). Such constraints are able to produce deposits that can reach hundreds of metres in depth, as in Flims, Switzerland (von Poschinger *et al.*, 2006). Flows that are channelised by topography, such as Köfels and Vaiont in the Alps or Tsergo Ri in Nepal, tend to run out further than free spreading flows or those impeded by a frontal impact (Heim, 1932; Heuberger *et al.*, 1984). The resulting depositional features are therefore highly dependent upon the relations between rock avalanche volume and valley geometry. The effects of various cross-valley topographic constraints on the morphology and structure of rock avalanche deposits are summarised in the schematic diagram shown in Fig. 3.5.

The final configuration of the depositional mass is further affected by the basal topography of the run-out path, which strongly conditions processes of flow compaction, resistance to and patterns of basal erosion (*Section 3.3*; Dufresne *et al.*, 2010). The resulting surface flow structures include features such as sharply defined margins, digitated fronts, flow bands, transverse ridges, longitudinal ridges, conical mounds (or 'molards') and coarse boulder carapaces (Fig. 3.6; Strom, 2004). These structures are believed to reflect processes active during the flow and are therefore important for inferring aspects of flow dynamics (Dufresne and Davies, 2009). Deposits that are emplaced across areas of rugged terrain tend to exist as isolated ridges or locally thickened and hummocky remnants that have been exposed by post-emplacement erosion and detached from their distant rock wall source, complicating the interpretation of past events (Hewitt, 2002). On open slopes, topographic irregularities may induce interactions between debris streams moving at different speeds or along different trajectories, generating transverse or longitudinal ridges hundreds of metres in length and that stand tens of metres above the rest of the deposit (Mollard, 1977). In addition, compressional ridges and/or raised flow fronts are often found in the proximal-medial reaches of deposits emplaced by smaller, low-velocity rock avalanches (Abdrakhmatov and Strom, 2006). Attempts to assess the complex behaviour of the Flims rock avalanche as it ran out over rugged terrain illustrate the weaknesses in using two-dimensional (2D) numerical models to capture such behaviour (von Poschinger *et al.*, 2006). These models are unable to explicitly account for lateral variations in intensity, hindering their ability to account for energy losses within the rock avalanche mass that are caused by complex topography (Hungr and McDougall, 2009).

3.5 Summary

The majority of theories of rock avalanche mobility discussed in *Section 3.2* are consistent with local observations but, crucially, they remain inconsistent with universal observations or physical constraints (Yarnold, 1993; Friedmann, 1997). All require either novel physics or particular environmental conditions, meaning that there is no unifying theory that can explain the wide range of conditions under which excessive mobility occurs (Davies and McSaveney, 2009). To date, few of these theories have been directly tested, either through physical or numerical experiments, and there remains a paucity of research seeking to determine their relative importance. Although many now have an equivalent empirical, analytical and/or numerical formulation that can be used for modelling rock avalanche propagation, none are currently able to predict the circumstances under which long run-out occurs, or the nature of that run-out.
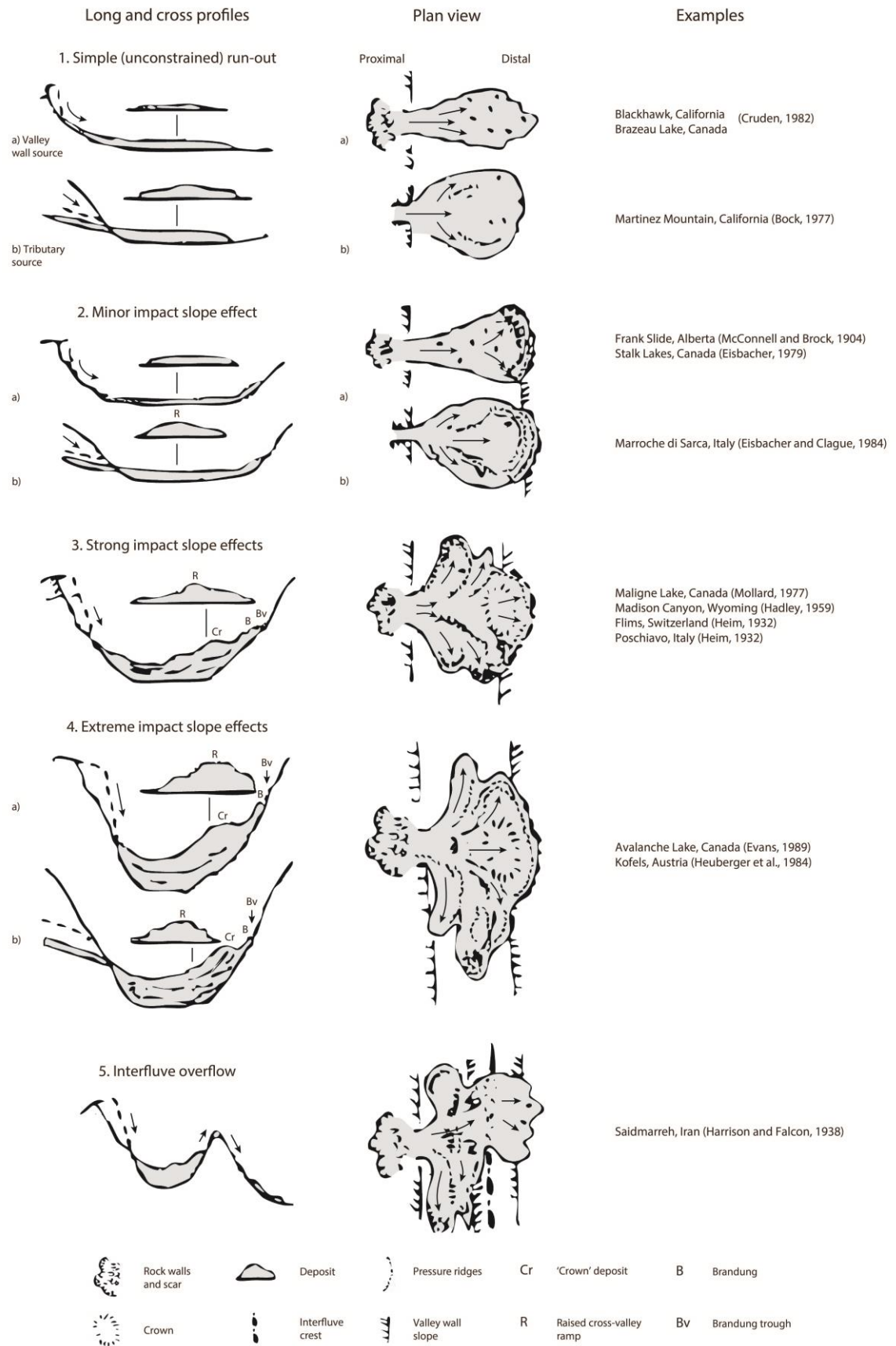
Figure 3.5) Schematic long- and cross -sections, and plan forms of cross-valley rock avalanche deposits. The *Brandung* represents the culmination of the rock avalanche's upward climb of an opposing slope and consists of a distal ridge with a steep front. In types 1, 2 and 4, subtypes are indicated where debris, initially confined in tributary chutes or canyons, is emplaced in the main valley. Diagram adapted from Hewitt (2002).
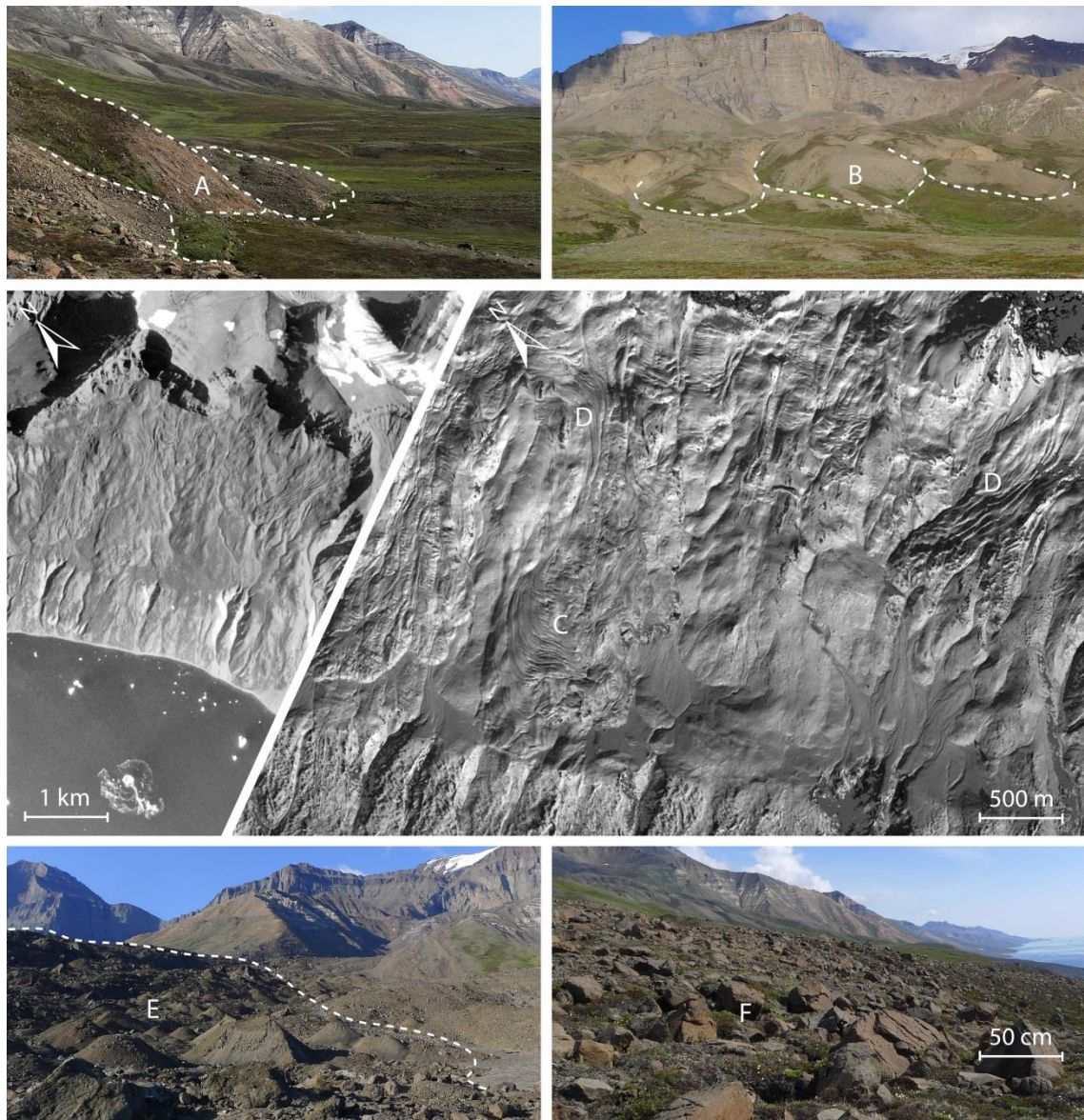
Figure 3.6) Surface flow features characteristic of rock avalanche deposits. Centre-left: contextual image of several rock avalanche deposits and their situation on the Vaigat Strait, West Greenland (*Chapter 2*). Centre-right: 2 m satellite imagery showing in detail the surface flow features of these deposits. These include sharply defined margins (A), digitated fronts (B), transverse ridges (C), longitudinal ridges (D), fields of conical mounds, or 'molards' (E), and coarse boulder carapaces (F). 2 m orthoimages were acquired on 19 June 2012 by WorldView-1 and subsequently provided by Ben Smith (Polar Science Center).

Although it is commonly known that the interaction with and subsequent entrainment of rock avalanche run-out path materials can exert a significant influence on their emplacement dynamics and run-out behaviour, these processes remain difficult to quantify as detailed field and experimental data are scarce. Laboratory experiments have been used to propose and test a number of constitutive relationships (Egashira *et al.*, 2001; Takahashi, 2001); however, the validity of these relationships under field conditions is yet to be demonstrated. Although numerical models are able to account for changes in topography as a result of the erosional and depositional processes discussed in *Sections 3.3* and *3.4*, the results are sensitive to the assumed erosion rate and maximum erosion depth, which remain difficult to quantify (McDougall and Hungr, 2005).

Studies of rock avalanche dynamics are based, with variable emphases, on theoretical

27

considerations, field observations, laboratory analogue models and computer-based numerical models. While much of the relevant literature on rock avalanches comprises studies of individual events, these come at the expense of studies that are focussed on regional investigations of multiple rock avalanches. 3D numerical models offer an alternative approach to small-scale analogue modelling and the assessment of events in real-time, and are therefore well placed to act as a tool to investigate and better understand the diversity, complexity and regional contexts of suites of rock avalanches, such as those in Vaigat (*Chapter 2*).

Chapter 4

Rock avalanches (II) Numerical run-out modelling

Quantitative risk assessments of the future hazard posed by potential rock avalanches rely upon the successful prediction of their extent and character of motion (Evans *et al.*, 2001). Although laboratory models of granular flows are valuable for investigating scale-independent effects of motion, they are limited by their limited ability to scale physics and the mechanisms exhibited by rock avalanches (Manzella and Labiouse, 2013). Computer-based models present an alternative that can also be used for scenario testing, offering a compromise between small-scale analogue modelling and the assessment of events in real-time, where dynamic measurements are expensive or, more often, impossible (Hungr, 2006). Modelling the mobility of rock avalanches is complicated by the complex behaviour experienced by the fragmenting rock mass during motion (Crosta *et al.*, 2006b); this difficulty is manifest in the burgeoning number of theories of motion and mechanisms presented in the literature, as illustrated in *Chapter 3*. This is further compounded by the common lack of pre-, syn- and post-failure observations of such phenomena, which are fundamental constraints on the development, calibration and validation of any numerical model of rock avalanche run-out and behaviour (Dahl *et al.*, 2013). As a result, the majority of numerical modelling studies focus on replicating the dynamics of a single, well-constrained event, and fail to consider the wider utility and sensitivity of the rheological calibration obtained. A series of 20 large rock avalanche deposits along the Vaigat Strait, West Greenland, presents the unique opportunity to undertake a case-specific calibration and investigate the validity of applying the same parameters to other events with similar morphological and geophysical conditions (*Chapter 2*). The following discussion reviews a number of numerical approaches to modelling the post-failure behaviour of rock avalanches (*Section 4.1*) and discusses the rheological laws commonly used to govern their motion in these models (*Section 4.2*). From this discussion, a continuum dynamic model, *VolcFlow*, which is suited to modelling the events observed in Vaigat is identified and described (*Section 4.3*).

4.1 Numerical run-out models

Numerical models constitute an important tool for simulating the large scale and complex motion of rock avalanches, allowing researchers to simulate their behaviour, and, ultimately, to predict run-out and perform hazard zonation (Crosta *et al.*, 2003). Currently, all numerical models used for this purpose are deterministic and produce a constant output for a given parameter input, with none incorporating a random (or probabilistic) aspect that prevents repeatability between the outputs for a given input (Hungr *et al.*, 2005). Numerical run-out models are primarily divided into two types, both of which are discussed below. The first, empirical models, make use of statistical

analyses of empirical observations, while the second, dynamic models, simulate rock avalanche motion by solving a governing set of equations of motion at every time step.

4.1.1 Empirical models

Statistical analyses of empirical observations correlate physical properties of a mass movement, such as fall height and failure volume, with the extent of its run-out and deposit (Glade and Crozier, 2005). The most commonly used method of run-out prediction is based on the empirical relation between failure volume and the apparent coefficient of friction (*Section 3.2.1*), allowing the run-out of a granular flow to be derived from a given failure volume (Scheidegger, 1973; Hsü, 1975; Lucchitta, 1979; Nicoletti and Sorriso-Valvo, 1991; Corominas, 1996; Fannin and Wise, 2001; Devoli *et al.*, 2009). A number of linear regression equations for calculating run-out have been developed, which typically take the following power-law form:

$$log_{10}\left(\frac{H}{L}\right) = -a\,log_{10}\,V + b \qquad \text{[Eq. 4.1]}$$

$$L = aV^b H \qquad \text{[Eq. 4.2]}$$

where *a* is the slope and *b* is the intercept of the line at $log_{10}V$ = 0. The type of mass movement in question, and the morphology of its run-out path, conditions the values of coefficients *a* and *b* (McDougall *et al.*, 2012). Similar statistical correlations between failure volume and inundation or deposit area have also been proposed by Iverson *et al.* (1998) to delineate the aerial extent of volcanic lahars, and, with the appropriate modification of the input datasets and statistics, this approach has been adapted to forecast the run-out of rock and debris avalanches (Iverson, 2006). This method has also been used to derive peak estimates of parameters such as flow velocity or discharge and is well-suited to probabilistic treatment, although little information is provided regarding the spatial distribution of the parameters in question (Rickenmann, 1999).

Despite their ease of use, empirical approaches are difficult to apply with a high degree of certainty and on a case-specific basis owing to the large data scatter in the constitutive datasets (Hunter and Fell, 2003). In addition, empirical models are unable to fully describe the kinematics of rock avalanche motion, particularly when considering unconfined mass movements, as model outputs only consist of single point predictions (Fannin and Wise, 2001). Such an approach is not appropriate for answering the research questions outlined in *Chapter 1*, which require more complex and physically realistic models for simulating rock avalanche run-out and mobility. However, in spite of their limitations, empirical methods constitute a useful starting point for run-out analyses, with the flexibility of statistical models allowing them to be applied even while in the field in order to carry out preliminary analysis for hazard assessments that may later be refined by more rigorous, physically-based models (McDougall *et al.*, 2012).

4.1.2 Dynamic models

Dynamic models simulate movement of the deforming mass by solving a governing set of equations of motion at every time step of the model (Savage and Hutter, 1989). This approach is thus able to explicitly account for local and geometrical material characteristics through time,

providing estimates of velocity and flow depth at different points along the run-out path that constitute a more complete description of rock avalanche motion in space and time. While lumped mass models idealise the motion of the mass as a single point (e.g. Hutchinson, 1986), such representations fail to account for internal deformation and are only able to provide what is deemed a reasonable approximation of the movement of the centre of gravity of the flowing mass (Evans *et al.*, 1994). Conversely, deformable mass models are more computationally intensive and model the deformation of a rock avalanche throughout its emplacement, incorporating both solid (dislocation along the failure surface) and fluid (continuous flow) deformation (McDougall and Hungr, 2004). Among these are discontinuum models, which simulate large-scale deformation by modelling the interactions of multiple individual particles and the ground surface (e.g. Cundall and Strack, 1979; Cleary and Prakash, 2004; Banton *et al.*, 2009), and continuum models based on the assumptions of fluid mechanics (e.g. Hungr, 1995; Denlinger and Iverson, 2004).

For the purposes of this research, the most suitable approach for the dynamic analysis of rock avalanche propagation across 3D terrain is presented by the depth-averaged continuum dynamic models pioneered by Savage and Hutter (1989) and developed by authors such as Iverson *et al.* (1997) and McDougall and Hungr (2004). Motion in these models is primarily governed by mass and momentum balance equations based on the shallow water (or Saint Venant) equations, which are a set of hyperbolic/parabolic partial differential equations that describe fluid flow below a pressure surface (Mangeney-Castelnau *et al.*, 2005). These equations are derived by integrating the Navier-Stokes equations, which themselves are derived from the equations for conservation of mass and linear momentum, with respect to flow depth in a procedure known as depth-averaging (Hungr, 1995). This assumes that stresses increase linearly with depth and neglects shear stresses in the depth-wise direction. It is also assumed that the depth of the flowing mass varies gradually and is small in relation to its overall extent, which is a classical shallow flow assumption of hydrodynamics (Chow, 1959). The continuum dynamic models commonly used in numerical run-out modelling couple frictional internal stresses, which govern flow spreading, to basal shear stresses, which provide resistance to forward motion of the flowing mass (*Section 3.2.2*; McDougall *et al.*, 2008). Such models are therefore able to account for the influence of internal shear strength, spatially variable rheology and erosion or entrainment of materials from the run-out path, with the simulated mass able to spread, contract, abruptly change direction, diverge or join in response to local topography (McDougall and Hungr, 2004). Continuum dynamic models therefore provide the most complete description of rock avalanche motion and offer the best possible opportunity to assess the emplacement dynamics of the rock avalanches in Vaigat (*Chapters 1* and *2*).

4.1.2.1 Model classification

Although a variety of ways exists to classify continuum dynamic models, key distinctions are commonly made between the dimension of the model, its reference frame, and whether or not the model requires measurement or calibration of its rheological parameters.

Model dimensions

Although natural processes occur in three spatial dimensions and a temporal dimension,

numerical models simulate rock avalanche motion across either 1D, 2D (prediction in the x and y or x and z coordinates) or 3D (prediction in the x, y, and z coordinates) terrain. While 2D models constitute a useful tool for the preliminary calibration of 3D models, the complex behaviour of rock avalanches is ultimately best captured using models that simulate their propagation across 3D terrain (Hungr and McDougall, 2009).

Solution reference frame

Continuum dynamic models formulate the depth-averaged equations of motion in one of two frames of reference: Eulerian or Lagrangian. In computational fluid dynamics it is conventional to use finite difference or finite element schemes in a Eulerian framework, using a fixed reference grid (e.g. O'Brien *et al.*, 1993; Kelfoun and Druitt, 2005; Kwam and Sun, 2006; Medina *et al.*, 2008; Pirulli and Mangeney, 2008; Begueria *et al.*, 2009; Christen *et al.*, 2010). While finite difference schemes discretise space in rows and columns of orthogonal lines, finite element schemes use an irregular discretisation of space and integrate the governing equations over each finite element, summing the solution over the entire problem domain (Cook *et al.*, 2007). Models formulated in this framework require a dense, fixed computational grid for the solution of a more complex set of governing equations, while Lagrangian coordinates use a moving reference frame that is advected with the flowing mass (e.g. Pitman and Le, 2005; Chen and Lee, 2007; Hungr and McDougall, 2009). The use of fixed mesh, adaptive mesh or meshless techniques in a Lagrangian framework provides a higher resolution within the flow, although this is at the cost of instabilities arising from distortion of the computational elements of the reference grid. The severe deformation of rock avalanche materials can be problematic for simulation with both Eulerian and Lagrangian grid-based numerical methods and there are, at present, few combination methods capable of accurately simulating large-scale deformation while also tracking motion (Schwaiger, 2008).

Model set-up, calibration and boundary conditions

Accurate simulation of the dynamics of rock avalanche run-out is contingent upon selecting the correct boundary conditions, initial conditions and parameters (Crosta *et al.*, 2006b). An important distinction can be made between numerical models that require the input of measured physical parameters and those that are calibrated through back analyses (McDougall *et al.*, 2012). The majority of numerical models used for modelling rock avalanche run-out use a calibration-based approach, which stems from the empirical methods of hydraulic engineering (Hungr *et al.*, 2007). This involves calibration of the model via the statistical back-analysis of full-scale prototype events, where rheological parameters are systematically adjusted until the simulated run-out is in close agreement with observed geometrical properties of the landslide, such as: travel distance, deposit thickness, trim-line tilting derived velocities, run-up distance and emplacement time (Hungr, 2006). This approach will therefore be used to calibrate numerical models of rock avalanche run-out in West Greenland, via back-analysis of the Paatuut event (AD 2000; *Chapter 2*).

Calibration-based procedures are often criticised as being a form of tuning or curve-fitting exercise that encourages the arbitrary adjustment of variables in order to simulate an individual event (Iverson, 2003). Successful model calibration is therefore reliant upon the careful selection of

a series of events with consistent patterns of rheology type and ranges of parameter values, which can be used to reproduce the behaviour of large groups of similar events. There is a shortage of work of this kind, however, with previous modelling efforts having focussed on qualitative assessment of the best-fit parameter values for relatively small groups of events (Hungr and Evans, 1996; Ayotte and Hungr, 2000; Revellino *et al.*, 2004). This demonstrates the importance of this work in Vaigat (*Chapter 2*), a unique setting with boundary conditions consistent enough to allow for the investigation of the utility and validity of modelling a series of events using a single set of parameters obtained by back-analysis of one well-constrained case.

4.1.2.2 Examples of dynamic run-out models

A number of dynamic models have been developed to simulate the run-out behaviour of rock avalanches, the most commonly used of which are summarised in Table 4.1. The majority of modern continuum dynamic models have evolved from the simple hydrodynamic model first introduced by Savage and Hutter (1989). These models are able to more fully account for behaviours characteristic of rock avalanches, such as the high velocities and strain rates they experience as they propagate across complex 3D terrain (McDougall and Hungr, 2005).

4.2 Rheological laws

Realistically simulating the emplacement dynamics of rock avalanches is complicated by the anisotropic nature of the materials involved, as well as the complex interactions that occur during their highly unsteady and non-uniform flow across steep and irregular terrain (Manzella and Labiouse, 2013). This renders any single material constitutive relationship valid only within a narrow domain of space and time, which limits both the formulation and subsequent incorporation of such laws into a numerical modelling framework (Scheidl *et al.*, 2013). To address some of these challenges, the motion of rock avalanches in models is often governed by a series of simple rheological laws that can vary internally and/or along the path of motion (McDougall, 2006). Depth-averaging in these models allows the rheology to be represented as a single term that expresses the frictional forces occurring at the base of the flow (Luna *et al.*, 2010). Choosing the correct rheological law is therefore crucial, as it governs the run-out distance, thickness, extension and velocity of simulated flows. In most dynamic models, the basal shear stress (τ) is governed by a basal rheological law that may be varied by the user depending on the boundary conditions of the event in question. A number of rheological laws have been invoked for the simulation of rock avalanches, the mathematical expressions for which solve for τ as a function of normal flow depth, density, mean flow velocity and the relevant rheological parameters.

Frictional basal resistance assumes that the basal shear stress is a function only of the effective bed normal stress at the flow base ($\sigma_z{'}$) which is the difference between the total stress (σ_z) and the pore fluid pressure at the base (u):

$$\tau = -(\sigma_z - u)\tan\phi = -\sigma_z' \tan\phi, \qquad\qquad \text{[Eq.4.3]}$$

where ϕ is the dynamic basal friction angle (Ayotte and Hungr, 2000). As pore fluid pressure within

Table 4.1) Summary of the most commonly used dynamic run-out models. Entrainment rates may be defined by the user ('defined') or calculated by a prescribed algorithm that takes into account material properties ('process-based'). Other characteristics are also listed, including the reference frame of the solution, basal rheology and whether or not the model can account for variation of rheology along the flow path. Common rheological laws are summarised in *Section 4.2*.

Model	Reference frame	Rheology	Variation	Entrainment	Reference
Continuum integrated					
FLO-2D	Eulerian	Quadratic	No	None	O'Brien *et al.* (1993)
RAMMS	Eulerian	Voellmy	Yes	Process-based	Christen *et al.* (2010)
3dDMM	Eulerian	Frictional and Voellmy	Yes	Defined	Kwam and Sun (2006)
FLATMODEL	Eulerian	Frictional and Voellmy	No	Process-based	Medina *et al.* (2008)
VolcFlow	Eulerian	Frictional, Voellmy and Bingham	No	Process-based	Kelfoun and Druitt (2005)
RASH3D	Eulerian	Frictional, Voellmy and Quadratic	No	None	Pirulli and Mangeney (2008)
MassMov2D	Eulerian	Voellmy and Bingham	Yes	Defined	Begueria *et al.* (2009)
DAN3D	Lagrangian (meshless)	Frictional, Voellmy and Bingham	Yes	Defined	Hungr and McDougall (2009)
MADFLOW	Lagrangian (mesh)	Frictional, Voellmy and Bingham	No	Defined	Chen and Lee (2007)
TITAN2D	Lagrangian (mesh)	Frictional	No	None	Pitman and Le (2005)
Continuum differential					
TOCHNOG	Differential	Frictional (elastoplastic model)	Yes	Process-based	Crosta *et al.* (2003)
Discrete					
PFC3D	Discrete elements	Inter-particle/particle-wall interaction	No	None	Poisel and Preh (2007)
Cellular automata					
SCIDDICA S3-hex	Eulerian	Energy-based	No	Process-based	D'Ambrosio *et al.* (2003)

a mass movement is difficult to estimate, it is commonly assumed to be related to the total stress by a pore fluid pressure ratio ($r_u = u/\sigma_z$) such that:

$$\tau = -\sigma_z(1 - r_u)\tan\phi \qquad \text{[Eq. 4.4]}$$

Here, r_u and ϕ are rheological parameters that can be defined in the model and can also be expressed as one single variable, the bulk basal friction angle (φ_{bed}):

$$\varphi_{bed} = \arctan(1 - r_u)\tan\phi \qquad \text{[Eq. 4.5]}$$

If r_u is assumed to be constant, Equation 4.4 can be simplified such that:

$$\tau = -\sigma_z\tan\varphi_{bed} \qquad \text{[Eq. 4.6]}$$

A *laminar* or *viscous flow* function is often assumed for the analysis of certain fully liquefied flows, such as granular materials, which resemble Newtonian fluids flowing at a relatively low ratio of inertial to viscous stresses. In laminar flow, shear stresses are directly proportional to the depth-averaged flow velocity (v_d) and dynamic viscosity (η) and inversely proportional to flow depth (h):

$$\tau = -\frac{3\eta v_d}{h} \qquad \text{[Eq. 4.7]}$$

A number of rheological models invoke a velocity-dependent term (Wadge *et al.*, 1998). Flow of water or granular mixtures with a low concentration of solids may transition to a turbulent regime at relatively higher ratios of internal to viscous stresses. *Turbulent flow* is characterised by intense mixing and the associated basal shear stress can be calculated using the Manning equation:

$$\tau = -\frac{\rho g n^2 v_d^2}{h^{\frac{1}{3}}} \qquad \text{[Eq. 4.8]}$$

where n is the Manning roughness coefficient. An alternative to this is the Chézy equation, which relates n to the Chézy coefficient (C) by $C = h^{1/6}/n$:

$$\tau = -\frac{\rho g v_d^2}{C^2} \qquad \text{[Eq. 4.9]}$$

A *plastic* rheology is often used to describe the pseudo-static motion of liquefied soils, which remain at rest while the applied shear stress is below a threshold yield stress. Once movement begins, the shear stress exerted by the material is constant, irrespective of its thickness and/or its velocity (Dade and Huppert, 1998). The basal shear stress is thus assumed to be equal to a constant shear strength:

$$\tau = -c \qquad \text{[Eq. 4.10]}$$

A *Bingham* plastic is a visco-plastic material that behaves as a rigid body below a threshold yield stress (τ_{yield}) but flows as a viscous fluid above (Bingham, 1922). The Bingham constitutive equation is therefore derived by adding a viscous term to a plastic term. The resisting stress is a function of

flow depth, velocity, constant yield strength and the dynamic viscosity, and can be determined through solution of the following cubic equation:

$$\tau^3 = +3\left(\frac{\tau_{yield}}{2} + \frac{\eta v_x}{h}\right)\tau^2 - \frac{\tau_{yield}^3}{2} = 0 \qquad \text{[Eq. 4.11]}$$

The *Voellmy resistance model* takes into account both frictional and turbulent flow behaviours by combining the frictional and Chézy formulae (Voellmy, 1955), such that:

$$\tau = -\left(\sigma_z f + \frac{pg v_x^2}{\xi}\right) \qquad \text{[Eq. 4.12]}$$

where f is the friction coefficient and ξ is the velocity-dependent turbulence parameter. The frictional component of the Voellmy resistance model relates the shear stress to the normal stress and takes the same form as Equation 4.4, where f is analogous to $tan\varphi_{bed}$. The turbulence term can be likened to Manning's n and empirically accounts for all possible sources of velocity-dependent resistance, representing the effect of turbulence and/or collisions during motion (Hutter and Nohguchi, 1990; Evans *et al.*, 2001).

4.3 *VolcFlow*

VolcFlow is a geophysical mass flow code that was originally developed for the dynamic analysis of pyroclastic flows and debris avalanches, but is also suitable for modelling other mass flows including rock avalanches (Kelfoun and Druitt, 2005; Kelfoun *et al.*, 2010). The governing momentum equations are solved using a shock-capturing, finite difference numerical method based on either a single (more stable) or double (more accurate) upwind Eulerian scheme. Upwind schemes are a class of numerical discretisation methods used to solve partial differential equations and are able to handle the shocks and rarefaction waves generated by discontinuous flows and strong variations in fluid flow height (*Section 4.1.2.1*; Mangeney *et al.*, 2000). This means that *VolcFlow* is highly stable even when simulating rapid mass movements across complex topographies and on numerically 'wet' or 'dry' surfaces (Toro, 2001). In addition, the code is able to incorporate two fluids, allowing for the simulation of combined subaerial-submerged events such as the tsunami-generating rock avalanche at Paatuut (*Section 2.2.2*). *VolcFlow* therefore constitutes an important tool for exploring the dynamics of rock avalanches in confined fjord settings, such as Vaigat (*Chapter 2*). A summary of the numerical scheme and its implementation are provided in *Appendix B.* For full details, the reader is referred to Kelfoun and Druitt (2005).

4.3.1 Governing momentum equations

VolcFlow is governed by a series of mass and momentum balance equations based on the depth-averaged (Saint Venant) equations of shallow flow. The governing equations are solved using a shock-capturing, finite difference numerical method based on a single or double upwind Eulerian scheme. With reference to a topography-linked coordinate system, where h is measured normal to the sliding surface, the momentum balance equations are:

$$\frac{\partial h}{\partial t} + \frac{\partial}{\partial x}(hv_x) + \frac{\partial}{\partial y}(hv_y) = 0 \qquad \text{[Eq. 4.13]}$$

$$\frac{\partial}{\partial t}(hv_x) + \frac{\partial}{\partial x}(hv_x{}^2) + \frac{\partial}{\partial y}(hv_x v_y) = gh \sin \alpha_x - \frac{1}{2} k_{actpass} \frac{\partial}{\partial x}(gh^2 \cos \alpha) + \frac{\tau_x}{\rho} \qquad \text{[Eq. 4.14]}$$

$$\frac{\partial}{\partial t}(hv_y) + \frac{\partial}{\partial x}(hv_y v_x) + \frac{\partial}{\partial y}(hv_y{}^2) = gh \sin \alpha_y - \frac{1}{2} k_{actpass} \frac{\partial}{\partial y}(gh^2 \cos \alpha) + \frac{\tau_y}{\rho} \qquad \text{[Eq. 4.15]}$$

where: x and y are local curvilinear coordinates parallel to the ground surface;

ρ is the bulk density of both the landslide and the path material (kg m^{-3});

h is the flow depth (m);

t is time (s);

v_x and v_y are the x and y components of the flow velocity (m s^{-1});

g is the acceleration due to gravity (m s^{-2});

τ is the basal shear stress (kg m^{-1} s^{-2});

α is the local ground slope (°); and

$k_{actpass}$ is the earth pressure coefficient (-).

4.3.2 Basal shear resistance

VolcFlow can account for a number of rheologies, including those summarised in *Section 4.2.* The default equation defining the basal shear stress in *VolcFlow* is:

$$\tau = \rho h \tan \boldsymbol{\varphi_{bed}} \, (v^2 curv + g \cos \alpha) + \boldsymbol{T_0} + \frac{dv}{dh} \boldsymbol{\eta} + \rho v^2 \boldsymbol{coef_{u2}} \qquad \text{[Eq. 4.16]}$$

where: φ_{bed} is the basal friction angle (°);

v is the flow velocity (m s^{-1});

$curv$ is the curvature of the topography in the flow direction;

T_0 is the cohesion (plastic rheology; kg m^{-1} s^{-2});

η is the dynamic fluid viscosity (Bingham viscous rheology; kg m^{-1} s^{-1}); and

$coef_{u2}$ is the collisional stress coefficient (or ξ, Voellmy rheology; -).

The terms in **bold** are to be defined in the model, depending on the boundary conditions.

4.3.3 Pressure terms

The constitutive equation used to calculate the earth pressure coefficient ($k_{actpass}$) in *VolcFlow* states that if the internal behaviour of the sliding mass is frictional:

$$k_{actpass} = 2 \left(\frac{1 \pm \sqrt{1 - \cos^2 \varphi_{int}(1 + \tan^2 \varphi_{bed})}}{\cos^2 \varphi_{int}} \right) - 1 \qquad \text{[Eq. 4.17]}$$

where φ_{int} is the internal angle of friction of the rock or debris avalanche (Iverson and Denlinger, 2001). The minimum and maximum values of the stress coefficients occur when the flow is

extensional (active) and compressional (passive), respectively. This expression is valid if $\varphi_{bed} < \varphi_{int}$. However, if $\varphi_{bed} > \varphi_{int}$, then $k_{actpass}$ is instead given by:

$$k_{actpass} = \frac{1 + \sin^2\varphi_{int}}{1 - \sin^2\varphi_{int}} \qquad \text{[Eq. 4.18]}$$

4.3.4 Previous applications of *VolcFlow*

VolcFlow has been tested on a number of volcanic debris avalanches and pyroclastic flow events, successfully simulating avalanche run-out and emplacement dynamics in a number of settings (Kelfoun and Druitt, 2005; Kelfoun *et al.*, 2008; Kelfoun *et al.*, 2009; Kelfoun *et al.*, 2010; Giachetti *et al.*, 2011; Kelfoun, 2011; Paris *et al.*, 2011; Charbonnier and Gertisser, 2012; Dondin *et al.,* 2012; Giachetti *et al.*, 2012; Charbonnier *et al.*, 2013). Notable results include the successful reproduction of the Socompa debris avalanche deposit, where it reproduced first-order structures such as deposit thickness, extension ridges, levées, distal lobes and the median escarpment, as well as reflected waves resulting from topographically driven secondary flows (Kelfoun and Druitt, 2005; Kelfoun *et al.*, 2008). The stability of the model and its ability to reproduce surface flow features, and thereby replicate flow dynamics, is encouraging and demonstrates model process representation. This is important for a number of applications, including scenario modelling and quantitative risk assessments, which are reliant not only upon the successful prediction of the extent, but also the character, of rock avalanche motion.

4.4 Summary

Studies of rock avalanche dynamics are based, with variable emphases, on theoretical considerations, field observations, laboratory analogue models and computer-based numerical models. Numerical models offer an alternative approach to small-scale analogue modelling and the assessment of events in real-time, constituting an important means for understanding rock avalanche mobility (Hungr, 2006). While empirical run-out models succeed in providing basic levels of run-out prediction, they fail to account for the complex interactions that occur within the rock avalanche mass as it flows across steep and irregular terrain (Manzella and Labiouse, 2013). Accurately simulating these processes instead requires dynamic models, which are physically based. However, successful calibration of these models is reliant upon the careful selection of a series of events with consistent patterns of rheology type and ranges of parameter values, which can then be used to reproduce the behaviour of large groups of similar events. A series of 20 large rock avalanche deposits in Vaigat presents the unique opportunity to do this (*Chapter 2*). Having reviewed the processes and mechanisms involved in rock avalanche emplacement (*Chapter 3*) and the numerical modelling approaches that have been developed to simulate these, a suitable numerical model for answering the research questions posed in *Chapter 1* has been identified. The stability of the geophysical mass flow code *VolcFlow*, and its ability to simulate combined subaerial-submerged events, makes it an important tool for exploring the dynamics of rock avalanches in confined fjord settings such as Vaigat. A framework for calibrating *VolcFlow* and applying this calibration to the rock avalanches in Vaigat will therefore be outlined and discussed in *Chapter 5*.

Chapter 5

Methodology

The successful simulation of rock-slope failure, potential run-out and tsunami propagation in steep fjord environments is contingent upon a thorough understanding of the flow dynamics inferred from deposits left by previous events (Rickenmann, 2005). However, few records exist of multiple rock avalanches with boundary conditions sufficiently consistent to develop a set of more generalised rules for behaviour across events. As discussed in *Chapter 2*, a cluster of 20 large rock avalanche deposits along the Vaigat Strait, West Greenland, presents the opportunity to model a large sample of adjacent events sourced from a stretch of coastal mountains of relatively uniform geology and structure. In addition, the event and corresponding tsunami at Paatuut (AD 2000) represents one of the best-documented events in a confined fjord setting (Pedersen *et al.*, 2002; Dahl-Jensen *et al.*, 2004) and presents an excellent opportunity for calibration of numerical models by back-analysis (*Chapter 4*). As the boundary conditions in this landscape can be taken to be relatively uniform, it is possible to apply this case-specific calibration in order to investigate the variations in dynamics and emplacement style related to variable landslide volume, drop heights and thinning/spreading. This chapter therefore presents the methodology used to provide a calibration of the rheological parameters required to assess the run-out dynamics and emplacement of these rock avalanches. The successive pre-, syn- and post-processing steps required to run and evaluate the Paatuut case are first outlined (*Section 5.1*), followed by the methods used to apply this calibration to the other 19 cases (*Section 5.2*) and details of the sensitivity analyses performed (*Section 5.3*).

5.1 *VolcFlow* model calibration

Numerical simulations of the event at Paatuut (AD 2000) were performed using the geophysical mass flow code *VolcFlow*, which was introduced in *Section 4.3*. The reader is referred to *Appendix B* for details of the model and its numerical scheme, as well as Kelfoun and Druitt (2005) and Kelfoun *et al.* (2010) for full details of the model formulation and implementation. A step-by-step scheme for the calibration procedure used in this work is detailed in *Appendix C*.

5.1.1 Source conditions
5.1.1.1 Defining path topography and source depths

The rock avalanche at Paatuut was simulated on a 25 m resolution Digital Elevation Model (DEM) of the surrounding topography, which was provided by Trine Dahl-Jensen (Geological Survey of Denmark and Greenland; GUES). The pre-event DEM (10 m) was obtained by the GUES from photogrammetric work on a collection of aerial photos taken in 1985 (scale 1:150,000), while the post-event DEM (10 m) was derived from oblique colour stereo-photos taken with a small-

frame camera survey from a helicopter in July 2001 (Dahl-Jensen *et al.*, 2004). Both DEMs were downsampled to 25 m using cubic convolution so that the rheological calibration of *VolcFlow* could be undertaken at a model resolution corresponding to that of the Greenland Mapping Project (GIMP) DEM that covers the Vaigat Strait (Howat *et al.*, 2014).

Estimates of the magnitude and spatial distribution of erosion and deposition at Paatuut were derived by differencing the pre- and post-event DEMs to create a DEM of difference (DoD; James *et al.*, 2012). A mask of the areas where erosion depths were greater than 10 cm was then used to extract post-collapse scar elevations from the 2001 DEM. These elevations were mosaicked onto the 1985 DEM to derive the topography of the sliding surface for input into *VolcFlow*. Vertical erosional depths from the DoD were then extracted and converted into source depths normal to the ground using the cosine of the local slope, as required by the model (Kelfoun, 2014; *pers. comm*; see *Appendix D* for the relevant equations). The path topography and source depths were then gridded using kriging at 25 m spacing and saved for input into *VolcFlow*. These processes are summarised in the schematic diagram shown in Fig. 5.1.

5.1.1.2 Deposit characteristics

A DEM of the observed depositional mass at Paatuut was obtained for comparison with modelled deposits by differencing the pre- and post-event DEMs. The DEM was then smoothed using a 5x5 pixel moving average filter for direct comparison with the smoothed deposits predicted by *VolcFlow* (Fig. 5.1). The maximum run-out, duration of emplacement, maximum velocity, average velocity, maximum deposit depth, average deposit depth, lateral extent at toe, surface area, hypsometric curve (and integral) and the horizontal displacement of the centre of mass of the deposit were all measured for comparison with modelled deposits (Table 5.1). These metrics and a DEM of the simulated deposit, longitudinal transects through the deposit and kinematic measures derived from the literature together constituted the criteria for model validation. Error bands for these measurements were then approximated based on measurement errors, which are also detailed in Table 5.1. These bands constituted a measure of the goodness-of-fit of the model outputs and their use is discussed in *Section 5.1.3*.

Table 5.1) Observed features of the Paatuut event (AD 2000) and the associated deposit. Errors are stated in units of measurement.

* Denotes measurements obtained from Pedersen *et al.* (2002) and Dahl-Jensen *et al.* (2004).

Paatuut		Observation	Error	%
1	Max. run-out (m)	4,383	± 100	± 2%
2	Max. flow velocity (m s^{-1}) *	56	± 20	± 35%
3	Duration of emplacement (s) *	80	± 20	± 25%
4	Max. deposit depth (m)	60	± 5	± 8%
5	Lateral extent at toe (m)	1,325	± 100	± 8%
6	Surface area (m^2)	4,138,971	± 433,750	± 12%
	Hypsometric integral (-)	0.235	-	-
7	COM displacement (m)	2,353	± 100	± 4%
8	Average flow velocity (m s^{-1}) *	37	± 20	± 54%
9	Average deposit depth (m)	18	± 5	± 28%
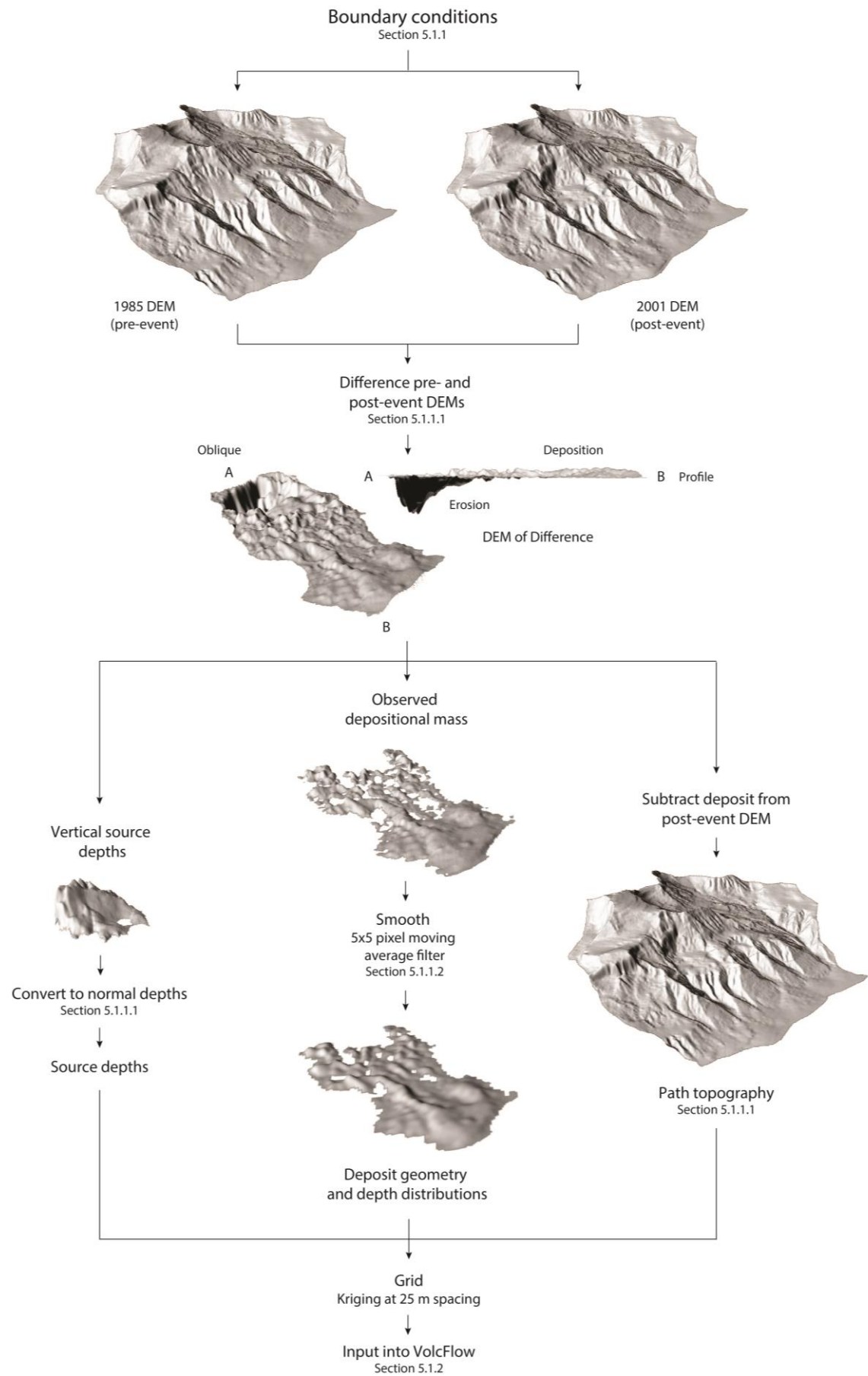
Figure 5.1) Schematic diagram of the steps used to define the source conditions (source depths and path topography) for input into *VolcFlow.* The deposit geometry and depth distributions were used later to validate model outputs.

5.1.2 Input parameters and calibration procedure

To test the ability of simple rheological laws to simulate the dynamics of rock avalanche emplacement, five rheologies were used to simulate the propagation of the event at Paatuut (AD 2000): the Coulomb frictional rheology (1 and 2 equations; simulations 1.# and 2.#), the Voellmy rheology (simulations 3.#), a plastic rheology (simulations 4.#), and a plastic rheology with a velocity-dependent law (simulations 5.#; Table 5.2). These rheologies were chosen as they are those most commonly used to simulate rock avalanche propagation (*Section 4.2*). In total, 41 models were run with the aim of reproducing: (i) the maximum run-out distance reached by the rock avalanche, (ii) the kinematics of the event (e.g. maximum flow velocity and duration of emplacement), and (iii) the first-order morphology of the subaerial rock avalanche deposit, based on the criteria in Table 5.1. The rheological parameters, φ_{bed}, φ_{int}, ξ and T_0, were selected using a systematic approach and adjusted in fixed intervals for each rheology until the model outputs converged as closely as possible with these criteria, as described in *Section 4.1.2.1*. For the Voellmy rheology, φ_{bed} was selected first as to reach the observed distal end of deposition, followed by the adjustment of ξ, which controls the proximal end limit of the deposition and the flow velocity. For the plastic rheology with a velocity-dependent law, T_0 was selected first as to reach the observed distal end of deposition followed by the adjustment of ξ. A diagram of the proximal and distal ends of deposition is shown in Fig. 3.5 (p. 26). Where possible, the calibration procedure was undertaken in keeping with the range of values commonly found in the literature on natural subaerial rock avalanches (e.g. Sosio *et al.*, 2008; Giachetti *et al.*, 2011; Kelfoun, 2011).

All simulations assumed a single collapse of 94×10^6 m^3 of basalt (ρ = 2850 kg m^{-3}) that propagated across dry topography and were ended when the velocity of the flow front reached 0 m s^{-1}. Using the 'en masse sliding' capability in *VolcFlow*, the mass was initially forced to slide as a block before its cohesion decreased with time (see *Appendix E* for the relevant equations). This capability was enabled for the purpose of simulating the early sliding phase of the rock avalanche (Voight and Faust, 1982; Kelfoun, 2014; *pers. comm.*). Entrainment data (e.g. locally eroded depths, erosion rates and lag rate) were unavailable for the Paatuut event and difficulties in coding entrainment laws meant that these processes were not simulated. The collapse of the deposit tongue that originally formed the toe of the rock avalanche emplaced in the Vaigat fjord, which is believed to have triggered the subsequent tsunami (Pedersen *et al.*, 2002), was also not simulated.

5.1.3 Model validation

Selection of the best-fit rheological parameters combined quantitative parameter selection with qualitative user selection. A normalised index, Δ, comparing the modelled and observed measurements for the event characteristics listed in Table 5.1 was calculated for each simulation:

$$normalised\ index\ (\Delta) = \frac{(modelled - observed)}{observed} \times 100 \qquad [\text{Eq. 5.1}]$$

Where positive/negative values indicate an overestimation/underestimation of the investigated characteristic (Mulligan and Wainwright, 2013). The error bounds of each of the observed event characteristics therefore provide a constraint on the goodness-of-fit for all simulations. For

Table 5.2) Summary of simulations and corresponding input parameters (by rheology) used to simulate the event at Paatuut (AD 2000) for the calibration of *VolcFlow*. Numbers in **bold** (e.g. 1.#, 2.#) refer to the number of the simulation (41 in total). All model runs were performed using a single upwind scheme and with en masse sliding enabled, a time step of 0.02 s and a plotting step of 1.0 s. A density of 2850 kg m⁻³ was assumed based on the dominant rock type in the area (basalt; Suckro *et al.*, 2013).

Simulations

Coulomb frictional – 1 equation (φ_{bed})

1.1	**1.2**	**1.3**	**1.4**	**1.5**	**1.6**	**1.7**	**1.8**
20°	19°	18°	17°	16°	15°	14°	13°

Coulomb frictional – 2 equations (φ_{bed}, φ_{int})

2.1	**2.2**	**2.3**	**2.4**	**2.5**	**2.6**	**2.7**	**2.8**	**2.9**	**2.10**	**2.11**	**2.12**
10°, 30°	11°, 30°	12°, 30°	13°, 30°	14°, 30°	15°, 30°	10°, 35°	11°, 35°	12°, 35°	13°, 35°	14°, 35°	15°, 35°

Voellmy (φ_{bed}, ξ)

3.1	**3.2**	**3.3**	**3.4**	**3.5**	**3.6**
13°, 0.1	12°, 0.1	11°, 0.1	15°, 0.01	14°, 0.01	13°, 0.01

Plastic (T_0)

4.1	**4.2**	**4.3**	**4.4**	**4.5**	**4.6**
235 kPa	260 kPa	265 kPa	270 kPa	275 kPa	300 kPa

Plastic with a velocity-dependent law (T_0, ξ)

5.1	**5.2**	**5.3**	**5.4**	**5.5**	**5.6**	**5.7**	**5.8**	**5.9**
250 kPa, 0.01	255 kPa, 0.01	260 kPa, 0.01	250 kPa, 0.005	255 kPa, 0.005	260 kPa, 0.005	200 kPa, 0.05	210 kPa, 0.05	220 kPa, 0.05

example, a model that produced a run-out within the error bounds of the observed maximum run-out (±2%) was judged as an 'excellent' fit. The level at which an 'excellent' fit becomes a 'good' fit is more difficult to distinguish (e.g. McKinnon, 2010), and so in this study a 'good' fit is simply defined as one that is within twice the error bounds of the observed measurement.

In addition to the normalised index for each measure, a DEM, the hypsometric curve and a longitudinal transect was taken through the crest-to-toe centreline of each modelled deposit for comparison with field observations. The hypsometric curve is a non-dimensional measure of the proportion of a landform, typically a catchment, above a given elevation (Strahler, 1964). It can be used as an indicator of the geomorphic form of landforms and therefore constitutes an important criterion for assessing model performance (Willgoose and Hancock, 1998). Together, these measures provided a more holistic view of how well each model was able to replicate the volume and material flux at the toe of the rock avalanches, in some cases immediately prior to their entry into the water. This is critical for accurately simulating the resultant wave generation and propagation, especially in the far field (Kelfoun *et al.*, 2010). These parameters were used, qualitatively, in conjunction with the normalised indices of deposit characteristics to select the best-fit rheological parameters for simulating the Paatuut event, and for later use at other sites.

5.2 Application to other cases (3D and contour-parallel 3D)

Numerical simulations of the other 19 rock avalanches in Vaigat were performed using the best-fit rheological parameters obtained by back-analysis of the Paatuut event (AD 2000). It was not possible to model all 19 cases on 3D topography, and so five events with variable run-out and stalling characteristics were simulated across 3D terrain while the last 14 events were modelled on contour-parallel 3D terrain. These events were chosen on the basis that they are examples of the key event types occurring in Vaigat and include: (i) one event that ran out to sea-level and generated a tsunami, (ii) one event that ran out to sea-level, (iii) one event that stalled on an alluvial fan, (iv) and two events that stalled on and above a major topographic bench. These events are representative of a range of event types occurring in Vaigat. In addition, the events run across contour-parallel 3D terrain provide a test bed for assessing the ability of the model to simulate run-out on a reduced level of topographic complexity. All cases were modelled using the 25 m GIMP DEM (Howat *et al.*, 2014). Step-by-step schemes for defining the source conditions and the procedure for numerical simulations for both sets of cases may be found in *Appendices F* and *G*.

5.2.1 Source conditions

5.2.1.1 Calculating initial source volumes

The failure volumes of the rock avalanches were estimated using the measured present-day volume of the corresponding deposit. The surface areas of the deposits were mapped and their volumes were calculated using the following volume-area scaling:

$$V = 0.05A^{1.5} \qquad\qquad [\text{Eq. 5.2}]$$

which has been successfully applied for bedrock landslides in a number of settings (after: Hovius *et*

al., 1997; Malamud *et al.*, 2004; Larsen *et al.*, 2010). As entrainment was not coded into these models and *VolcFlow* cannot simulate the increase in volume of the mobilised mass due to bulking or fragmentation processes (Kelfoun *et al.*, 2005), the source volume of each event was assumed to be equal to the deposit volume obtained from the DoD. This includes any changes during rock avalanche propagation due to generation of void spaces and general dilation of the mass during flow (McSaveney, 1978; Voight *et al.*, 1983; Sosio *et al.*, 2012).

5.2.1.2 Defining path topography and source depths

3D cases

The pre-collapse topography of the five cases simulated across 3D terrain was estimated by manually interpolating the DEM within the area of the mapped deposit to represent the down slope profile (original topography) of the adjacent topography. This assumes open slope rather than channelised features, but is an optimal approach in the absence of pre-event topography. The volume change between this pre-event DEM and the present-day surface was then calculated and checked against that derived from the volume-area scaling relationship (Equation 5.2). Vertical erosional depths from each DEM of difference were then extracted and converted into source depths normal to the ground, as in *Section 5.1.1.1.* The path topography and source depths for each event were then gridded using kriging at 25 m spacing and saved for input into *VolcFlow*.

Contour-parallel 3D cases

The path topographies of the 14 contour-parallel 3D simulations were estimated using a profile taken along the central deposit axis, which was assumed to be a first order representation of the main streamline of motion. This profile was gridded using 25 m spacing along the down-slope (*X*) and cross-slope (*Y*) axes. An approximation for the average depth of the initial sliding mass was then derived by dividing the deposit volume by the surface area of the scar. The source depth for each event was then gridded by placing the source mass in grid cells that corresponded to the observed scar elevations in the path topography grid. The path topography and source depths for each event were then gridded using kriging at 25 m spacing and saved for input into *VolcFlow*.

5.2.1.3 Deposit characteristics

For each of the five cases simulated across 3D terrain, a DEM of the observed depositional mass was obtained for comparison with modelled deposits by differencing the pre- and post-event DEMs. These deposits then were processed and the observed features measured as described in *Section 5.1.1.2* for the Paatuut case. The reduced complexity of the simulations run across contour-parallel 3D terrain limited the useful data that could be output and validated, and so only the modelled run-out, *H/L*, lateral extent and surface area of each deposit was measured for comparison. This represents a test of the merits of using simplified approaches to modelling rock avalanche run-out across terrain of reduced topographic complexity.

5.2.2 Run-out simulation and model validation

The rheological calibration obtained in *Section 5.1* was applied in 3D and contour-parallel

3D simulations of the remaining 19 rock avalanches that have occurred in the Vaigat. Only the path topography and source depth was varied between model runs, with all other conditions (e.g. material density, en masse sliding, entrainment, time step, plotting step) kept as in *Section 5.1.2*.

The normalised index for the event characteristics listed in Table 5.1 was calculated for each of the five simulations run on 3D topography. A selection of longitudinal profiles comparing the observed and modelled deposit depths were also used for qualitative assessment of model performance. The ability of the model to reproduce the bulk external behaviour (e.g. run-out, *H/L*, lateral extent and surface area) of each of the 20 cases was also assessed; this is especially important as the modelled deposit distributions are strongly affected by the chosen rheology (Pirulli, 2008). To assess overall model performance, and thereby the suitability of a single set of parameters for simulating behaviour across the rock avalanches, a reduced major axis regression was then fit to observed *vs.* modelled values of run-out, *H/L*, lateral extent and surface area. The residuals were plotted against observed values to identify structure in the performance of the modelling.

5.3 Sensitivity analysis

The consistency in primary boundary conditions found across the 20 rock avalanches in Vaigat, including geology, palaeoenvironmental history, first-order order topography, and rock avalanche preparatory and triggering factors, provides a rare opportunity to assess the sensitivity of rock avalanche run-out to changes in key topographic and geometric factors. The ability of the model to reproduce the bulk external behaviour (run-out, *H/L*, lateral extent and surface area) of each of the 20 cases was therefore tested in terms of its sensitivity to a number of factors. The relationship between four primary geometric factors (failure volume, drop height, drop zone angle, slope concavity) and the normalised index of the bulk external characteristics of the rock avalanche deposits was first assessed using a scatter plot matrix. The normalised index of these bulk characteristics was then plotted against the case order of the rock avalanches (1-20, E-W along the Vaigat Strait) to assess any patterns in model under- or over-prediction and to relate these back to the influence of topographic factors and known substrate conditions.

5.4 Summary

This chapter has outlined a framework for calibrating a continuum dynamic flow code, *VolcFlow*, and for applying this calibration to a series of rock avalanches in the Vaigat Strait, West Greenland. The methods detailed in this chapter have been employed for the purpose of investigating:

1) The utility and sensitivity of modelling a single rock avalanche satisfactorily as a function of rheology (*Section 5.1*);

2) The validity of applying the rheological calibration obtained to events elsewhere, within similar boundary conditions (*Section 5.2*); and

3) The performance of the model and its sensitivity to a range of factors (*Section 5.3*).

The results of these procedures will now be presented in *Chapter 6*.

Chapter 6

Results

This chapter presents the results of the calibration and modelling outlined in *Chapter 5*. The characteristics of rock avalanche run-out and the different styles of deposit emplacement observed in the Vaigat Strait are discussed (*RCQ1*). This initial assessment of rock avalanche characteristics in Vaigat is followed by the results of the rheological calibration of *VolcFlow* and a discussion of the ability of the model to successfully back-analyse a well-constrained event (*RCQ2*). The performance of the best-fit rheological calibration when applied to 19 other rock avalanches is then assessed (*RCQ3*) and the sensitivity of the model to a series of topographic and geometric factors is discussed (*RCQ4*).

Section 6.1 first presents an updated map of the south coast of Nuussuaq, West Greenland, showing the 20 rock avalanche deposits that are the focus of this research. The results of a GIS-based analysis of the geomorphometric characteristics of these events, which are also used in later sections, are presented (*RCQ1*).

Section 6.2 presents the results of the rheological calibration of *VolcFlow*. Five rheologies were tested in *Section 5.1* to simulate the propagation of the event at Paatuut (AD 2000), including: the Coulomb frictional rheology (using a one equation and two equation approach), the Voellmy rheology, a plastic rheology, and a plastic rheology with a velocity-dependent law. The overall behaviour of the simulated flows and its relation to each rheology is discussed. For each rheology, longitudinal transects through the modelled deposits are presented alongside a plot of deposit hypsometry and a 3D mesh plot of the best-fit modelled deposit. These are compared to field observations in order to assess the ability of each rheology to reproduce the deposit morphology and distribution observed at Paatuut (*RCQ2*). The relative successes of the chosen rheological laws in simulating the emplacement dynamics of the Paatuut event (AD 2000) are then discussed, and the best-fit rheological parameters for simulating the event are presented.

Section 6.3 presents a series of pairwise comparisons of the modelled and observed results, which together constitute an assessment of the ability of the best-fit rheological parameters to accurately simulate a series of events (*RCQ3*). This is split between the results obtained from six 3D analyses (*Section 6.3.1*) and those from all 20 cases, which includes 14 events simulated across contour-parallel 3D terrain (*Section 6.3.2*). In *Section 6.3.1*, the results of each case simulated across fully 3D terrain are presented alongside a series of lateral and longitudinal transects through the observed and modelled deposits. These are used to assess in detail the ability of the rheological calibration to replicate the behaviour of six of the key types of event occurring in Vaigat, which have variable failure volumes, run-out and stalling characteristics. In *Section 6.3.2* the ability of the model to reproduce the bulk external behaviour (i.e. run-out, apparent coefficient of friction, lateral extent and surface area) of the 20 cases is then assessed using reduced major axis regression of the

observed and modelled values. The normalised index of these bulk characteristics is then plotted against the case order of the rock avalanches (1-20, E-W across the site) and trends are described.

The remarkable consistency in morphological and geophysical conditions across the 20 rock avalanches in Vaigat provides a rare opportunity to assess the sensitivity of rock avalanche run-out to changes in key topographic and geometric factors (*Chapter 2*). *Section 6.4* presents the results of a sensitivity analysis considering the influence of a number of topographic (i.e. situation of the rock avalanche along the Vaigat Strait, profile of the underlying topography) and geometric (i.e. volume, drop height, drop zone angle, slope concavity) factors on model performance. The relative successes of the best-fit rheological calibration for simulating rock avalanche behaviour across a number of events are then identified and the overall performance of the model is discussed (*RCQ4*). The key findings of this chapter are then summarised in *Section 6.5*.

6.1 Rock avalanche characteristics in Vaigat

Field observations and aerial photos taken in 1985 (scale 1:150,000) have shown that the south coast of Nuussuaq is characterised by a series of 20 large rock avalanche deposits (Fig. 6.1), which are identifiable from their geomorphological expression (*Chapter 2*). A GIS-based analysis of the geomorphometric characteristics of these rock avalanches has shown that they are characterised by variable failure volumes, run-out and stalling characteristics (Table 6.1; a full list of these measurements and the associated errors is found in *Appendix H*). Empirical volume-scaling laws applied in *Section 5.2.1* show that the events have each mobilised $>10^6$ m^3 of material, with estimated deposit volumes ranging from $3x10^6$-$94x10^6$ m^3 (Table 6.1). These deposits therefore contain $>350x10^6$ m^3 of material along some 25-30 km of coastline, equivalent to a ca. 2 m drape of sediment across the entire landscape when a 5 km coastal slope is assumed. As discussed in *Chapter 2*, the deposits are likely to have been emplaced since ca. 3000 yr BP based on their relationship with various Holocene sea level markers (Pedersen *et al.*, 2002). The volume of material contained in these deposits is therefore approximately equivalent to 4 mm yr^{-1} of average rockwall retreat.

The run-out of the rock avalanches ranges considerably, from 1,270-4,383 m (Table 6.1). The deposits demonstrate variable stalling characteristics, with some halting on or above a topographic bench or alluvial fan (e.g. events 2-5), some running out to sea level (e.g. events 8 and 9) and some collapsing into the sea, thereby presumably generating tsunami (e.g. events 1 and 16). Events 1, 13 and 14 are characterised by large volumes ($30x10^6$-$94x10^6$ m^3) and long unimpeded run-outs (2,843-4,383 m), resulting in relatively low values of the apparent coefficient of friction *H/L* (0.33-0.40; Table 6.1). However, a smaller subset of these events (2, 3, 4 and 15) are large in volume and instead stall on topographic benches or superimpose onto alluvial fans and stall, resulting in higher values of *H/L* (0.46-0.56; Table 6.1). Although most of these events are characterised by simple and unrestricted run-out paths, they also show a considerable diversity in lateral spreading (113-1,325 m; Table 6.1). These diverse emplacement 'styles' may result from variable failure volumes, drop heights and thinning/spreading, as well as the slope of the path topography and interactions of the flowing mass with rugged terrain and/or deformable substrates (*Chapter 3*), clearly identifying a rationale for exploratory numerical modelling.
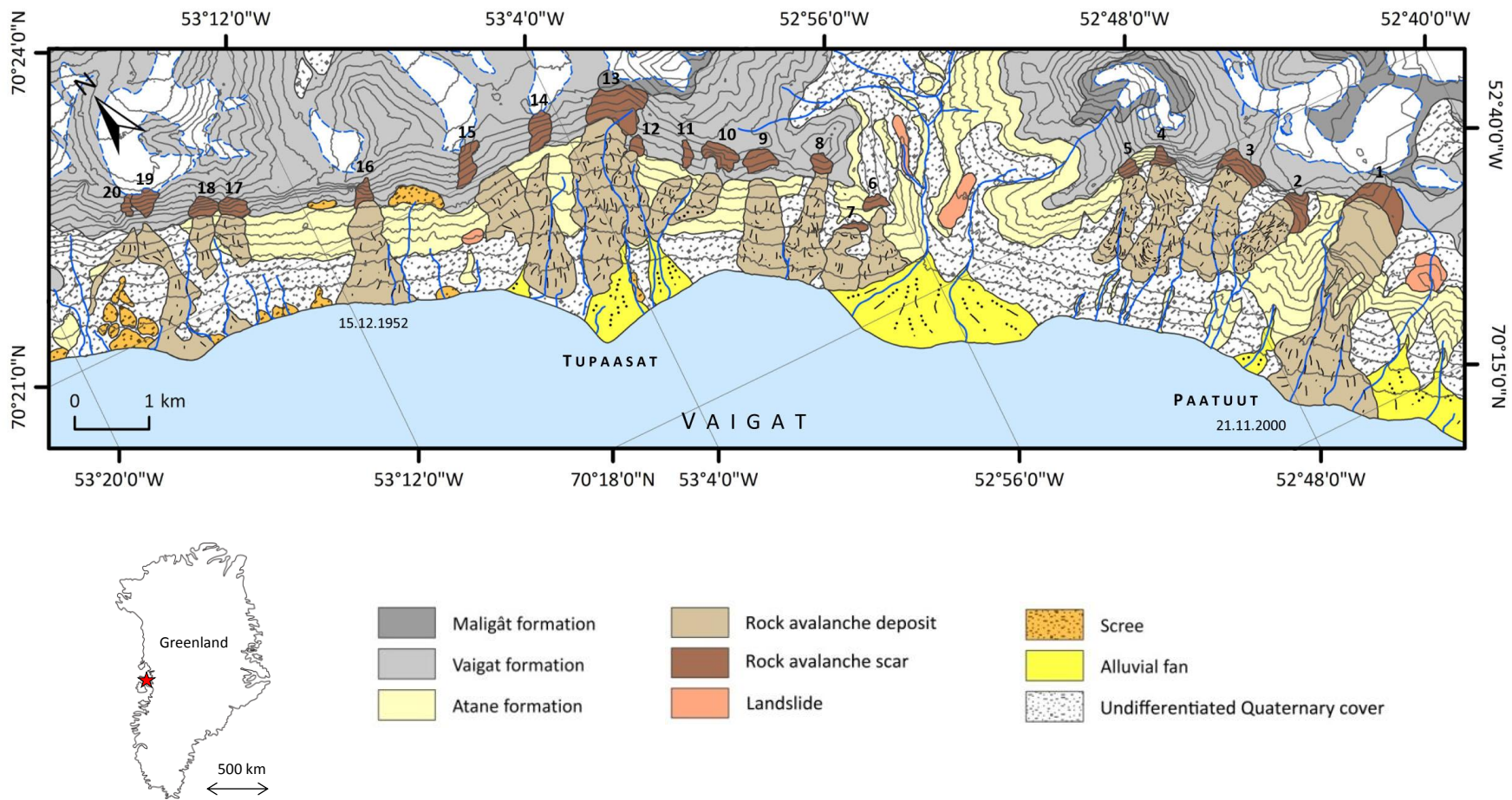
Figure 6.1) Map of the south coast of Nuussuaq, West Greenland, showing 20 large rock avalanche deposits. The events occur over a short length of coastline (ca. 25-30 km) of relatively uniform geology and structure. Contours are drawn in 100 m intervals from the 25 m GIMP DEM (Howat *et al.*, 2014). The events are numbered 1-20, E-W across the site, and their geometric characteristics are summarised in Table 6.1.

Table 6.1) The observed geometric characteristics associated with each event. Each event is given a number, ordered from 1-20 (E-W across the site), and is referred to by this number throughout the rest of this work. Deposit volumes were calculated using the volume-area scaling detailed in *Section 5.2.1*. Run-out and lateral extent at the toe were measured using aerial photographs (scale 1:150,000; *Section 5.1.1*). The total vertical drop height (*H*) and apparent coefficient of friction (*H/L*) were measured as defined in *Chapter 3.* The concavity index for each event represents the ratio between the integral of a longitudinal profile of the path topography and a straight line fit through that topography, indicating relative concavity. A value of 1.00 therefore constitutes a planar slope, with decreasing values of the index representing a progressive increase in slope concavity. The approximate angle of each drop zone was measured by masking and averaging the slope map of the scar in question. All measurements given to the appropriate number of significant figures. See *Appendix H* for details and a full list of these measurements and the associated errors.

Event	Notes	Deposit							Scar	
		Surface area (*A*; m²)	Volume (*V*; x10⁶ m³)	Run-out (*L*; m)	Lateral extent (m)	*H* (m)	*H/L* (-)	Concavity Index (-)	Drop zone angle (°)	Surface area (m²)
1	Paatuut (AD 2000) – tsunamigenic	4,138,000	94	4,383	1,325	1,470	0.33	0.71	61	411,000
2	Stalls above bench (1)	997,000	11	2,084	312	970	0.46	0.95	70	225,000
3	Stalls above bench (2)	1,577,000	22	1,927	674	970	0.50	0.91	69	284,000
4	Stalls at bench (elevation 330-350 m asl)	1,930,000	30	2,843	650	1,100	0.39	0.77	75	98,000
5	Stalls above bench (3)	736,000	7	1,740	440	860	0.49	0.82	67	94,000
6	Superimposed onto alluvial fan (1)	651,000	6	1,501	1,070	630	0.42	0.95	48	96,000
7	Superimposed onto alluvial fan (2)	669,000	6	1,270	618	400	0.32	0.91	43	55,000
8	Runs out to sea level (1)	1,037,000	12	2,340	396	990	0.42	0.79	46	118,000
9	Runs out to sea level (2)	1,295,000	16	2,416	958	970	0.40	0.74	53	201,000
10	Tupasaat – stalls above alluvial fan (1)	603,000	5	1,821	736	840	0.46	0.73	72	225,000
11	Tupasaat – stalls above alluvial fan (2)	504,000	4	1,848	180	810	0.44	0.88	40	74,000
12	Tupasaat – stalls above alluvial fan (3)	739,000	7	1,995	233	660	0.33	0.86	35	75,000
13	Tupasaat – long run-out, stalls above alluvial fan	2,424,000	42	3,710	370	1,240	0.33	0.73	48	655,000
14	Tupasaat – runs out to sea level	2,096,000	34	3,196	921	1,280	0.40	0.62	56	249,000
15	Adjoining to (14) – stalls at bench	965,000	11	2,107	279	1,190	0.56	0.82	56	227,000
16	1952 event – tsunamigenic	1,409,000	19	2,345	1,028	1,130	0.48	0.79	77	114,000
17	Small event – stalls at bench (1)	405,000	3	1,313	281	970	0.74	0.82	62	165,000
18	Small event – stalls at bench (2)	398,000	3	1,550	122	980	0.63	0.76	66	157,000
19	Runs out to sea level	1,477,000	20	3,129	1,214	1,450	0.46	0.61	57	171,000
20	Stalls at bench - channelised	633,000	6	2,320	113	1,330	0.57	0.58	55	62,000

6.2 Rheological calibration

Over 40 simulations of the Paatuut event (AD 2000) were performed in *VolcFlow* varying the rheological parameters used to define the shear stress at the base of the rock avalanche. The rheological parameters, φ_{bed}, φ_{int}, ξ and T_0, required for the back-analysis were selected using a trial-and-error approach and adjusted in fixed intervals for each rheology as described in *Section 5.1*. Table 5.2 (p. 43) shows the ranges of parameter values used. For the frictional and Voellmy rheologies, which are commonly used to model rock avalanches, the calibration procedure was undertaken in keeping with the range of values found in the literature (e.g. φ_{bed} = 10-30°, φ_{int} = 30-40°; Sosio *et al.*, 2008; Giachetti *et al.*, 2011; Kelfoun, 2011). The parameters and results of the best-fit simulation for each rheology are summarised in Table 6.2 and discussed in the following sections. The parameters and results of each individual model run are listed in full in *Appendix I*.

Table 6.2) Parameters and results of the best-fit simulation for each rheology. All model runs were performed using a single upwind scheme and with en masse sliding enabled, assuming a density of 2850 kg m^{-3}, with a time step of 0.02 s and a plotting step of 1.0 s. Numbers in brackets represent the normalised index, Δ, which compares the modelled and observed measurements for each output (as calculated in *Section 5.1.3*).

Paatuut	Rheology				
	Frictional (1 angle)	**Frictional (2 angles)**	**Voellmy**	**Plastic**	**Plastic + u^2**
Mechanical behaviour					
Density (kg m^{-3})	2850	2850	2850	2850	2850
Basal friction angle, φ_{bed} (°)	14	12	13	-	-
Internal friction angle, φ_{int} (°)	-	30	-	-	-
Collisional stress coefficient, ξ (-)	-	-	0.01	-	0.01
Cohesion (kPa)	-	-	-	270	250
Model outputs					
Max. run-out (m)	**4,503**	**4,319**	**4,134**	**4,334**	**4,368**
	(+3%)	(-2%)	(-6%)	(-1%)	(-0.3%)
Max. flow velocity (m s^{-1})	**89**	**100**	**48**	**72**	**66**
	(+59%)	(+79%)	(-14%)	(+29%)	(+18%)
Duration of emplacement (s)	**184**	**249**	**243**	**87**	**92**
	(+130%)	(+211%)	(+204%)	(+9%)	(+15%)
Max. deposit thickness (m)	**106**	**111**	**110**	**71**	**72**
	(+77%)	(+85%)	(+83%)	(+18%)	(+20%)
Lateral extent at toe (m)	**1,353**	**984**	**1,546**	**821**	**1,101**
	(+2%)	(-39%)	(+17%)	(-38%)	(-17%)
Surface area (m^2)	**5,579,375**	**4,155,625**	**4,898,750**	**4,563,125**	**4,545,000**
	(+35%)	(+0.4%)	(+18%)	(+10%)	(+10%)
Hypsometric integral (-)	**0.138**	**0.100**	**0.150**	**0.272**	**0.269**
	(-41%)	(-57%)	(-36%)	(+16%)	(+14%)
X-displacement of the centre of mass (m)	**1,617**	**308**	**1,885**	**1,694**	**1,776**
	(-31%)	(-87%)	(-20%)	(-28%)	(-25%)
Average flow velocity (m s^{-1})	**25**	**29**	**7**	**10**	**19**
	(-32%)	(-22%)	(-81%)	(-73%)	(-49%)
Average deposit thickness (m)	**15**	**11**	**16**	**19**	**19**
	(-17%)	(-39%)	(-11%)	(+6%)	(+6%)

6.2.1 Coulomb frictional rheology (one equation)

In all simulations the acceleration of the source mass following collapse was relatively slow (ca. 10 m s^{-1}) as it flowed across a platform (ca. 6-7°) at the base of the escarpment (ca. 800-900 m asl; Fig. 6.2). At greater basal frictional angles (i.e. 17-20°) the mass accumulated over a very limited distance, with much of the source mass stalled on the plateau, as seen in the depth profiles presented in Fig. 6.2a. As a result, these parameterisations greatly underestimate the average velocity of the rock avalanche and thereby the run-out, lateral extent and surface area of the resultant deposit. The run-out of the event is more satisfactorily simulated at lower basal friction angles (i.e. 13-15°), with the best-fit model simulating the event to within ±3% of the observed run-out (φ_{bed} = 14°; Table 6.2). For these cases, a higher proportion of the mass was able to leave the source area and flow through the gullies in the Atane Formation (ca. 300-900 m asl) before forming a sheet-like deposit with a rounded frontal lobe and gentle downstream slopes due to inertia of the flow (Figs. 6.2c and 6.3a). In all cases, the hypsometry of the modelled deposits is characterised by a smaller proportion of areas at shallow deposit depths compared to the observed deposit (Fig. 6.2b), as much of the mass accumulated to great depths (ca. 80-120 m) in the source area and gullies, with only thin debris sheets flowing over the alluvial fan (below ca. 300 m asl). Although the best-fit Coulomb frictional model is successful in reproducing run-out at Paatuut, it is unable to sufficiently replicate the deposit morphology and kinematics of the event and greatly overestimates the maximum velocity (Δ = +59%) and duration of emplacement (Δ = +130%), and underestimates the average velocity (Δ = -31%) of the flow (Table 6.2).
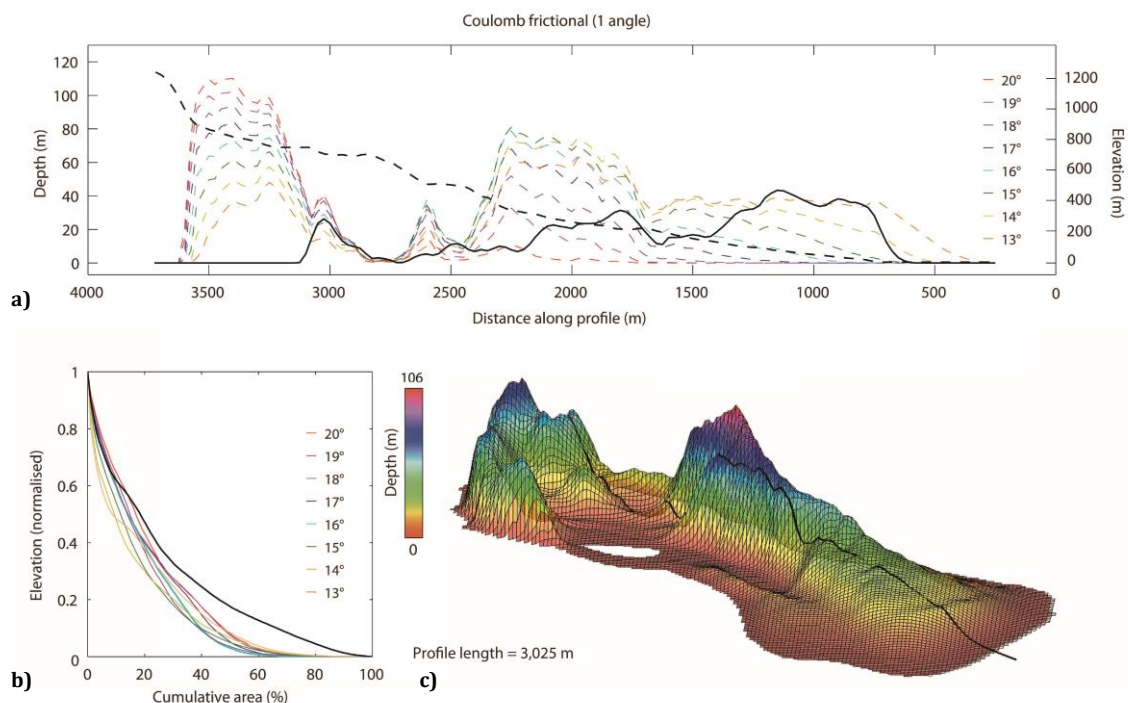
Figure 6.2) a) Longitudinal transects through the observed (solid black line) and modelled deposits (coloured lines) for the Coulomb frictional rheology (one equation). The dashed black line represents the elevation of the path topography along the same profile, **b)** normalised hypsometric curves for the observed (solid black line) and modelled deposits (coloured lines), and **c)** oblique view 3D mesh plot and transect (solid black line) of the best-fit modelled deposit. Note the concentration of the deposited mass in the proximal and medial reaches.
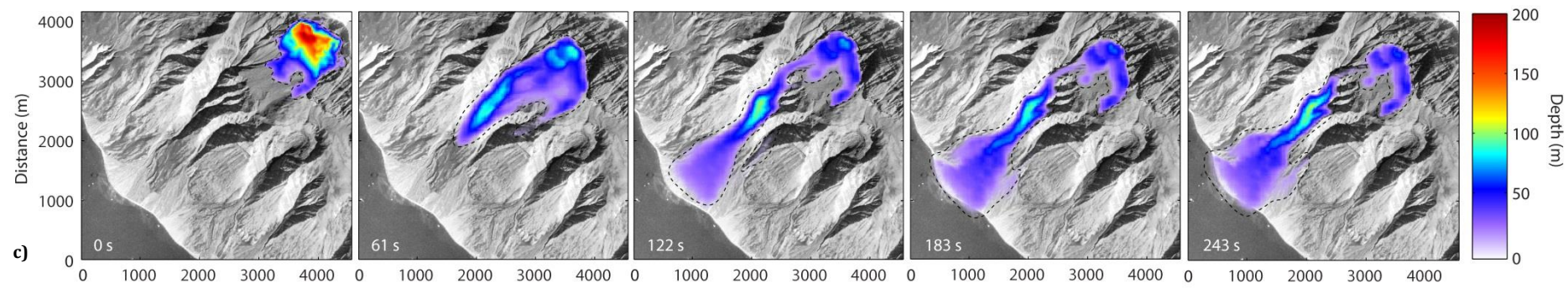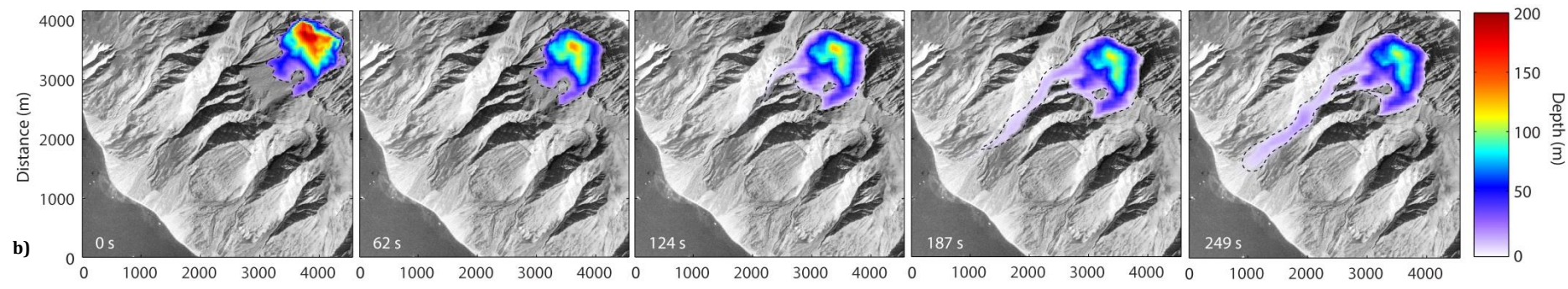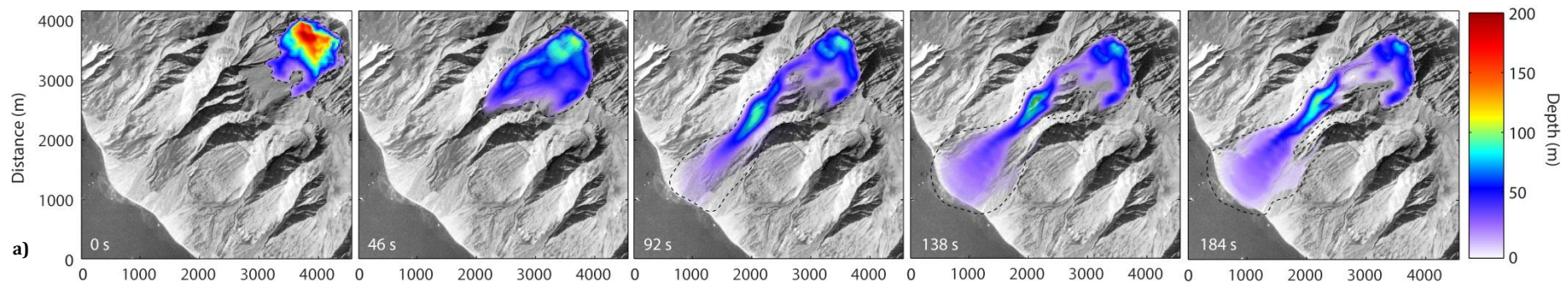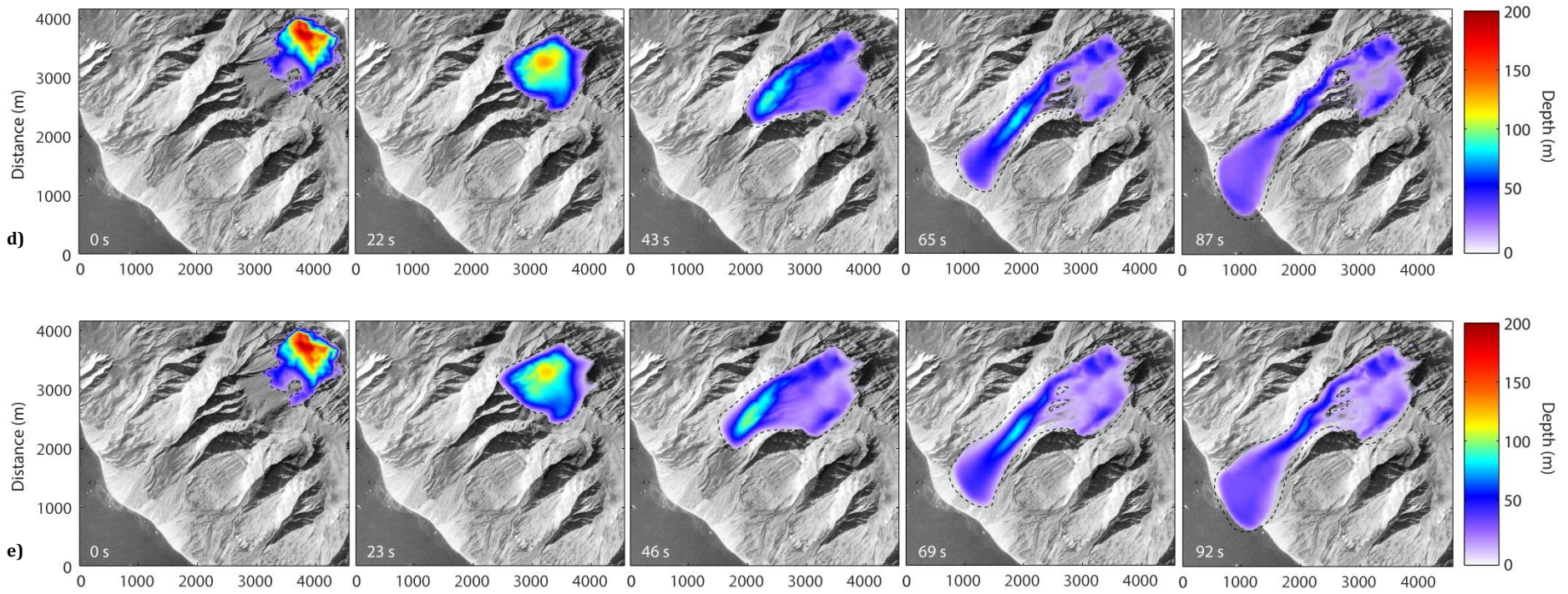
Figure 6.3) Simulated emplacement of the event at Paatuut (AD 2000) using the best-fit model for **a)** a Coulomb frictional rheology (1 equation), **b)** a Coulomb frictional rheology (2 equations), **c)** a Voellmy rheology, **d)** a plastic rheology, and **e)** a plastic rheology with a velocity-dependent law. Snapshots were taken at 0%, 25%, 50%, 75% and 100% of the total simulation time. See text for full discussion.

6.2.2 Coulomb frictional rheology (two equations)

When only the basal friction angle (φ_{bed}) is defined, as above, the internal friction of the flowing material, φ_{int}, implicitly equals φ_{bed} and the internal stresses of the flow are considered to be isotropic (i.e. $k_{actpass}$ = 1). In a two equation frictional law φ_{int} differs from φ_{bed}, thereby acting on $k_{actpass}$, the earth pressure coefficient and modifying the stresses induced by the pressure gradient (*Section 4.3*). This allows for strain-dependent, anisotropic internal stresses that arise due to the 3D deformation of material during topographically steered flow (McDougall and Hungr, 2004).
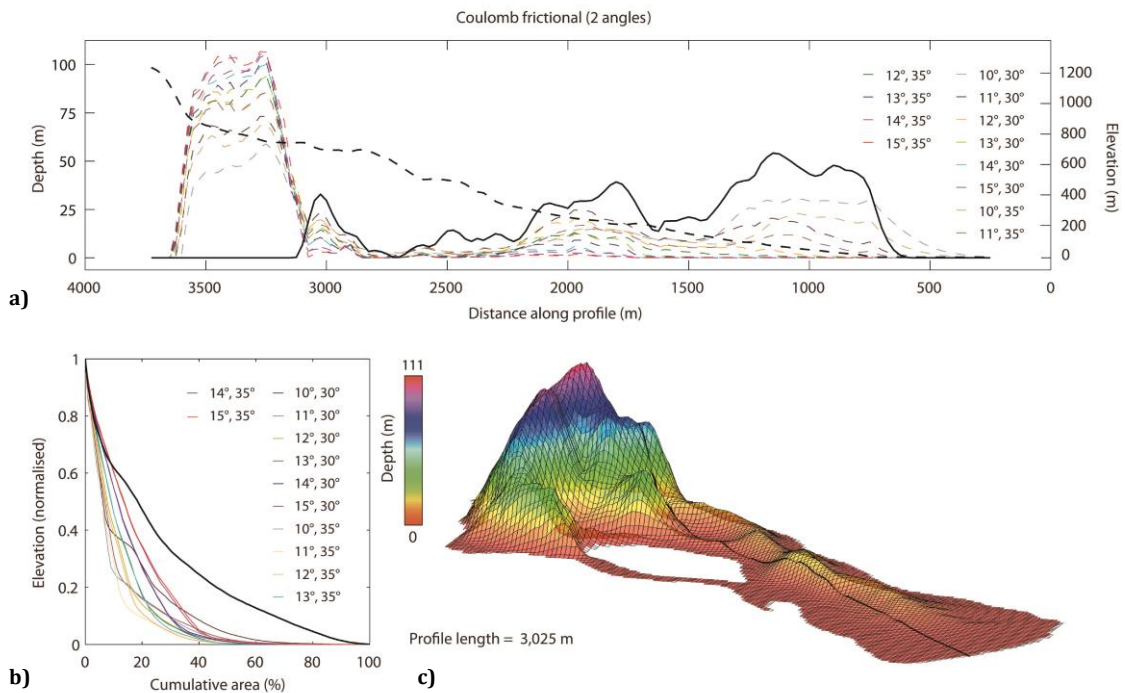
Figure 6.4) a) Longitudinal transects through the observed (solid black line) and modelled deposits (coloured lines) for the Coulomb frictional rheology (two equations). The dashed black line represents the elevation of the path topography along the same profile, **b)** normalised hypsometric curves for the observed (solid black line) and modelled deposits (coloured lines), and **c)** oblique view 3D mesh plot and transect (solid black line) of the best-fit modelled deposit.

In all cases the flowing mass behaved similarly to the previous set of simulations. However, as $\varphi_{int} > \varphi_{bed}$, the motion of flow was strongly opposed and the deposits were therefore emplaced closer to the source, forming thinning deposits (Figs. 6.3b and 6.4a). The hypsometry of the modelled deposits is characterised by a smaller proportion of areas at shallow depths in comparison to the observed deposit, as the majority of the source mass remained stalled on the plateau (Fig. 6.4b). Although the best-fit model is able to simulate the event to within ±2% of the observed run-out (φ_{bed} = 12°, φ_{int} = 30°), the simulated flows were emplaced slowly (Δ = +211%) and the model fails to replicate the horizontal displacement of the centre of mass observed in the field (Δ = -87%; Table 6.2). The run-out extent and spreading simulated by the model was only achieved by a fraction of the failed mass as a result of strong spreading of the frontal wedge by inertia, as shown by the mesh plot in Fig. 6.4c. Although several of the flows shown here are able to adequately reproduce the extent of run-out at Paatuut, combining a realistic internal friction angle (30° or 35°) with any realistic basal friction angle (10-15°) fails to reproduce the initial collapse of the source mass, the kinematics of the event or the overall morphology of the resultant deposit.

6.2.3 Voellmy rheology

The Voellmy rheology adds a collisional stress coefficient (ξ), which depends on the square of the flow velocity, to the Coulomb frictional model. With this additional velocity-dependent stress the basal friction angle must be lowered to reach the equivalent run-outs simulated in *Section 6.2.1*, where a simple Coulomb frictional law was assumed. As in previous simulations, the acceleration of the source mass following collapse was slow (Fig. 6.3c). However, the addition of ξ incorporates the effects of turbulence and/or collisions within the flow, reducing its maximum velocity and constituting a better fit than that simulated by either of the frictional laws (Δ = -14%; Table 6.2). The lower inertia of a Voellmy flow in comparison to a Coulomb flow allows the mass to accumulate closer to the point where the topographic slope equals φ_{bed} (Fig. 6.5a). A greater proportion of the collapsed mass was therefore able to flow out of the source area before being channelled through the gullies in the Atane Formation and out onto the alluvial fan below, as seen by the deposit morphology mesh plot in Fig. 6.5c. The deposits modelled assuming a Voellmy rheology therefore accumulated at greater thicknesses in the medial and distal reaches, which is in agreement with field observations at Paatuut (*Chapter 2*). In contrast to the hypsometry of the deposits emplaced by Coulomb flows, the hypsometry of deposits modelled using a Voellmy rheology begins to converge with the morphology of the observed deposit (Fig. 6.5b). Although the best-fit model fails to simulate the extent of the run-out as closely as the Coulomb frictional models (Δ = -6%; φ_{bed} = 13°, ξ = 0.01), it can better simulate the distribution of the resultant deposit and can also more accurately reproduce the horizontal displacement of the centre of mass (Δ = -20%), lateral extent (Δ = +17%) and average depths of the deposit (Δ = -11%; Table 6.2).
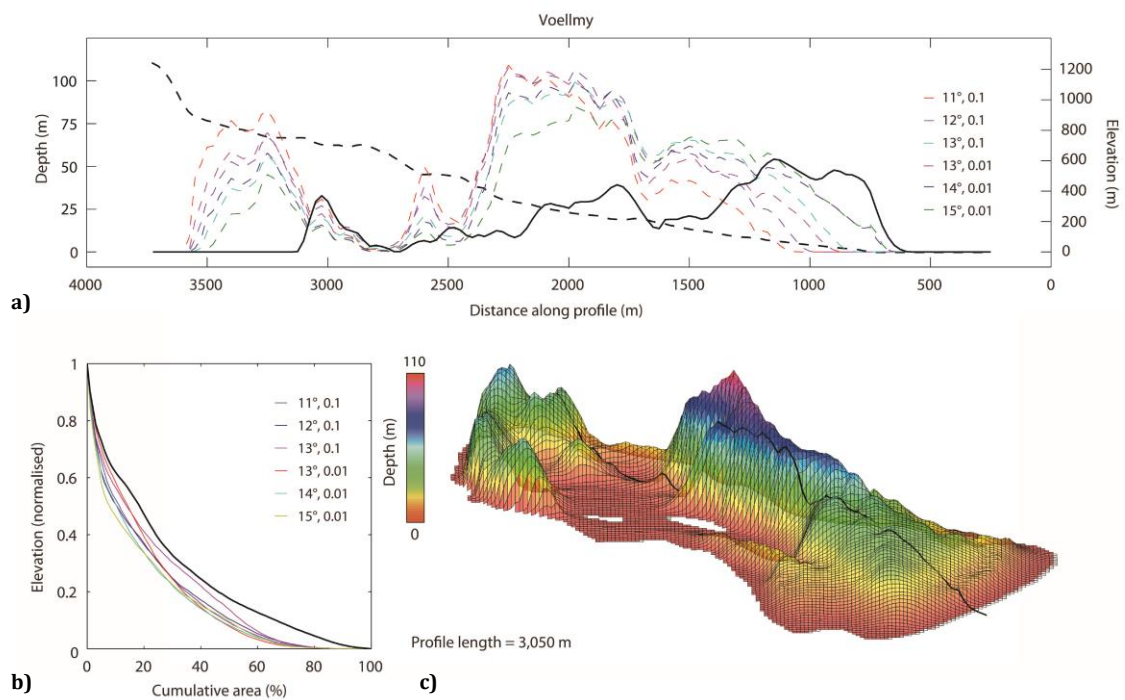
Figure 6.5) a) Longitudinal transects through the observed (solid black line) and modelled deposits (coloured lines) for the Voellmy rheology. The dashed black line represents the elevation of the path topography along the same profile, **b)** normalised hypsometric curves for the observed (solid black line) and modelled deposits (coloured lines), and **c)** oblique view 3D mesh plot and transect (solid black line) of the best-fit modelled deposit.

6.2.4 Plastic rheology

The plastic rheology assumes a constant retarding stress, T_0, which is independent of the depth or velocity of the flow. In all cases the acceleration of the source mass following collapse was slow as it flowed across the platform at the base of the escarpment (Fig. 6.3d). Lateral confinement by gullies caused the flow to deepen, thereby increasing the driving stress. The flowing mass then began to accelerate rapidly, reaching a maximum flow velocity close to that estimated from seismic records in AD 2000 (Δ = +29%, Table 6.2; Pedersen *et al.*, 2002). As the mass flowed out onto the alluvial fan it thinned, lowering the driving stress to below T_0 and thus causing the flow to quickly decelerate, achieving a run-out within ±1% of the observed distance (best-fit: T_0 = 270 kPa; Table 6.2). Previous simulations above have overestimated the relatively short duration of the event, which is best simulated with a plastic flow (Δ = +9%; Table 6.2). In all cases, the deposits emplaced using a plastic rheology are sheet-like on all slopes and form a rounded frontal lobe with a well-defined flow front (Fig. 6.6), in keeping with field observations (*Chapter 2*). The plastic rheology therefore replicates the kinematics of the event and the morphology of the resultant deposit well, with close fits also obtained for the horizontal displacement of the centre of mass (-28%), average and maximum deposit thickness (+6% and +18%) and surface area (+10%; Table 6.2).
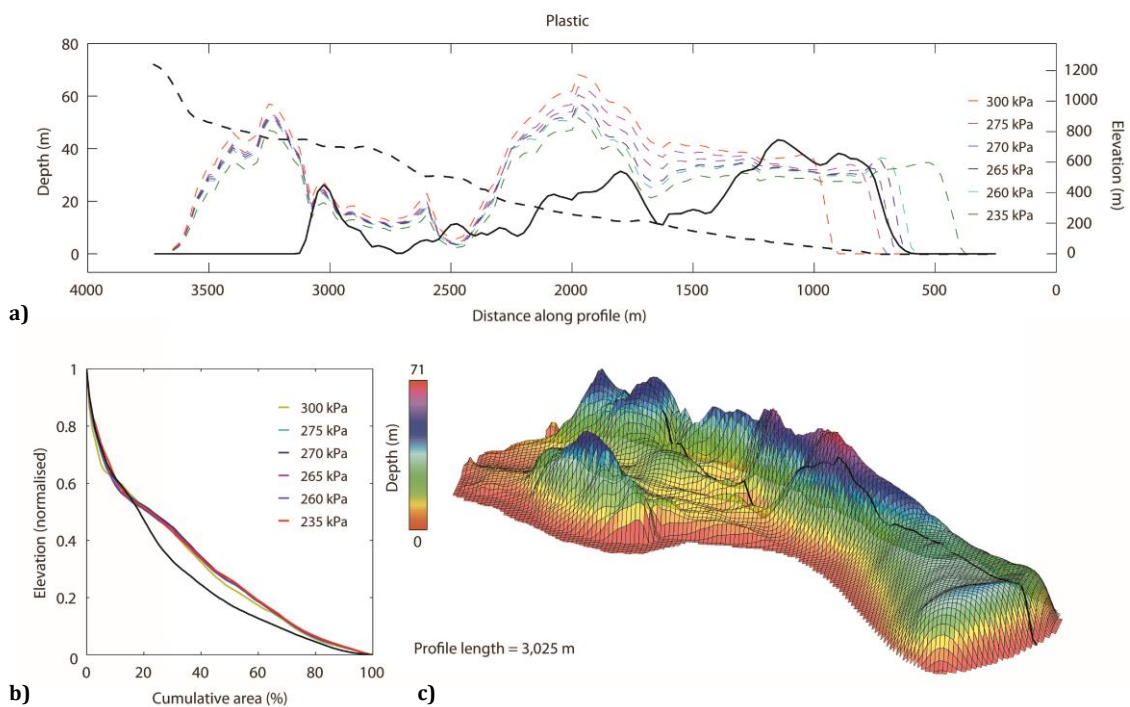
Figure 6.6) a) Longitudinal transects through the observed (solid black line) and modelled deposits (coloured lines) for the plastic rheology. The dashed black line represents the elevation of the path topography along the same profile, **b)** normalised hypsometric curves for the observed (solid black line) and modelled deposits (coloured lines), and **c)** oblique view 3D mesh plot and transect (solid black line) of the best-fit modelled deposit.

6.2.5 Plastic rheology with a velocity-dependent law

The addition of a velocity-dependent term (ξ) to the plastic rheology is principally to reduce the velocity of the flow. With this additional velocity-dependent stress the best-fit value of the constant retarding stress obtained in the previous section must be lowered to achieve the

observed run-out. The maximum velocity of a flow simulated with this rheology is therefore reduced and is a closer fit to that derived using the seismic records (Δ = +18%; Pedersen *et al.*, 2002). In all cases the flowing mass behaved in a similar manner to the previous set of simulations, and the morphology of the modelled deposits share the characteristics modelled with a purely plastic flow: a progressive increase in deposit depth as the slope of the path topography decreases, and a rounded frontal lobe (Figs. 6.3e and 6.7). A number of combinations of T_0 and ξ were tested, with the best-fit model simulating the event to within ±0.3% of the observed run-out (T_0 = 250 kPa, ξ = 0.01; Table 6.2). The kinematics of the event and the morphology of the resultant deposit are simulated most closely when a collisional stress coefficient is added to the plastic model, which yields a closer overall fit between the observed and modelled event characteristics and deposit distribution (Fig. 6.7; Table 6.2). This rheology is most successful in reproducing the event kinematics, deposit mass distribution and deposit morphology to justify the assumption that it represents, to the first order, the dominant features of the emplacement dynamics.
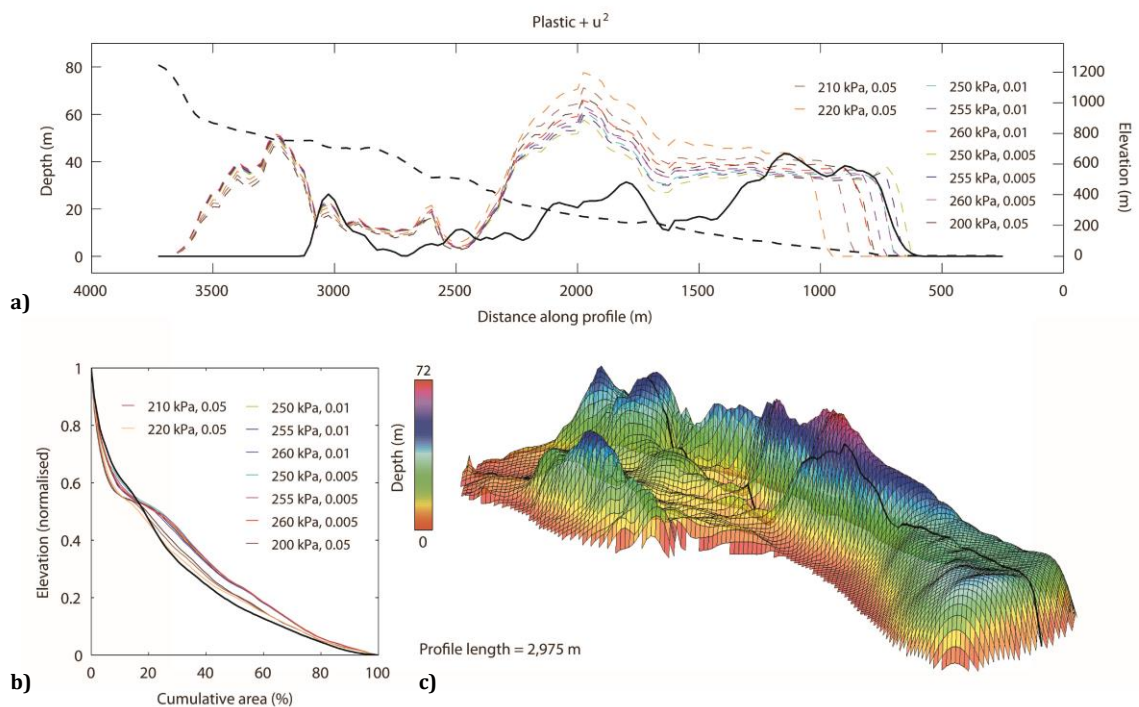
Figure 6.7) a) Longitudinal transects through the observed (solid black line) and modelled deposits (coloured lines) for the plastic rheology with a velocity-dependent law added. The dashed black line represents the elevation of the path topography along the same profile, **b)** normalised hypsometric curves for the observed (solid black line) and modelled deposits (coloured lines), and **c)** oblique view 3D mesh plot and transect (solid black line) of the best-fit modelled deposit.

6.3 Model performance

6.3.1 Application to other 3D cases

Five other rock avalanches in Vaigat were simulated across fully 3D model terrain using the best-fit rheological calibration obtained in *Section 5.1* (T_0 = 250 kPa, ξ = 0.01). These tests were performed to assess the ability of the model to translate to five further events with variable deposit volumes (5×10^6-94×10^6 m^3), run-out (1,821-4,383 m) and stalling characteristics (Table 6.1). These were chosen on the basis that they each represent a different emplacement style of event occurring

in Vaigat and include: (i) an event that ran out to sea-level and generated a tsunami (16), (ii) an event that ran out to sea-level (14), (iii) an event that stalled on an alluvial fan (10), (iv) and two events that stalled on and above a major topographic bench, respectively (4 and 2).

In general the morphology of the resultant deposits is simulated well, and the model yields a close overall fit between the observed and modelled event characteristics and the associated depths (Table 6.3). A realistic simulation of the observed run-out was obtained for five of the events, with all bar one event (10) modelled to within ±2% of the observed run-out (Table 6.3). The distribution of mass in the deposits was also simulated reasonably well, with the horizontal displacement of the centre of mass that took place during events 2, 4, 14 and 16 simulated to within ±12% of the observed displacement (Table 6.3). The model failed, however, to adequately simulate the event characteristics of the smallest event, event 10 (5×10^6 m^3), which ran out and stalled above an alluvial fan at Tupaasat (Fig. 6.1; Table 6.3).

A number of the deposits, particularly those emplaced by events 1, 2, 4 and 16, are characterised by a convex upper deposit surface, steep fronts and sides close to the angle of repose (Fig. 6.8). The toe morphology of these deposits is reproduced particularly well, as shown by the longitudinal transects in Fig. 6.8. The overall distribution of deposit depths is also simulated well, with those emplaced by events 2, 4 and 16 closely approximating those of the observed deposits, within error (Fig. 6.9). In addition, several of these events (2, 4 and 10) are correctly simulated to stall at or above a major topographic bench (Fig. 6.9). However, in all cases, deposition is simulated along the full extent of the run-out path, while the observed deposits were only emplaced in the medial and distal reaches with little of the mass remaining stalled in the source area (Fig. 6.9).

Cross-slope transects taken through the toe of each deposit show that the lateral depth distribution is also simulated well, with the deposits emplaced by events 2, 4, 10 and 14 closely approximating those of the observed deposits, within error (Fig. 6.10). In these cases, the lobes of the observed and modelled deposits are shown to have developed in response to the underlying topography, with evidence of upslope thinning (1), hole filling (2), and pinching out of the deposit at topographic highs (3) all apparent (Fig. 6.10). This suggests that the model can plausibly account for the observed morphology of a series of deposits emplaced by a range of event types. Thus far, the model shows encouraging results in its ability to simulate a series of events of variable
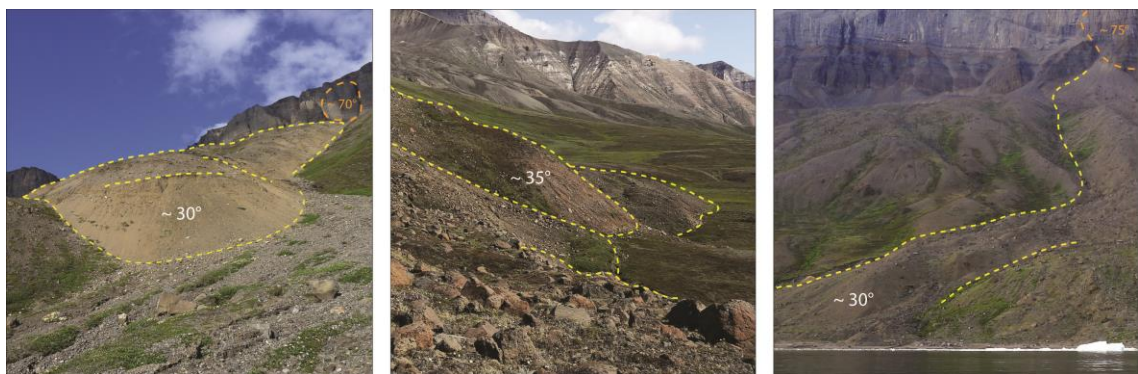
Figure 6.8) Left:deposits emplaced by event 2. Centre: lobate deposits emplaced by event 4. Right: deposits emplaced by the 1952 event (16). In all cases the deposit consists of a complex of partially overlapping and anatomising lobes. Near their terminations the deposits are thick and have slopes close to the angle of repose. The surface of the deposits emplaced by the 1952 event are also characterised by conical mounds of debris, or 'molards', which can be seen in the foreground.

Table 6.3) Results of the simulations run using the best-fit rheological calibration obtained in *Section 5.1* (plastic rheology with a velocity-dependent law; T_0 = 250 kPa, ξ = 0.01). All model runs were performed using a single upwind scheme and with en masse sliding enabled, assuming a density of 2850 kg m^{-3}, with a time step of 0.02 s and a plotting step of 1.0 s. Numbers in **bold** represent the case order number assigned to the rock avalanche shown in *Section 6.1*. Numbers in brackets represent the normalised index, Δ, which compares the modelled and observed measurement for each output (as calculated in *Section 5.1.3*).

| Rock avalanche	1		2		4		10		14		16	
	Observed	Modelled	Observed	Modelled	Observed	Modelled	Observed	Modelled	Observed	Modelled	Observed	Modelled
Max. run-out (m)	4,383	4,368	2,084	2,060	2,843	2,829	1,821	1,643	3,196	3,123	2,345	2,299
	-	(-0.3%)	-	(-1%)	-	(-0.5%)	-	(-9%)	-	(-2%)	-	(-2%)
Max. flow velocity (m s^{-1})	56	66	-	61	-	83	-	36	-	64	-	59
	-	(+18%)	-	-	-	-	-	-	-	-	-	-
Duration of emplacement (s)	80	92	-	52	-	50	-	59	-	61	-	54
	-	(+15%)	-	-	-	-	-	-	-	-	-	-
Max. deposit thickness (m)	60	72	24	22	35	25	51	72	42	34	24	27
	-	(+20%)	-	(-8%)	-	(-28%)	-	(+41%)	-	(-19%)	-	(+12%)
Lateral extent at toe (m)	1,325	1,101	312	241	650	702	736	716	921	889	1,028	1,055
	-	(-17%)	-	(-23%)	-	(+8%)	-	(-3%)	-	(-4%)	-	(+3%)
Surface area (m^2)	4,138,000	4,545,000	997,000	1,120,625	1,930,000	2,233,125	603,000	804,375	2,096,000	2,294,375	1,409,000	1,773,125
	-	(+10%)	-	(+12%)	-	(+16%)	-	(+33%)	-	(+9%)	-	(+26%)
Hypsometric integral (-)	0.235	0.269	0.417	0.447	0.355	0.389	0.393	0.239	0.324	0.361	0.339	0.348
	-	(+14%)	-	(+7%)	-	(+8%)	-	(-39%)	-	(+11%)	-	(+3%)
X-displacement of the centre of mass (m)	2,353	1,776	957	843	1,558	1,373	873	667	1,473	1,448	1,394	1,302
	-	(-25%)	-	(-12%)	-	(-11%)	-	(-24%)	-	(-2%)	-	(-7%)
Average flow velocity (m s^{-1})	37	19	-	24	-	33	-	9	-	27	-	24
	-	(-49%)	-	-	-	-	-	-	-	-	-	-
Average deposit thickness (m)	18	19	10	10	12	10	20	18	14	13	10	9
	-	(+6%)	-	(0%)	-	(-17%)	-	(-10%)	-	(-7%)	-	(-11%)
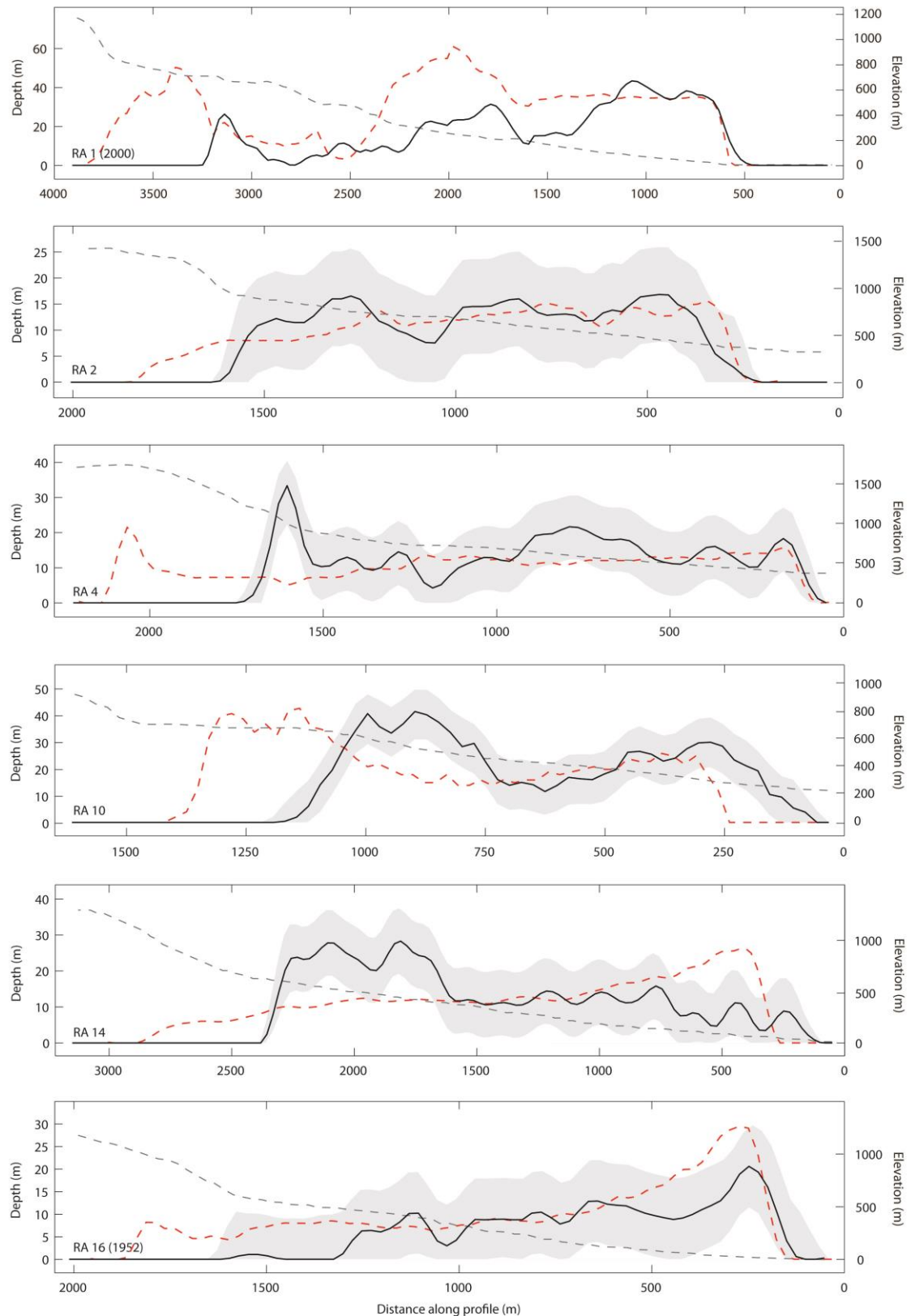
Figure 6.9) Longitudinal transects through the observed (solid black lines) and modelled deposits (dashed red lines) for the six events simulated across 3D terrain. The pale grey shading represents the overall RMS error of the GIMP DEM (Howat *et al.*, 2014). The dashed grey line represents the elevation of the path topography along the same profile. Note that, in all cases, the model simulates deposition along the full extent of the run-out path, while the observed deposit was only emplaced in the medial and distal reaches.
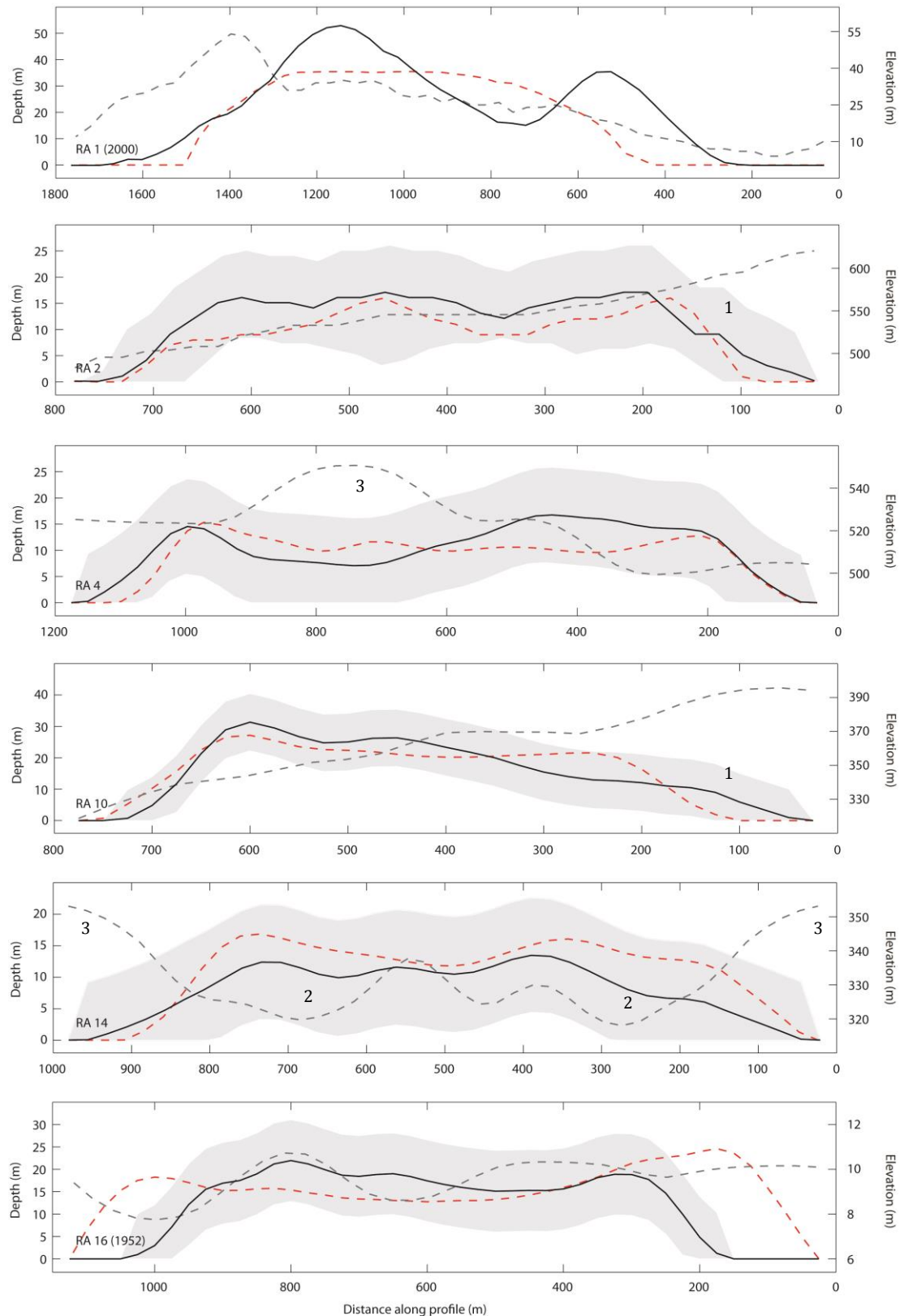
Figure 6.10) Cross-slope transects through the observed (solid black lines) and modelled deposits (dashed red lines) for the six events simulated across 3D terrain. Profiles are taken through the toe of the deposit. The pale grey shading represents the overall RMS error of the GIMP DEM (Howat *et al.*, 2014). The dashed grey line represents the elevation of the path topography along the same profile. Labels refer to evidence of upslope thinning of the observed and modelled deposits (1), hole filling (2), and pinching out of the deposits at topographic highs (3).

volumes, run-out and stalling characteristics using a single set of parameters obtained by back-analysis of the Paatuut event.

6.3.2 Application to all cases

The remaining 14 cases were modelled using contour-parallel 3D terrain in order to test the ability of the model to simulate rock avalanches at a reduced level of topographic complexity (*Section 5.2*). The ability of the model to reproduce the bulk external behaviour (i.e. run-out, *H/L*, lateral extent and surface area) of each of the 20 cases was therefore assessed using reduced major axis regression (RMA; Fig. 6.11). RMA was used instead of ordinary least squares to define a line of best fit for the relationship between the observed and modelled values, as both variables are measured with error (Clarke, 1980).

The total run-out distance of 80% of the cases was simulated within an error of ±14% using a plastic rheology and a velocity-dependent law with a single pair of input parameter values (T_0 = 250 kPa, ξ = 0.01). Half of these cases were simulated within an error of ±2%. The RMA fit to the run-out data is very close, with an r^2 value of 0.99 (Fig. 6.11a). Residuals taken from the RMA
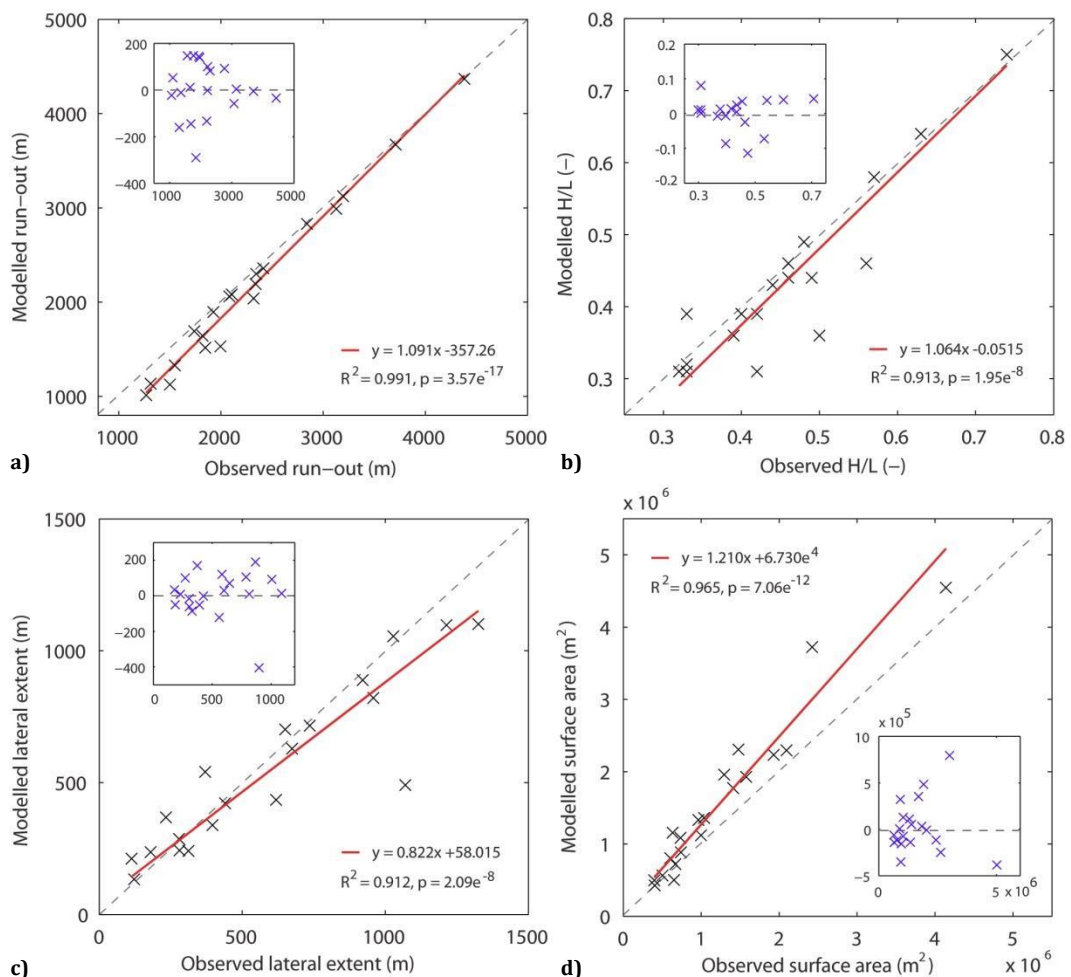
Figure 6.11) Plots of observed against modelled values of **a)** rock avalanche run-out, **b)** apparent coefficient of friction, *H/L*, **c)** lateral extent at toe, and **d)** surface area, for all 20 cases. Supporting data for all plots is found in *Appendix J*. Solid red lines are the best-fit obtained by a Reduced Major Axis Regression. Dashed grey lines show the 1:1 correlation. *P* values are based on *t* statistics. Inset: residual vs. observed plots for each model. Summary tables of the results and associated diagnostics for these regressions can be found in *Appendix K*.

fit show spreading at relatively short run-out distances (ca. 1000 – 3000 m) and clustering around residuals equal to 0 at long run-outs (>3000 m). The RMA regression fit and associated residuals shown in Fig. 6.11a therefore indicate that the model simulates events that ran out over longer distances more accurately than those that ran out over a shorter distance.

Using the rheological calibration obtained in *Section 5.1*, the *H/L* of 65% of the cases was simulated within an error of ±5%. Residuals taken from the RMA fit are well distributed, although the modelled *H/L* for three events is considerably underestimated (events 3, 6 and 15; Fig. 6.11b). These events are characterised by relatively short run-out distances (ca. 1500-2100 m) and planar slopes with a concavity index ranging from 0.91-0.95 (Table 6.1). They stall at topographic benches or on an alluvial fan below, having travelled over wet, deformable substrates (Fig. 6.1; Table 6.1).

Lateral spreading at the toe of the rock avalanches is also simulated well. The RMA regression fit to the lateral extent data achieves an r^2 value of 0.91 (Fig. 6.11c). Residuals of the regression are randomly distributed, although one large negative residual occurs where the modelled spreading (491 m) greatly underestimates the observed spreading (1,070 m). This residual corresponds to event 6, a relatively small (6×10^6 m^3) event that spread out onto a convex alluvial fan (Table 6.1). The model often fails to simulate the spreading of relatively short run-out rock avalanches at topographic benches and onto alluvial fans, thereby considerably underestimating the lateral extent of a number of deposits (events 2, 3, 5, 6, 7, and 17; Fig. 6.11c; Table 6.1). In addition, the surface area of the simulated deposits is consistently overestimated by the model (Fig. 6.11d). As discussed in *Sections 6.2* and *6.3.1*, the plastic rheology combined with a collisional stress coefficient simulates deposition along the full extent of the run-out path as opposed to only the medial and distal reaches, causing an increase in modelled surface areas.

6.4 Model sensitivity to topographic and geometric factors

The remarkable consistency in boundary conditions across the 20 rock avalanches in Vaigat provides a rare opportunity to assess the sensitivity of rock avalanche run-out to changes in key topographic and geometric factors (*Chapter 2*). The ability of the model to reproduce the bulk external behaviour of each of the 20 cases, as discussed above, is therefore explained here in terms of its sensitivity to a number of factors, including: failure volume, drop height, drop zone angle, the situation of the rock avalanche along the Vaigat Strait, and the topography of its run-out path.

6.4.1 Failure volume

As discussed in *Section 3.2.1*, events of smaller volumes tend to run out over shorter distances. The RMA regression fit and associated residuals shown in Fig. 6.11a therefore indicate that the model simulates the run-out of smaller events less accurately than that of larger events (*Section 6.3.2*). This is confirmed by the log-log plot of the normalised index of run-out against volume (Fig. 6.12a), which shows that smaller events (3×10^6-7×10^6 m^3) are characterised by a greater difference between observed and modelled run-out distances. This effect is likely to be an artefact of the model, where the constant retarding stress used in the best-fit rheology

(T_0 = 250 kPa) has a disproportionate influence on the simulated run-out of events of different magnitudes. Smaller rock avalanches are characterised by a high surface-to-volume ratio (Melosh, 1986). When modelled using the best-fit rheology (T_0 = 250 kPa, ξ = 0.01), the constant retarding stress acting at the base of the avalanche is therefore applied to a greater proportion of its total surface area. As a result, a greater proportion of the source mass remains stalled in the source area for smaller events, as shown in Fig. 6.12b, therefore causing a decrease in modelled run-out.
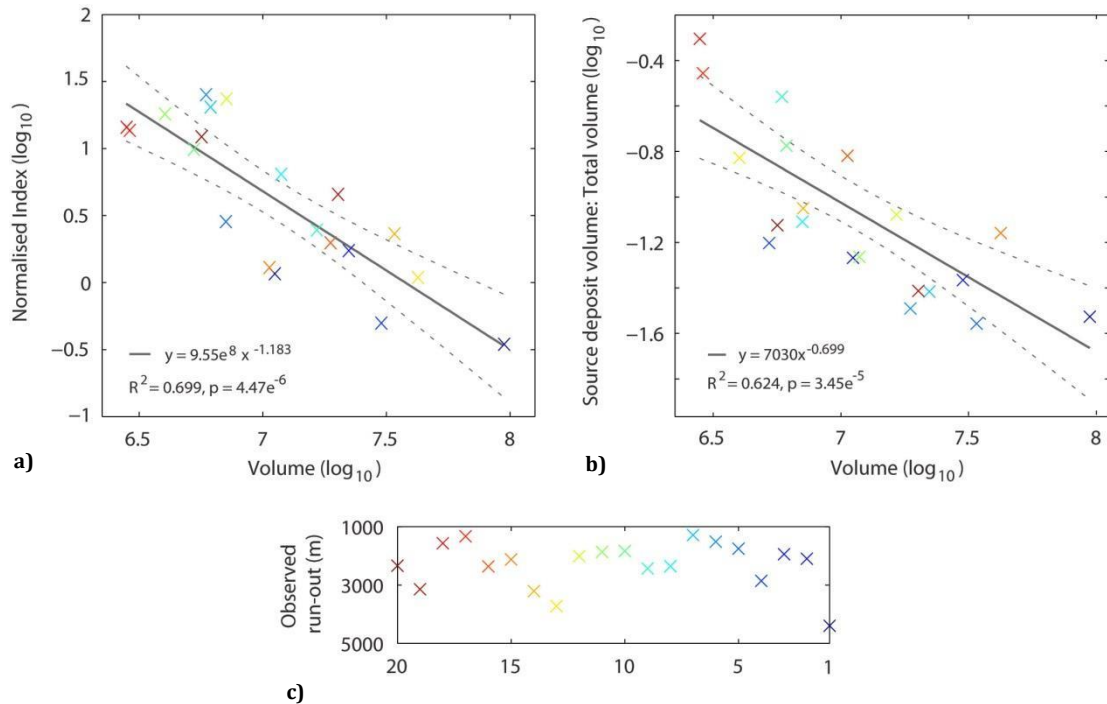
Figure 6.12) a) Plot of the normalised index of run-out (log_{10}) against volume (log_{10}), **b)** plot of the volume of material remaining stalled in the source area: total volume (log_{10}) against total volume (log_{10}). In both plots the solid grey line is the best-fit obtained by an ordinary least squares regression. Dashed lines show 95% confidence intervals. Colours are assigned according to the event; these are plotted in case order below **(c)**. Source data for the volumetric calculations are listed in *Appendix L*. Summaries of the results and associated diagnostics for these regressions are found in *Appendix K*.

6.4.2 Drop height and drop zone angle

Rock avalanches gain kinetic energy by conversion of the potential energy from their drop height (*Section 3.2.1*). In addition to failure volume, drop height therefore has an important influence on rock avalanche run-out and spreading (Straub, 1997). As discussed in the previous section, events with large failure volumes (33×10^6-94×10^6 m^3) are characterised by long run-outs (>3000 m) and a smaller difference between observed and modelled run-out distances (Fig. 6.12a). These events are also characterised by a greater drop height and steeper drop zone (Table 6.1). Plots of the normalised index of run-out versus drop height and drop zone angle show a moderate positive correlation (Fig. 6.13), indicating that the model is also likely to be sensitive to these source conditions. The strong dependence of a constant retarding stress model on the source conditions of a simulation is a difficulty that has also been noted by Kelfoun *et al.* (2005; 2009), who successfully reproduced the main features of a debris avalanche at Socompa and pyroclastic flows at Tungurahua using a constant retarding stress rheology (T_0 = 50 kPa and 5 kPa, respectively).

6.4.3 Path topography

As discussed in *Section 3.2.2.1*, the energy dissipation and subsequent run-out of rock avalanches is strongly influenced by topography, leading to a range of depositional plan forms and surface morphologies (Okura *et al.*, 2003). In most cases the model is able to simulate the mobility of the rock avalanches (as quantified by the apparent coefficient of friction, *H/L*) well, and residuals taken from the RMA fit are randomly distributed (Fig. 6.11b). However, the mobility of events 3, 6 and 15 is considerably overestimated (i.e. the modelled *H/L* underestimates the observed *H/L*; Fig. 6.14b). These events are characterised by relatively short run-out distances (ca. 1500-2100 m) and stall above topographic benches or on an alluvial fan below, having travelled over deformable and erodible substrates (Fig. 6.1; Table 6.1). In these cases, the model is not simulating the processes involved in and effects of rock avalanche emplacement across different substrates (*Section 3.3*). In reality, the energy required to mobilise the substrate may
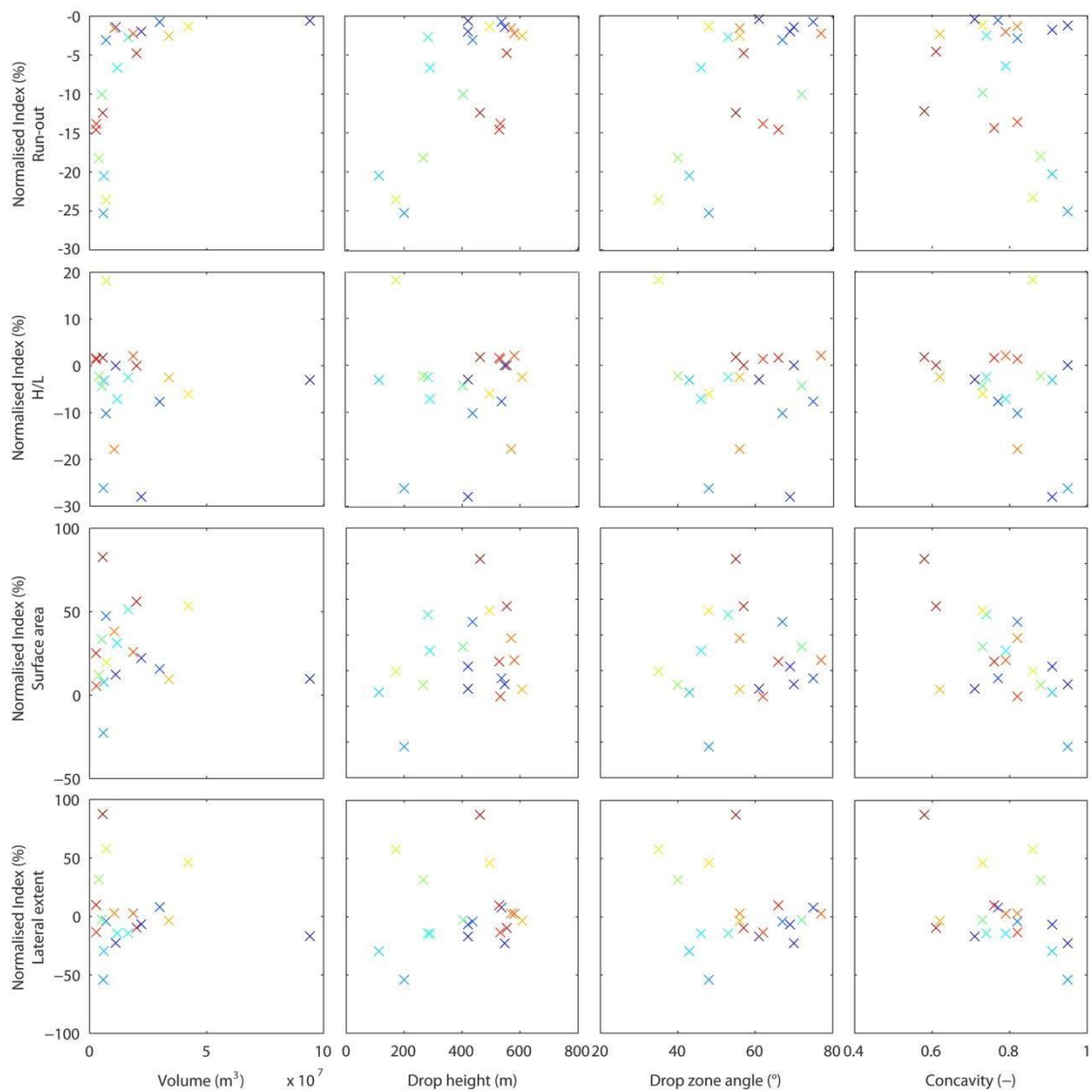
Figure 6.13) Scatter plot matrix of the normalised index, Δ, of the bulk external characteristics (run-out, apparent coefficient of friction, surface area and lateral extent) against a series of geometric characteristics (failure volume, drop height, drop zone angle and concavity). A number of relationships are apparent, particularly the influence of volume on run-out and of slope concavity on run-out, surface area and lateral extent.

have been too great and caused the avalanche mass to 'sink' into the alluvial fan or it may have been bulldozed into mounds (Dufresne *et al.*, 2010). In both cases, this would have impeded avalanche momentum/motion and caused a decrease in mobility.

The concavity of the path topography also influences the ability of the model to simulate spreading, with events emplaced across more concave surfaces (concavity index ≤0.7) tending to spread to a greater extent than observed (Fig. 6.13). For those events emplaced across fully 3D terrain, the simulated depth distributions demonstrate evidence of topographically steered flow as well as upslope thinning, hole filling and pinching out at topographic highs (Figs. 6.9 and 6.10). This suggests that the model can plausibly account for the observed morphology of a series of deposits emplaced by a range of event types and is sensitive to the local topography.
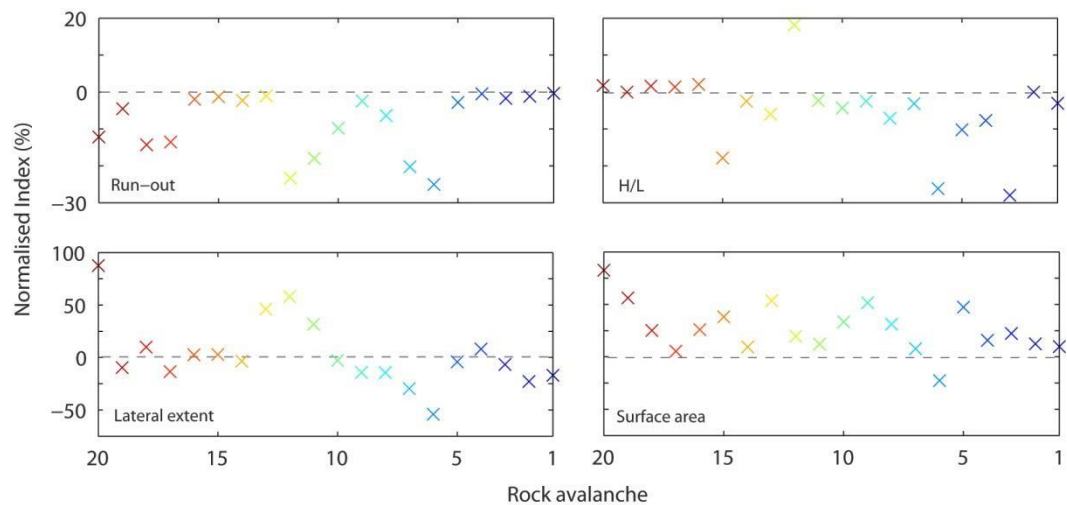
Figure 6.14) Case order plots of the normalised index of **a)** rock avalanche run-out, **b)** apparent coefficient of friction, *H/L*, **c)** lateral extent at toe, and **d)** surface area, for all 20 cases. The events are ordered 1-20, E-W across the site. Supporting data may be found in *Appendix J*.

Difficulties are encountered when simulating the spreading of relatively short run-out events at topographic benches and onto alluvial fans, where the model considerably underestimates the lateral extent of a number of deposits (events 2, 3, 5, 6, 7, and 17; Fig. 6.14c). Conversely, lateral spreading is overestimated where, in reality, the flow has been laterally confined somewhere along its run-out path (events 11, 12 and 20). In these cases the rock avalanches were simulated across contour-parallel 3D terrain, which does not impose the 3D confinement effects of topography on the rock avalanche. This is also the case when considering areas of deposition, which are most poorly simulated when the event in question was emplaced across contour-parallel 3D terrain and for events that were partially confined, such as events 19 and 20 (Δ = +56% and +83%, respectively; Fig. 6.14d; Table 6.3). These results attest to the importance of using realistic terrain models, as the dissipation of mechanical energy from the rock avalanche, and thereby its mobility and spreading behaviour, is more accurately simulated (*Section 3.2.2.1*; Nicoletti and Sorriso-Valvo, 1991; McDougall and Hungr, 2004).

6.5 Summary

Despite being widely used to simulate the propagation of rock avalanches, models

assuming either a constant dynamic friction or a Voellmy rheology fail to reproduce the observed event characteristics and deposit distribution at Paatuut (e.g. McEwan and Malin, 1989; Evans *et al.*, 2001; Crosta *et al.*, 2004; Sheridan *et al.*, 2005; Pirulli, 2009; Kelfoun, 2011; Sosio *et al.*, 2012; see *Section 6.2*). Although these models can account crudely for the observed run-out, the basal friction angles necessary to generate this run-out result in a long duration of simulated failure with deposition concentrated in the proximal reaches of the run-out path. The best-fit simulation of the Paatuut event instead assumes a plastic rheology with a velocity-dependent law (T_0 = 250 kPa, ξ = 0.01). This simulates the run-out of the rock avalanche to within ±0.3% of the observed run-out, which is well within the margin of measurement error (±2%; Table 5.2, p 42). This rheology is therefore successful in reproducing the event kinematics, deposit mass distribution and morphology to justify the assumption that it constitutes a first order representation of the dominant features of the emplacement dynamics.

19 other events are simulated using the best-fit rheological calibration obtained by back-analysis of the Paatuut event (*Section 6.3*). For those simulated across fully 3D terrain, the model is able to replicate the morphology and distribution of mass in the resultant deposits very well (*Section 6.3.1*). Depositional features observed in the observed and modelled deposits developed in response to the underlying topography, suggesting that the model can plausibly account for the observed morphology of a series of deposits emplaced by a range of event types. The bulk external characteristics of the 20 cases are simulated with varying degrees of success. The run-out of 80% of the cases was simulated within an error of ±14%.

The performance of the model is sensitive to a range of topographic and geometric factors (*Section 6.4*). In particular, difficulties in correctly simulating the observed run-out and other bulk external characteristics of the rock avalanches are encountered when:

1) The failure volume of the simulated event is small, as the constant retarding stress acting at the base of the avalanche is applied to a greater proportion of its total surface area. This means that a greater proportion of the source mass remains stalled in the source area and therefore that the rock avalanche is simulated to run out over a shorter distance.

2) The event in question is emplaced across contour-parallel terrain, which cannot fully account for longitudinal and transverse confinement of the rock avalanche mass or topographic junctions that act to block, confine or diverge flow.

3) The rock avalanche encounters a change in substrate along its run-out path and the model is unable to simulate the associated changes in avalanche mobility.

These exercises show encouraging results in the ability of the model to simulate a series of events using a single set of parameters obtained by back-analysis of the Paatuut event alone. The results demonstrate that a plastic rheology with a velocity-dependent law describes the emplacement of these events and the resultant deposit more accurately than any other simple rheological law. The implications of this for our process understanding and the subsequent modelling of such events will be discussed in *Chapter 7*.

Chapter 7

Discussion

As discussed in *Chapter 4*, accurately simulating the emplacement dynamics of rock avalanches is complicated by the anisotropic nature of the materials involved, as well as the complex interactions that occur during their propagation across steep and irregular terrain (Manzella and Labiouse, 2013). Depth-averaging in continuum dynamic models such as *VolcFlow* (Kelfoun and Druitt, 2005) assumes that the rheology of the flow can be represented as a single term that expresses the frictional forces interacting between the flow and basal path (*Section 4.2*; Luna *et al.*, 2013). However, the common lack of pre-, syn- and post-failure observations of rock avalanches has meant that the majority of numerical modelling studies have focussed on replicating the dynamics of a single, well-constrained event, and fail to consider the wider utility and sensitivity of the rheological calibration obtained. A series of 20 large rock avalanche deposits in Vaigat, West Greenland, has presented the unique opportunity to undertake a case-specific calibration and investigate the validity of applying the same parameters to other events emplaced in similar conditions (*Chapter 5*). The results presented in *Chapter 6* are now discussed with regards to the use of simple rheological laws in numerical run-out models (*Section 7.1*) and their implications for model requirements (*Section 7.2*). The implications of these results for forward modelling and for the incorporation of numerical run-out models into a risk assessment framework is then discussed (*Sections 7.3* and *7.4*), placing particular emphasis on their implications for tsunami hazard and risk assessments (*Section 7.5*).

7.1 The suitability of simple rheological laws for simulating rock avalanches and implications for understanding their behaviour

Despite being widely used to simulate the propagation of rock avalanches, models assuming either a constant dynamic friction or a Voellmy rheology failed to reproduce geometric and dynamic observations at Paatuut (e.g. McEwan and Malin, 1989; Evans *et al.*, 2001; Crosta *et al.*, 2004; Sheridan *et al.*, 2005; Pirulli, 2009; Kelfoun, 2011; Sosio *et al.*, 2012; see *Section 6.2*). While both of the Coulomb frictional models and the Voellmy model are able to crudely account for the observed run-out at Paatuut, the basal friction angles necessary to generate this run-out result in a long duration of simulated failure with deposition concentrated in the proximal reaches of the run-out path. This is at odds with the morphology of the observed deposit and the kinematic constraints of the event that were estimated from seismic records (*Section 2.2.2*). Instead, the main features of the Paatuut event can be reproduced using a plastic rheology with a velocity-dependent law, as shown in *Section 6.2.5* (T_0 = 250 kPa, ξ = 0.01). A number of studies have successfully used *VolcFlow* to simulate the run-out and emplacement dynamics of debris avalanches and pyroclastic flows assuming a plastic rheology (Table 7.1). The limited ability of frictional models to simulate the run-

Table 7.1) Examples of long run-out events successfully modelled assuming using a plastic rheology. Only calibration results obtained using *VolcFlow* are considered, as different dynamic models incorporate different internal stress assumptions. ***** Exact value of the best-fit constant retarding stress is dependent upon whether single or retrogressive failure of the rock mass was defined. ****** Event collapsed into water. Exact value of the best-fit constant retarding stress is dependent upon the value of the stress exerted by the water as defined in *VolcFlow*.

Event	Notes	Volume (m³)	Run-out (m)	Parameters (T_0, ξ)	Reference
Fogo, Cape Verde	Debris avalanche	115x10⁹	40,000	90-95 kPa*	Paris *et al.* (2011)
Socompa, Chile	Debris avalanche	25x10⁹	40,000	52 kPa	Kelfoun and Druitt (2005)
Güìmar, Tenerife	Debris avalanche	44x10⁹	38,000	145-150 kPa*	Giachetti *et al.* (2011)
Réunion Island	Debris avalanche	10x10⁹	35-40,000	20-50 kPa**	Kelfoun *et al.* (2010)
Tungurahua, Ecuador	Pyroclastic flows	20x10⁶	8,000	5 kPa	Kelfoun *et al.* (2009)
Merapi, Indonesia	Block-and-ash flows	6x10⁶	7,000	3.5 kPa, 0.01	Charbonnier and Gertisser (2012)
Paatuut, Greenland	Rock avalanche	94x10⁶	4,400	250 kPa, 0.01	This study

out of the events in Vaigat as well as the volcanic debris avalanches listed in Table 7.1 suggests that processes additional to those of granular flow dynamic are involved, such as dynamic fragmentation (*Section 3.2.2.2*). Unlike rock avalanches, the material derived from the edifices that source volcanic debris avalanches is normally-consolidated, often hydrothermally altered and therefore substantially weakened (Davies *et al.*, 2011). This reduces the intact rock strength and therefore the frictional resistance of a fragmenting rock layer at the base of the flow (Davies *et al.*, 2011), generating run-outs that are 2-3 orders of magnitude longer than non-volcanic events of the same volume (Siebert, 1984). The high constant retarding stress required to correctly simulate the event at Paatuut remains difficult to physically explain (Table 7.1), although it may reflect differences in the intact rock strength of the materials involved or in the physical processes operating within the flowing mass (Kelfoun *et al.*, 2009). Alternatively, a high constant retarding stress may be required to realistically simulate events where the failure and subsequent run-out of large volumes of material down steep slopes occurred over a relatively short period of time (Takahashi and Tsujimoto, 2000; Charbonnier and Gertisser, 2012), as in fjords and semi-enclosed basins. It is important to note that the reasons for this behaviour are speculative, and further work using a plastic rheology to simulate rock avalanches in other settings should be undertaken for comparison.

The major implication of using a plastic rheology is that flow mobility is driven by a constant stress condition and not by a constant slope condition, as in the frictional models described in *Section 3.2.1*. This means that the friction angle at the base of these mass movements cannot be considered constant, as in frictional models. Instead, the ratio of driving to retarding stresses decreases as flow thickness increases, leading to very mobile and deep flows (Charbonnier and Gertisser, 2012). Although this appears to be in keeping with a number of field observations, it is difficult to explain from a mechanical point of view as it stipulates that the shear stress at the base of the flow is independent of its thickness and/or its velocity (*Section 4.2*; Dade and Huppert, 1998). Rock avalanches exhibit complex time-dependent and spatially variable mechanical behaviour, which continuum dynamic numerical models often simplify into one- or two-parameter

rheological laws (*Section 4.2*; Iverson and Vallance, 2001). The constant stress condition invoked when using a plastic rheology is most likely to represent an average value of a retarding stress at the flow base that varies with time during rock avalanche run-out (Kelfoun, 2005). To explain this behaviour mechanically, a constant stress at the base of the flow can be obtained if the basal friction angle (φ_{bed}) decreases with increasing flow depth (h), assuming that the stress of the flow is defined by Coulomb friction (Mangeney *et al*., 2007). For example, the basal friction angle may increase more rapidly in thin flows relative to thick flows due to the presence of resistant blocks within the fluidised matrix, which act to increase the solid interaction with the ground as the flow thins (Kelfoun, 2011). Alternatively, an increase of the mechanical strength of the flows from their base or interior to the surface could also explain the apparent inverse relationship between flow depth and friction. This strength may vary in relation to the granulometry of the flows: for example, most deposits are composed of a fluidal interior of matrix-supported debris covered by a rafted and brittle crust of angular boulders (*Section 3.4.1*; e.g. Tsergo Ri, Nepal: Heuberger *et al*., 1984; Köfels, Austria: Brückl *et al*., 2001; Flims, Switzerland: von Poschinger *et al*., 2006; Val Pola, Italy; Crosta *et al*., 2007). In deeper rock avalanches, a greater proportion of the flow would therefore be constituted of fine particles, prolonging flow capability (Fig. 7.1).
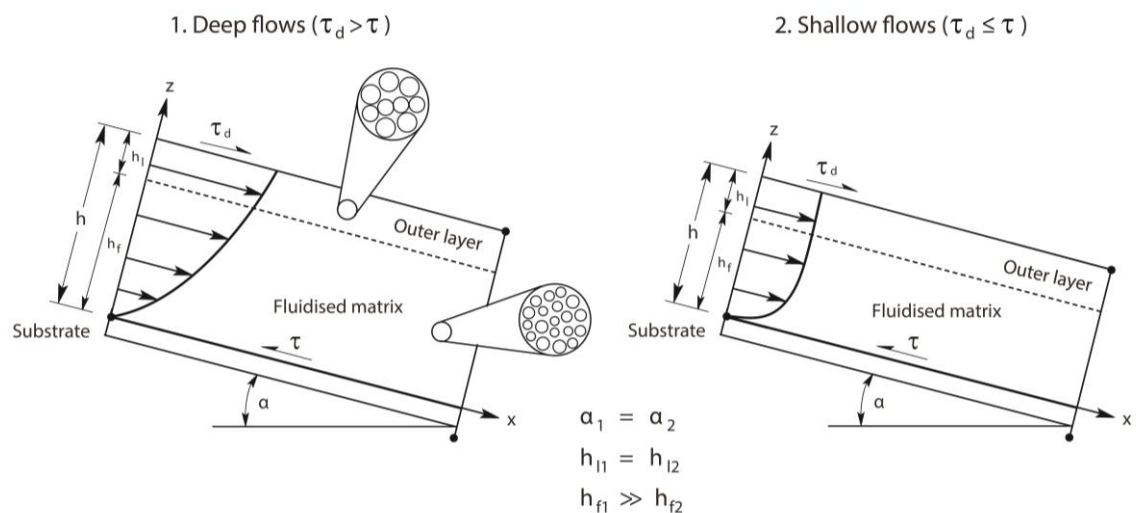
Figure 7.1) Schematic diagram of the system described above. Here, rock avalanches are composed of a fluid-like interior of matrix-supported debris (depth = h_f) surrounded by a more resistant outer layer (depth = h_l). In deep flows (1), the low-friction interior in contact with the ground would permit flow even on gentle slopes (small α), with the more frictional outer layer simply being rafted. This would act to prolong flow capability. In shallower flows (2), the influence of the resistant outer layer would increase, reducing the driving stress of the flow (τ_d). Diagrams adapted from Louge's (2003) schematic of steady, fully developed flows down an inclined plane.

Although a plastic rheology fits the morphology of many rock avalanche deposits better than a frictional rheology, the reasons for its success remain unclear. The plastic-type rheology that was used in this research should therefore only be considered as a first order description of the rheology of the rock avalanches in Vaigat. This poses fundamental questions regarding the use of simple one- or two-parameter rheological laws for simulating rock avalanches. Although these laws are straightforward to implement, their use is contentious as the parameters governing the rheology of the flows often lack any physical meaning and remain difficult to physically quantify or

verify, despite a number of attempts (e.g. Schneider *et al.*, 2010; Fischer *et al.*, 2012b). In addition, the use of single-phase mass and momentum balance equations to govern flow mobility, such as those used in the one fluid version of *VolcFlow* (see *Section 4.3.1*), only passively incorporates the effects of mechanical lubrication and fluidisation of the flow. The large uncertainty associated with parameter selection for these models demands the development of more sophisticated models that use physically measurable and dynamically variable values of these parameters, which can actively take into account the presence of materials with different physical and rheological properties (e.g. rock, ice, snow, slurry, water and fine particles) and shifts between different flow regimes (Pudasaini, 2012). This property is particularly important when considering the melting of snow and/or ice due to frictional heating during rock avalanche propagation, which is likely to have occurred during the Paatuut event (AD 2000) and in a number of other cases at Vaigat (*Section 2.2.1*). The development of a new rheological model by Pudasaini and Krautblatter (*In Press*) marks the first attempt to address some of these issues. Rather than treating the effective internal and basal friction angles as constant, the model includes interphase mass and momentum exchanges that correspond to spatial and temporal variations in the effective solid volume fraction, volume fraction of ice, friction coefficients, and lubrication/fluidisation factors that are a function of a number of physical parameters or mechanical variables (e.g. volume fractions, shear-rate and normal stresses). The development of such models, which are capable of performing dynamic strength weakening due to the effects of internal fluidisation and/or basal lubrication, represent an important direction for future research, and detailed quantitative evaluation of their performance with laboratory and field observations is required.

7.2 Requirements for numerical run-out modelling

As shown in *Section 6.3*, the rheological calibration obtained by back-analysis of the Paatuut event can plausibly account for the observed morphology of a series of deposits emplaced by events of different types, although its performance is sensitive to a range of topographic and geometric factors (*Section 6.4*). This has important implications for model requirements when simulating either a single event or multiple events.

The flow capacity of rock avalanches modelled using a plastic rheology is directly related to their depth, meaning that numerical simulations of their emplacement dynamics have a particularly strong dependence on the source conditions and path topography (Kelfoun *et al.*, 2009). As discussed in *Section 6.4.1*, the constant retarding stress at the base of the avalanche has a disproportionate influence on the simulated run-out of events of different magnitudes, with a greater proportion of the source mass remaining stalled in the source area for smaller events (Melosh, 1986). This is indicative of a threshold volume below which rock avalanches in Vaigat, and perhaps other settings, cannot be modelled satisfactorily using a plastic rheology. Further calibration studies are therefore required to test this and to assess the extent to which this condition varies in different settings. In addition, as numerical models of rock avalanche run-out are highly sensitive to the initial collapse volume, accurately quantifying this volume is important for successful backward and forward analyses (Kelfoun, 2009). In *Chapter 5*, the failure volumes of the rock avalanches in Vaigat were estimated using the measured present-day volume of the

corresponding deposit, as no pre-event DEMs were available. The deposit volumes were calculated using a self-similar volume-area scaling (Equation 5.2) that has been successfully applied for bedrock landslides in a number of settings (after: Hovius *et al.*, 1997; Malamud *et al.*, 2004). This captures the central tendency in the scaling exponent for datasets consisting of such events, although the associated errors are large and it remains difficult to resolve how broadly this scaling can be applied (Larsen *et al.*, 2010). However, the scaling exponents derived from measurements of scar versus deposit geometry for global bedrock landslides and rock avalanches are indistinguishable (Larsen *et al.*, 2010). This means that the tendency for rock avalanches to increase in volume due to fragmentation, dilation and entrainment has not introduced significant errors into this scaling relationship and advocates its use for obtaining a first-order estimate of rock avalanche volume (Hungr and Evans, 2004).

The availability of pre- and post-event DEMs, and at a resolution that is reasonable in relation to rock avalanche size, is essential for the success of retroactive simulations such as those run in *Chapter 5* (Schneider *et al.*, 2010). It is well known that the ability of a model to account for the energy losses caused during run-out over complex topography is, in part, conditioned by the resolution of the DEM used (Hungr and McDougall, 2009). However, at present it is unclear as to what extent the observed/modelled errors discussed in *Section 6.3.2* scale with changes in grid resolution. The results shown in *Chapter 6* demonstrate that a 25 m grid resolution is suitable for reproducing the dominant features of rock avalanche emplacement in Vaigat, although the ability of the model to replicate the small-scale structures that characterise the surfaces of these deposits, such as pressure ridges and hummocks, is compromised. These structures are believed to reflect processes active during the flow and are therefore important for inferring aspects of flow dynamics (Dufresne and Davies, 2009). However, few numerical modelling studies have focussed on replicating these structures (Pudasaini and Hutter, 2007). This is due, in part, to the poor quality of topographic data in areas of steep terrain, where many techniques for DEM generation suffer from the occlusion of features due to layover and shadowing (Raggam, 2006). Recent advances in the use (and combination) of LiDAR techniques and tri-stereoscopy, which acquires stereo triplets in the forward, backward and nadir view of an area, are beginning to overcome this problem (e.g. Giribabu *et al.*, 2013; Basgall *et al.*, 2014; Poli *et al.*, *In Press*). Future numerical modelling efforts should therefore consider making use of newly available high-resolution (2 m) DEMs for the purpose of more accurately mapping and quantifying the morphological signature of rock avalanches in Vaigat (Fig. 7.2), and indeed in other areas. These models can also be extended to show 2D surface strain during emplacement, which allows for the deformation histories of chosen points on the rock avalanche surface to be tracked (Kelfoun *et al.*, 2008). This will help to more correctly validate model outputs and perhaps shed light on dynamic flow processes occurring at a smaller scale within the rock avalanche mass.

As discussed in *Section 3.3*, the interaction with and subsequent entrainment of run-out path materials can exert a significant influence on rock avalanche dynamics and run-out behaviour. However, uncertainty in these processes is large (Dufresne, 2009). In *Chapter 5*, each simulation treated the rock avalanche as a homogenous, incompressible continuum and did not explicitly account for basal erosion and/or entrainment, pore fluid pressure, density variations due to
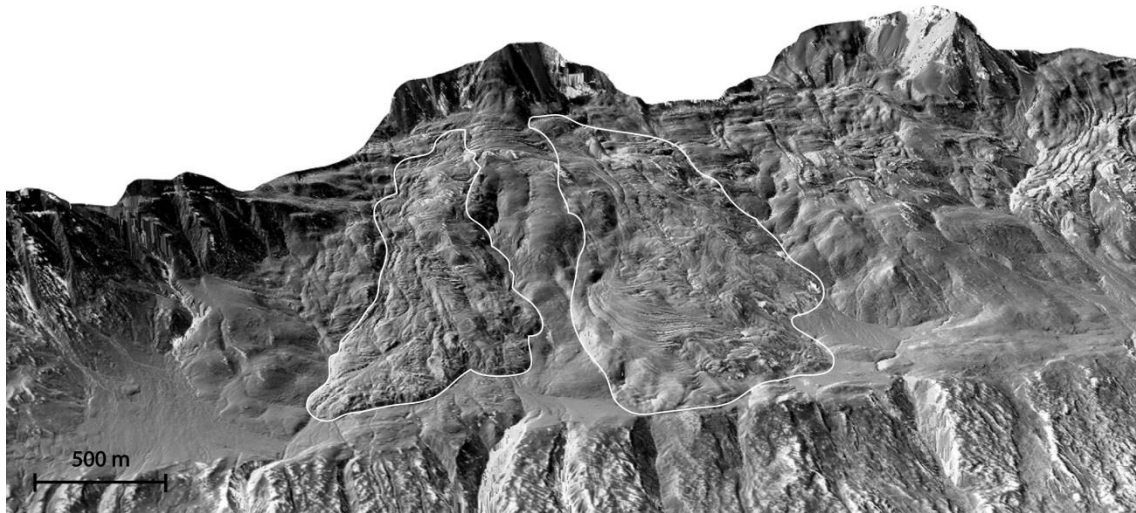
Figure 7.2) 3D perspective view of rock avalanche deposits in Vaigat, West Greenland, looking north from a position above the Vaigat Strait. 0.5 m satellite imagery was acquired on 19 June 2012 by WorldView-1 and orthorectified to produce a 2 m DEM. All data provided by Ben Smith (Polar Science Center).

material dilation or incorporation of air, ice or water (Pirulli and Mangeney, 2008). The model was therefore unable to simulate the associated changes in mobility and run-out if the rock avalanche had encountered a change in substrate along its run-out path (*Section 6.4.3*), demonstrating the importance of incorporating these changes into numerical simulations (Cuomo *et al.*, 2014). Although these simulations would benefit from incorporating erosion and entrainment laws, the specific processes acting at the base of rock avalanches during travel over (non-)deformable and erodible substrates remain poorly understood and therefore difficult to model (*Section 3.3*). In addition, the rates of these processes are difficult to constrain, with the published literature lacking estimates of field-derived rock avalanche-induced erosion rates (Iverson, 2012; McCoy *et al.*, 2012). Commonly, erosion laws predict that the volume growth of rock avalanches resulting from entrainment processes can be described either by an exponential law (Pirulli and Pastor, 2012), or by a monotonic increase in the amount of eroded material when the basal shear stress exceeds a given threshold (Pitman *et al.*, 2003). Accurate incorporation of these laws into numerical models remains difficult, although recent developments have been made using *VolcFlow* to model pyroclastic density current erosion and bulking processes (e.g. Bernard *et al.*, 2014) and should be pursued in future work.

Successful model calibration is not only reliant upon reproducing the correct run-out distance, but must simultaneously fit with geometric, energetic, and dynamic observations (Schneider *et al.*, 2010). As discussed in *Chapter 4*, the overall level of fit of the model to these observations gives an indication of how well the model demonstrates process representation. For large rock avalanches such as Paatuut, long-period seismic recordings are often the only data available for characterising avalanche dynamics (Suriñach *et al.*, 2005). In addition to the single point predictions used for dynamic constraints in *Chapter 5* (e.g. average and maximum velocity), inverse modelling of teleseismic data can be used in conjunction with geometric constraints from aerial/satellite imagery to determine rock avalanche force histories, yielding estimates of their duration, momenta, potential energy loss, mass, and run-out trajectory (Ekström and Stark, 2013).

This technique generally requires rock-slope failure and subsequent run-out on slopes steep enough to generate accelerations of approximately 1 m s^{-2} or greater. When considering the terrain and height drop of the rock avalanche at Paatuut, this is likely to have been the case (*Chapter 2*). Assuming a density of ca. 2850 kg m^{-3} for basalt (Suckro *et al*., 2013) and a failure volume of ca. 94x10^6 m^3, an approximate value for the long-period surface-wave magnitude (M_{sw}) of the Paatuut event can be estimated from the failure mass (m; in 10^{12} kg) alone:

$$M_{sw} = \frac{12 + log_{10}\left(\frac{m}{0.54}\right)}{2.2} \qquad \text{[Eq. 7.1]}$$

The peak force involved in the event would have been ca. 0.2x10^{12} N, generating an estimated surface-wave magnitude of $M_{sw} \approx 5.3$ (Stark, 2014; *pers. comm.*). This places the Paatuut event within the range of a typical analysis (Ekström and Stark, 2013). However, as much of the mass remained stalled on the plateau at ca. 800-900 m above sea level, the duration over which the peak accelerations and forces were generated may have been too short for detection and teleseismic inversion. Nevertheless, such techniques may help to better constrain the numerical models used here and they raise a number of important questions, including: what is the minimum magnitude of rock avalanche event that can be reliably detected by teleseismic source inversion?; Are there particular settings or dynamic factors that preclude the use of this technique for determining force histories?; and, how reliably can this technique distinguish between discrete geomorphic events, or pulses within single events? With the potential for the global seismic network to be used as a means of detecting the occurrence of rock avalanches in real time (Burtin *et al*., 2013), this technique represents an important avenue for further research.

7.3 Implications for forward modelling

Physically based simulations of rock avalanches using *VolcFlow* provide a useful tool for recognising flow patterns and for calculating potential flow magnitudes, velocities, and fluxes (Crosta *et al*., 2006b). The calibration discussed in *Chapter 6* shows encouraging results in the model's ability to simulate a series of events using a single set of parameters obtained by back-analysis of the Paatuut event alone, suggesting that first-order run-out prediction is possible. However, it is important to recognise that the calibration results for these events may not be transferrable between other dynamic models, which incorporate different internal stress assumptions (*Section 4.1.2*; Hungr, 2007). As discussed in *Section 7.1*, it is also important to question how definitive this calibration is, as particular aspects of the boundary conditions in Vaigat remain unknown (e.g. free surface drag, lubrication, fluidisation, basal scouring and entrainment and/or deposition during motion, water absorption, material mixing, liquefaction, substrate conditions). When considering the model requirements discussed in *Section 7.2* it is clear that, prior to the application of this model for predictive purposes, in-depth studies are required in order to consider the effects of these conditions and the relative importance of key factors on simulated run-out. Once these conditions are satisfied, a robust framework must be developed for the incorporation of the model into hazard and risk assessments.

7.4 Incorporation of numerical run-out models into a risk assessment framework

As discussed in *Chapter 4*, quantitative risk assessments of the future hazards posed by potential rock avalanches rely upon numerical modelling for the successful prediction of the extent and character of their motion (Evans *et al.*, 2001). Building on the discussion in *Section 7.3*, it is clear that the application of a model for predictive purposes, and its subsequent incorporation into risk assessments, requires the development of a suitable framework. In addition to the model requirements outlined in *Section 7.2*, this framework should include (i) estimation of the failure volume of the unstable rock-slope in question, (ii) probabilistic run-out assessments using numerical run-out modelling, and (iii) quantification of the vulnerability of elements at risk. While detailed consideration of (iii) is beyond the scope of this thesis, the development of a robust approach for both (i) and (ii) is pertinent for future modelling efforts and so is discussed in further detail here.

Geometric and kinematic models of the motion of a rockslide can be identified and its potential failure volume quantified using differential satellite interferometric synthetic aperture radar (InSAR), as has been demonstrated in Norway (e.g. Lauknes *et al.*, 2010; Blikra and Christiansen, 2014; Harbitz *et al.*, 2014). However, the use of differential InSAR to estimate the potential failure volume of a rock-slope requires it to be actively deforming. Where this method is not applicable, a number of authors have proposed that failure surfaces in rock-slopes are controlled by their slope geometry, implying the existence of a potential sliding surface above which the rock mass is assumed to be potentially unstable due to the absence of buttresses (e.g. Jaboyedoff *et al.*, 2009). This failure surface has been termed the isobase by Golts and Rosenthal (1993) and the Sloping Local Base Level (SLBL) by Jaboyedoff *et al.* (2004). Ideally, the SLBL should be constrained by geophysical, geotechnical and/or geomorphic data derived using methods such as seismic profiling and boreholes (Travelletti *et al.*, 2010). This approach can be highly efficient for integrating and upscaling interpretations of any local multi-source data for the estimation of potential failure surfaces (Jaboyedoff *et al.*, 2013). An estimate of the potential failure volume of an unstable rock-slope could therefore be obtained by differencing the elevation of this surface and that of the present-day topography. The sliding surface and corresponding failure volume could then be used to constrain the source conditions of a potential future event for input into numerical models of rock avalanche run-out. However, it should be noted that, in reality, the limits of stability are unlikely to be reached everywhere simultaneously and it is therefore unlikely that a future failure would develop as a single event, as predicted by the SLBL, and may instead proceed retrogressively (Jaboyedoff *et al.*, 2009). This is particularly important for any numerical modelling efforts that aim to use the SLBL as a means of estimating the potential failure volume of an unstable rock-slope, given the strong dependence of simulated dynamics on source conditions such as failure volume and mode (*Section 7.2*).

Although continuum dynamic models are deterministic, they can incorporate probabilistic components by adopting a range of plausible parameter values associated with different probable conditions (e.g. material properties and source conditions) in order to compute a corresponding range in possible outcomes (Iverson, 2014). To date, the majority of studies concerned with run-out

prediction have been limited to manual parametric model runs (see *Section 4.1.2.1*). Classical methods of sampling input parameter values, such as Monte Carlo and Latin Hypercube sampling, can also be used, although these approaches tend to be computationally intensive for continuum dynamic models that are based on the solution of conservation laws, such as *VolcFlow* (McDougall *et al.*, 2012). A number of more recently developed alternatives exist, including non-sampling methods such as stochastic collocation, polynomial chaos quadrature and spectral projection (see Dalbey, 2009 for a review). These methods are encouraging in their ability to produce high quality results while preserving the simplicity and robustness of Monte Carlo-type approaches in both simple settings and also when trialled using TITAN2D to simulate the 1991 block-and-ash flows at Colima Volcano, Mexico (Dalbey *et al.*, 2008).

Once a prospective failure is identified, hazard maps can be constructed for risk management practices by forward-modelling the event using a range of parameter values (Corominas *et al.*, 2014). The calibration exercises undertaken in *Chapter 5* have shown that a series of events that occurred within similar boundary conditions can be accurately simulated using a single set of rheological parameters. The parameter values required for scenario modelling in other settings could therefore, within theory, be derived from the back-analysis of any other event provided that it occurred within similar boundary conditions (McKinnon, 2010). To fully test this theory requires a database of back-analyses, as well as the corresponding rheological parameters, undertaken in different environments. If groups of events are similar in their simulated dynamics and behaviour this could indicate that they share some aspects of the underlying processes that govern excess mobility. These cases could then be used to differentiate between theories of rock avalanche dynamics such as those presented in *Section 3.2.2*. While empirical run-out models are commonly used in probabilistic risk assessments, further testing and refinement is required for dynamic models that are used in this manner; this will lead to improvements in their predictive ability and a more widespread use in practical applications (Iverson, 2014).

7.5 Tsunami hazard and risk assessments

As discussed in *Section 1.3*, the consequences of rock avalanches can often be more far-reaching and severe than the events themselves, with far-field hazards such as rock avalanche-induced tsunami posing a much more extensive risk. The findings presented in *Chapter 6* indicate that there is a need for further calibration studies using *VolcFlow* to simulate rock avalanches in other fjords and semi-enclosed basins. Rock avalanches that collapse into narrow fjords or confined bays commonly do so onto steep slopes and require targeted calibration initiatives that may involve unusual parameter sets (see *Section 7.1*). These initiatives should aim to establish whether a plastic rheology with a high constant retarding stress is characteristic of rock avalanche events in steep fjordlands such as Alaska (Miller, 1960), British Columbia (Bornhold *et al.*, 2007), Chile (Sepúlveda and Serey, 2009), Norway (Olesen *et al.*, 2004) and New Zealand (Dykstra, 2013). Being able to accurately simulate the distal reaches of rock avalanches is particularly important in these settings where the momentum of the rock avalanche at the point of entry into the water strongly controls the magnitude of the resultant displacement wave. However, parameters such as the velocity, volume and flux of material into the water are often poorly constrained, and the extent to which the

bathymetry and coastal morphology condition the propagation of tsunami waves and the resultant coastal inundation varies considerably between different locations (Harbitz *et al.*, 2014). The development and expansion of these datasets would therefore provide an important foundation for future model evaluation and scenario simulations in fjord environments, as a two fluids version of *VolcFlow* has the unique capability of being able to simulate combined subaerial-submerged events (Kelfoun *et al.*, 2010).

A number of recent events, including the rock avalanche at Paatuut, have emphasised our lack of understanding with regards to the magnitude and frequency of catastrophic rock-slope failures above flooded fjords and semi-enclosed basins, especially in tectonically quiescent terrain (Korup and Dunning, *In Press*). In general, the lack of pre-, syn- and post-failure observations of rock avalanches makes it difficult to distinguish between catastrophic inputs of sediment and background rates of erosion and sediment transport (Hewitt *et al.*, 2008). While a number of notable submarine failures have been investigated (e.g. Løvholt *et al.*, 2008; Tappin *et al.*, 2008; Völker *et al.*, 2010), investigations of subaerial rock avalanches that impact a water body and trigger further submarine landsliding, soft sediment deformation and tsunami waves are rare, as detailed (and seamless) topographic and bathymetric datasets are often unavailable (Hermanns *et al.*, 2014). A future challenge will therefore be to compile a consistent, high quality database of submarine deposits by using techniques such as seismic profiling to locate submarine geomorphic and sedimentary archives of past tsunamigenic events. In addition to the use of submarine archives, further work must also be undertaken in order to capture and characterise evidence for the impact of rock avalanche-induced tsunami across key coastal features. Field evidence of the rock avalanche and corresponding tsunami at Paatuut (AD 2000) remains well preserved (Pedersen *et al.*, 2002; Dahl-Jensen *et al.*, 2004). In future work, mapping of the onshore and offshore deposits using high-resolution hyperspectral and topographic data will provide the opportunity to develop combined spectral and morphological constraints that could be used to identify remnant tsunami deposits from other rock avalanches in the area. This work could then be extended by using the two fluids version of *VolcFlow* in order to back-analyse and examine the tsunamigenic potential of other rock avalanches in the Vaigat Strait.

When considering rock avalanche-triggered tsunami, multiple sources of hazard must be analysed in parallel and finally integrated into a multi-hazard, multi-risk analysis (van Westen, 2005). Although the consequences of cascading sequences are well known, there remains no well-established and widely accepted methodology for the identification and quantitative assessment of multi-hazard events (Corominas *et al.*, 2014). These assessments must consider a number of issues, including:

1. The integration of different hazard models into one system;
2. The phenomenon of hazard cascades, whereby hazards are related and influence each other;
3. Ways of calculating losses for different hazard and asset combinations; and
4. Finding a common framework for multi-risk analyses that involves different hazards, methodologies, disciplines and terminologies.

At present, there exist few projects worldwide that consider the risk assessment and management

of tsunamigenic rock avalanches in mountainous areas with fjords, lakes or reservoirs, and those that do are largely concentrated in the Norwegian fjords (Blikra *et al.*, 2005; Eidsvig *et al.*, 2011; Harbitz *et al.*, 2014). In West Greenland, as glaciers continue to retreat and rock-slopes are debuttressed, the risk of catastrophic rock-slope failures and potential tsunami will be increasingly of interest to the burgeoning mineral and petroleum extraction industries that are active in the area (Smelror *et al.*, 2008). The extension of this research to include the assessment of tsunami hazard and risk in Vaigat should take advantage of this unique setting in order to provide better constraints on the performance of two fluid numerical models, which can then be applied to similar hazards in more populous regions.

Chapter 8

Conclusions

Perhaps one of the most pressing questions regarding catastrophic rock-slope failure in high latitudes is the potential response of rock-slope stability to climate change, specifically contemporary warming (Deline, 2009). The study presented here contributes to this active and growing area of research by using a unique cluster of 20 large rock avalanche deposits along the Vaigat Strait, West Greenland, as a test case for assessing paraglacial slope response as the Greenland Ice Sheet retreats and rock-slopes are debuttressed. Specifically, this research aimed to increase our understanding of rock avalanche dynamics by using a numerical model to undertake a sensitivity analysis of rock avalanche run-out, which was uniquely validated by a proximal population of rock avalanche deposits with comparable boundary conditions.

The simulations of the rock avalanches in Vaigat were performed using *VolcFlow*, a geophysical mass flow code originally developed to simulate volcanic debris avalanches. Rheological calibration of the model was performed using a well-constrained event at Paatuut (AD 2000). The best-fit simulation assumes a plastic-type rheology, using a constant retarding stress with a velocity-dependent law (T_0 = 250 kPa, ξ = 0.01) and simulating run-out distance to within ±0.3% of that observed. This calibration was applied to 19 other events, simulating rock avalanche motion across 3D terrain of varying levels of complexity and testing the sensitivity of the model to a range of topographic and geometric factors. The findings presented here illustrate the utility and sensitivity of employing a case-specific approach for the calibration of numerical models of rock avalanche run-out, alongside the validity of applying these rheological parameters elsewhere, even within similar boundary conditions. Specifically, this research concludes that:

A plastic-type rheology can plausibly account for the observed morphology of a series of deposits emplaced by events of different types.

Despite being widely used to simulate rock avalanche propagation, other models, that assume either a Coulomb frictional or a Voellmy rheology, failed to reproduce the observed event characteristics and deposit distribution at Paatuut. Instead, a plastic rheology with a velocity-dependent law best described the kinematics of the event and the morphology of the resultant deposit. A number of studies have successfully used a plastic rheology to simulate the run-out and emplacement dynamics of debris avalanches and pyroclastic flows. The limited ability of frictional models to simulate the behaviour of events such as these suggests that processes additional to those of granular flow dynamics are involved. Although the success of a plastic-type rheology over any other remains difficult to physically explain, it might indicate that the friction angle at the base of these mass movements cannot be considered constant as in many commonly used rheological models.

Provided that their morphological/geophysical conditions are regionally consistent, a series of events can be accurately simulated using a single set of parameters obtained by back-analysis of one well-constrained event alone.

>The majority of work to date has only provided broad envelopes of rheological properties unsuited to predictive scenario modelling, thereby precluding the development of a set of more generalised rules for behaviour across events in different settings. The rheological calibration obtained here shows encouraging results in the model's ability to simulate a series of events using a single set of parameters obtained by back-analysis of the Paatuut event alone, suggesting that first-order run-out prediction of events in this landscape is possible. However, as discussed below, further in-depth studies, as well as the development of a suitable probabilistic framework, are required prior to the application of this model for predictive purposes.

Numerical models of rock avalanche run-out are highly sensitive to the assumed source conditions.

>This work has demonstrated the value of applying a rheological parameter set to a group of rock avalanches that have occurred within regionally consistent boundary conditions (e.g. geology, palaeoenvironmental history, first-order order topography, and rock avalanche preparatory and triggering factors). However, the simulated run-out and behaviour of these events is strongly conditioned by the failure volume and its geometry, as well as the influence of substrate materials and path topography. Such aspects can vary strongly over short distances. This sensitivity of the model to the assumed source conditions attests to the importance of reliable and accurate data for successful model calibration and validation, and has important implications for future numerical run-out modelling.

8.1 Directions for future research

The findings presented here serve as a basis for future numerical modelling efforts concerned with rock avalanche run-out and the risks they pose in recently glaciated, fjord environments. It is clear that, while much research to date has focussed on more accessible and readily monitored sites, mountain ranges in polar regions such as Vaigat may be candidates for sudden regime shifts in rock-slope stability in the future (Kargel *et al.*, 2013). Large (tsunamigenic) rock avalanches from steep, deglaciating coastlines are therefore a scenario that may need to be increasingly accommodated in risk assessments (Korup and Dunning, *In Press*). To this end, future research should build on that presented here in order to:

1. **Refine our understanding of the plastic rheology, its use in numerical run-out modelling and its implications for the mechanical behaviour of rock avalanches.**
   This requires accurate field data from sites where a plastic rheology has been proven successful in reproducing the dynamics of past events, as well as the development of analogue modelling techniques that might be able to provide greater insights into how flows may be driven by a constant stress condition rather than a constant slope condition.

In particular, we need to establish whether there exist particular settings where a plastic rheology is most suitable for simulating rock avalanche propagation. Targeted calibration initiatives are required to determine whether a high constant retarding stress is characteristic of rock avalanches occurring along steep coastlines, where large volumes of material run out over limited distances and in a relatively short period of time.

2. **Determine whether there is a threshold volume below which a group of rock avalanches cannot be modelled satisfactorily using a single set of parameters.**

   The findings presented in this work indicate that assuming a constant retarding stress at the base of a flow may have a disproportionate influence on the simulated run-out of events of different magnitudes. This is indicative of a threshold volume below which rock avalanches in Vaigat, and perhaps other settings, cannot be modelled satisfactorily using a single set of parameters. If this threshold does exist, it is pertinent for future risk assessments as smaller rock avalanches (ca. $1x10^6$ m³) occur with greater frequency on human timescales. In addition, the deposits of such events are difficult to detect, often having been extensively reworked, resulting in the underestimation of their occurrence. Further calibration studies are therefore required to test whether this behaviour is exclusive to the plastic rheology, why such a threshold might exist and to assess the extent to which this condition varies across different settings.

3. **Elucidate the relative importance of key source conditions for successfully simulating rock avalanche run-out.**

   Although the research presented here sheds some light on the sensitivity of numerical run-out models to a number of key controlling factors, further research should be undertaken using the events in Vaigat in order to elucidate the relative importance of these factors, which remain difficult to isolate and test in almost all other settings. This knowledge could be used to set standards for the quality of input data used to constrain future models of rock avalanche run-out.

4. **Improve calibration and validation datasets for numerical models of rock avalanche run-out, with the ultimate aim of compiling a consistent and high quality database for future use.**

   Numerical run-out models critically depend upon realistic initial conditions. Successful back-analysis of past events and, by extension, predictive scenario modelling of future events, requires high quality data concerning: (i) the (potential) location and volume of rock-slope failure, (ii) the presence of erodible substrates, (iii) the location and rate of substrate entrainment, (iv) the presence of surface water (if any) along the run-out path, and (v) topographic constraints on run-out. In addition, recent advances in teleseismic source inversion techniques should be applied more widely to ensure that model results are dynamically consistent over the entire displacement process and not only in the final resting state. Targeted calibration initiatives involving these case studies could be used to

consider whether models truly demonstrate process representation, and whether there are particular environments or settings that preclude such analyses by virtue of a set of topographic and/or geometric characteristics.

5. **Develop a suitable framework that considers the application of numerical run-out models for predictive purposes and their incorporation into risk assessments.**

   Quantitative assessments of the future hazards posed by potential rock avalanches are crucial for risk assessment and management practices. Prior to the application of a numerical run-out model for forward modelling a potential future event, a systematic and computationally feasible procedure must be developed for incorporating probabilistic components into deterministic continuum dynamic models. The cost of traditional methods for sampling input parameter values, such as Monte Carlo and Latin Hypercube sampling, makes them unsuitable for these models, which are governed by conservation laws that are computationally intensive to evaluate. At present, so-called 'smart' Monte Carlo methods such as polynomial chaos quadrature remain sparsely applied and should be further developed for use in probabilistic run-out assessments.

6. **Increase our understanding of rock avalanche-triggered tsunami and to better constrain the factors that condition the severity of these events.**

   Although it is well known that the material flux at the point of entry into the water is critical in determining the magnitude of the resultant displacement wave, accurately modelling this flux remains challenging. A future challenge will be to compile a consistent, high quality database of subaerial and submarine deposits by using techniques such as airborne LiDAR and seismic profiling to locate geomorphic and sedimentary archives of past tsunamigenic events. Future work should therefore seek to expand the dataset presented here and use *VolcFlow* to back-analyse known subaerial-submerged events based on the location and form of their proximal marine deposits, with the ultimate aim of using this unique setting to provide better constraints on the performance of two fluid numerical models.

References

Abele, G. (1974) 'Bergstürze in den Alpen: ihre Verbreitung, Morphologie und Folgeerscheinungen', *Hauptausschüsse des Deutschen und des Österreichischen Alpenvereins*, 25:230 p.

Abdrakhmatov, K.E. and Strom, A.L. (2006) 'Dissected rockslide and rock-avalanche deposits, Tien Shan, Kyrgyzstan', in Evans, S.G., Mugnozza, G.S., Strom, A. and Hermanns, R.L. (Eds.) *Landslides from Massive Rock Slope Failure. Proceedings of the NATO Advanced Research Workshop on Massive Rock Slope Failure: New Models for Hazard Assessment, Celano, Italy, 16-21 June 2002*. Netherlands: Springer, pp.551-570.

Alean, J. (1985) 'Ice avalanches: some empirical information about their formation and reach', *Journal of Glaciology*, 31(109):324-333.

Allen, S.K., Cox, S.C. and Owens, I.F. (2011) 'Rock avalanches and other landslides in the central Southern Alps of New Zealand: a regional study considering possible climate change impacts', *Landslides*, 8(1):33-48.

Ancey, C. (2005) 'Monte Carlo calibration of avalanches as a Coulomb fluid', *Philosophical Transactions of the Royal Society A*, 363(1832):1529-1550.

Ayotte, D. and Hungr, O. (2000) 'Calibration of a runout prediction model for debris flows and avalanches', in Wieczorek, G.F. and Naeser, N.D. (Eds.) *Proceedings of the Second International Conference on Debris-Flow Hazards Mitigation*. Rotterdam: Balkema, pp.505-514.

Baldwin, J.E. (1987) 'The Martinez Mountain rock avalanche', in Guptil, P.D., Gath, E.M. and Ruff, R.W. (Eds.) *Geology of the Imperial Valley, California: Santa Ana, California, South Coast Geological Society Annual Field Trip Guidebook*. Volume 14, pp.37-48.

Ballantyne, C.K. (2002) 'Paraglacial geomorphology', *Quaternary Science Reviews*, 21(18-19):1935-2017.

Banton, J., Villard, P., Jongmans, D. and Scavia, C. (2009) 'Two-dimensional discrete element models of debris avalanches: Parameterization and the reproducibility of experimental results' *Journal of Geophysical Research: Earth Surface*, 114(F4):15 p.

Basgall, P.l., Kruse, F.A. and Olsen, R.C. (2014) 'Comparison of LiDAR and stereo photogrammetric point clouds for change detection', *Proceedings of the International Society for Optics and Photonics: Lasar Radar Technology and Applications*. 9080:14 p.

Begueria, S., van Asch, T.W.J., Malet, J.-P. and Grondahl, S. (2009) 'A GIS-based numerical model for simulating the kinematics of mud and debris flows over complex terrain', *Natural Hazards and Earth System Sciences*, 9(6):1897-1909.

Belousova, M.G. and Belousov, A.B. (1995) 'Prehistoric and 1933 debris avalanches and associated eruptions of Harimkotan Volcano (Kurile islands)', *Periodico di Mineralogia*, 64:99-101.

Belousov, A.B., Belousova, M.G. and Voight, B. (1999) 'Multiple edifice failures, debris avalanches and associated eruptions in the Holocene history of Shiveluch volcano, Kamchatka, Russia', *Bulletin of Volcanology*, 61(5):324-342.

Bernard, J., Kelfoun, K., Le Pennec, J.-L., and Vargas, S.V. (2014) 'Pyroclasic flow erosion and bulking processes: comparing field-based vs. modelling results at Tungurahua volcano,

Ecuador', *Bulletin of Volcanology*, 76(9):16 p.

Bingham, E.C. (1922) *Fluidity and Plasticity*. New York: McGraw-Hill, 466 p.

Blair, T.C. (1999) 'Form, facies, and depositional history of the North Long John rock avalanche, Owens Valley, California', *Canadian Journal of Earth Sciences*, 36(6):855-870.

Blikra, L.H., Longva, O., Harbitz, C. and Løvholt, F. (2005) 'Quantification of rock-avalanche and tsunami hazard in Storfjorden, western Norway', in Senneset, K., Flaate, K. and Larsen, J.O. (Eds.) *Landslides and Avalanches: Proceedings of the 11th International Conference and Field Trip on Landslides (ICFL) Norway, 1-10 September 2005*. London: Taylor & Francis, pp.57-64.

Blikra, L.H., Longva, O., Braathen, A., Anda, E., Dehls, J.F. and Stalsberg, K. (2006) 'Rock slope failures in Norwegian fjord areas: examples, spatial distribution and temporal pattern', in Evans, S.G., Mugnozza, G.S., Strom, A. and Hermanns, R.L. (Eds.) *Landslides from Massive Rock Slope Failure. Proceedings of the NATO Advanced Research Workshop on Massive Rock Slope Failure: New Models for Hazard Assessment, Celano, Italy, 16-21 June 2002*. Netherlands: Springer, pp.475-496.

Blikra, L.H. and Christiansen, H.H. (2014) 'A field-based model of permafrost-controlled rockslide deformation in northern Norway', *Geomorphology*, 208:34-49.

Bock, C.G. (1977) 'Martinez Mountain rock avalanche', in Coates, D.R. (Ed.) *Landslides: Reviews in Engineering Geology Volume III*. Boulder, Colorado: Geological Society of America, pp.155-168.

Bornhold, B.D., Harper, J.R., McLaren, D. and Thomson, R.E. (2007) 'Destruction of the first nations village of Kwalate by a rock avalanche-generated tsunami', *Atmosphere-Ocean*, 45(2):123-128.

Boultbee, N., Stead, D., Schwab, J. and Geertsema, M. (2006) 'The Zymoetz River rock avalanche, June 2002, British Columbia, Canada', *Engineering geology*, 83(1):76-93.

Bowman, E.T., Take, W.A., Rait, K.L. and Hann, C. (2012) 'Physical models of rock avalanche spreading behaviour with dynamic fragmentation', *Canadian Geotechnical Journal*, 49(4):460-476.

Brückl, E., Brückl, J. and Heuberger, H. (2001) 'Present structure and prefailure topography of the giant rockslide of Köfels', *Zeitschrift für Gletscherkunde und Glazialgeologie*, 37(1):49-79.

Bungum, H., Olesen, O., Pascal, C., Gibbons, S., Lindholm, C. and Vestøl, O. (2010) 'To what extent is the present seismicity of Norway driven by post-glacial rebound?', *Journal of the Geological Society*, 167(2):373-384.

Burbank, D.W., Leland, J., Fielding, E., Anderson, R.S., Brozovic, N., Reid, M.R. and Duncan, C. (1996) 'Bedrock incision, rock uplift and threshold hill slopes in the northwestern Himalayas', *Nature*, 379(6565):505-510.

Burtin, A., Hovius, N., Milodowski, D.T., Chen, Y.-G., Wu, Y.-M., Lin, C.-W., Chen, H., Emberson, R. and Leu, P.-L. (2013) 'Continuous catchment-scale monitoring of geomorphic processes with a 2-D seismological array', *Journal of Geophysical Research: Earth Surface*, 118(3):1956-1974.

Capra, L., Macías, J.L., Scott, K.M., Abrams, M. and Garduño-Monroy, V.H. (2002) 'Debris avalanches and debris flows transformed from collapses in the Trans-Mexican Volcanic Belt, Mexico: Behaviour, and implications for hazard assessment', *Journal of Volcanology and Geothermal Research*, 113(1):81-110.

Carrasco-Núñez, G., Vallance, J.W. and Rose, W.I. (1993) 'A voluminous avalanche-induced lahar from Citlaltépetl volcano, Mexico: Implications for hazard assessment', *Journal of Volcanology and Geothermal Research*, 59(1-2):35-46.

Catane, S.G., Cabria, H.B., Zarco, M.A.H., Saturay, R.M. and Mirasol-Robert, A.A. (2008) 'The 17 Feb 2006 Guinsaugon rock slide debris avalanche, Southern Leyte, Philippines: deposit characteristics and failure mechanism', *Bulletin of Engineering Geology and the Environment*, 67(3):305-320.

Charbonnier, S.J. and Gertisser, R. (2012) 'Evaluation of geophysical mass flow models using the 2006 block-and-ash flows of Merapi Volcano, Java, Indonesia: Towards a short-term hazard assessment tool', *Journal of Volcanology and Geothermal Research*, 231-232:87-108.

Charbonnier, S.J., Germa, A., Connor, C.B., Gertisser, R., Preece, K., Komorowski, J.-C., Lavigne, F., Dixon, T. and Connor, L. (2013) 'Evaluation of the impact of the 2010 pyroclastic density currents at Merapi volcano from high-resolution satellite imagery, field investigations and numerical simulations', *Journal of Volcanology and Geothermal Research*, 261(1):295-315.

Chen, J.H. and Lee, C.F. (2007) 'Landslide mobility analysis using MADflow', in Ho, K. and Hong, V.L. (Eds.) *Proceedings of the 2007 International Forum on Landslide Disaster Management*. Hong Kong: Hong Kong Geotechnical Engineering Office, pp.857-874.

Chow, V.T. (1959) *Open-channel Hydraulics*. New York: McGraw-Hill, 680 p.

Christen, M., Kowalski, J. and Bartelt, P. (2010) 'RAMMS: Numerical simulation of dense snow avalanches in three-dimensional terrain', *Cold Regions Science and Technology*, 63(1-2):1-14.

Clague, J.J. and Souther, J.G. (1982) 'The Dusty Creek landslide on Mount Cayley, British Columbia', *Canadian Journal of Earth Sciences*, 19:524-539.

Clarke, M.R.B. (1980) 'The reduced major axis of a bivariate sample', *Biometrika*, 67(2):441-446.

Cleary, P.W. and Prakash, M. (2004) 'Discrete-element modeling and smoothed particle hydrodynamics: Potential in the environmental sciences', *Philosophical Transactions of the Royal Society A*, 362(1822):2003-2030.

Collins, G.S. and Melosh, H.J. (2003) 'Acoustic fluidization and the extraordinary mobility of struzströms', *Journal of Geophysical Research: Solid Earth*, 108(B10):14 p.

Cook, R.D., Malkus, D.S., Plesha, M.E. and Witt, R.J. (2007) *Concepts and applications of finite element analysis*. 4th Edn. New Delhi: John Wiley & Sons, 736 p.

Corominas, J. (1996) 'The angle of reach as a mobility index for small and large landslides', *Canadian Geotechnical Journal*, 33(2):260-271.

Corominas, J., van Westen, C., Frattini, P., Cascini, L., Malet, J.-P., Fotopoulou, S., Catani, F., Van Den Eeckhaut, M., Mavrouli, O., Agliardi, F., Pitilakis, K., Winter, M.G., Pastor, M., Ferlisi, S., Tofani, V., Hervás, J. and Smith, J.T. (2014) 'Recommendations for the quantitative analysis of landslide risk', *Bulletin of Engineering Geology and the Environment*, 73(2):209-263.

Crandell, D.R. and Fahnestock, R.K. (1965) 'Rockfalls and rock avalanches from Little Tahoma Peak on Mount Rainier', *Bulletin of the United States Geological Survey*, 1221(A):36 p.

Crandell, D.R., Mullineaux, D.R., Sigafoos, R.S. and Rubin, M. (1974) 'Chaos Crags eruptions and rockfall-avalanches, Lassen Volcanic National Park, California', *Journal of Research of the United States Geological Survey*, 2(1):49-59.

Crosta, G.B., Imposimato, S. and Roddeman, D.G. (2003) 'Numerical modelling of large landslides stability and runout', *Natural Hazards and Earth System Sciences*, 3(6):528-538.

Crosta, G.B., Chen, H. and Lee, C.F. (2004) 'Replay of the 1987 Val Pola landslide, Italian Alps', *Geomorphology*, 60(1-2):127-146.

Crosta, G.B., Chen, H. and Frattini, P. (2006a) 'Forecasting hazard scenarios and implications for the evaluation of countermeasure efficiency for large debris avalanches', *Engineering*

Geology, 83(1-3):236-253.

Crosta, G.B., Imposimato, S. and Roddeman, D.G. (2006b) 'Continuum numerical modelling of flow-like landslides', in Evans, S.G., Mugnozza, G.S., Strom, A. and Hermanns, R.L. (Eds.) *Landslides from Massive Rock Slope Failure. Proceedings of the NATO Advanced Research Workshop on Massive Rock Slope Failure: New Models for Hazard Assessment, Celano, Italy, 16-21 June 2002*. Netherlands: Springer, pp.211-232.

Crosta, G.B., Frattini, P. and Fusi, N. (2007) 'Fragmentation in the Val Pola rock avalanche', *Journal of Geophysical Research: Earth Surface*, 112(F1):23 p.

Crosta, G.B., Imposimato, S. and Roddeman, D. (2008) 'Numerical modelling of entrainment/deposition in rock and debris-avalanches', *Engineering Geology*, 109(1-2):135-145.

Crosta, G.B., Imposimato, S. and Roddeman, D. (2009) 'Numerical modelling of entrainment/deposition in rock and debris-avalanches', *Engineering Geology*, 109(1-2):135-145.

Cruden, D.M. (1982) 'The Brazeau Lake slide, Jasper National Park, Alberta', *Canadian Journal of Earth Sciences*, 19(5):975-981.

Cruden, D.M. and Hungr, O. (1986) 'The debris of the Frank Slide and theories of rockslide-avalanche mobility', *Canadian Journal of Earth Sciences*, 23(3):425-432.

Cundall, P.A. and Strack, O.D.L. (1979) 'A discrete numerical model for granular assemblies', *Géotechnique*, 29(1):47-65.

Cuomo, S., Pastor, M., Cascini, L. and Giuseppa, C.C. (2014) 'Interplay of rheology and entrainment in debris avalanches: a numerical study', *Canadian Geotechnical Journal*, DOI: 10.1139/cgj-2013-0387.

Dade, W.B. and Huppert, H.E. (1998) 'Long-runout rockfalls', *Geology*, 26(9):803-806.

Dahl, M.-P., Gauer, P., Kalsnes, B., Mortensen, L., Jensen, N. and Veihe, A. (2013) 'Numerical runout simulation of debris avalanches in the Faroe Islands, North Atlantic Ocean', *Landslides*, 10(5):623-631.

Dahl-Jensen, T., Larsen, L.M., Pedersen, S.A.S., Pedersen, J., Jepsen, H.F., Pedersen, G.K., Nielsen, T., Pedersen, A.K., Platen-Hallermund, F.V. and Weng, W. (2004) 'Landslide and tsunami 21 November 2000 in Paatuut, West Greenland', *Natural Hazards*, 31(1):277-287.

Dalbey, K.R. Patra, A.K., Pitman, E.B., Bursik, M.I. and Sheridan, M.F. (2008) 'Input uncertainty propagation methods and hazard mapping of geophysical mass flows', *Journal of Geophysical Research: Solid Earth*, 113(B5):16 p.

Dalbey, K.R. (2009) *Predictive simulation and model based hazard maps of geophysical mass flows*. Unpublished PhD Thesis. State University of New York at Buffalo, 316 p.

Daly, R.A., Miller, W.G. and Rice, G.S. (1912) 'Report of the commission appointed to investigate Turtle Mountain, Frank, Alberta', *Memoirs of the Geological Survey of Canada*, 27:34 p.

Dam, G. and Sønderholm, M. (1998) 'Sedimentological evolution of a fault-controlled Early Paleocene incised valley system, Nuussuaq Basin, West Greenland', in Shanley, K.W. and McCabe, P.J. (Eds.) *Relative role of eustasy, climate and tectonism in continental rocks. Society of Economic Paleontologists and Mineralogists Special Publication*, 59:109-121.

Dam, G., Pedersen, G.K., Sønderholm, M., Midtgaard, H.H., Larsen, L.M., Nøhr-Hansen, H. and Pedersen, A.K. (2009) 'Lithostratigraphy of the Cretaceous-Palaeocene Nuussuaq Group, Nuussuaq Basin, West Greenland', *Geological Survey of Denmark and Greenland Bulletin*, 19:171 p.

D'Ambrosio, D.D., Di Gregorio, S. and Iovine, G. (2003) 'Simulating debris flows through a hexagonal cellular automata: SCIDDICA S3-hex', *Natural Hazards and Earth System Sciences*, 3(6):545-559.

Davies, T.R.H. (1982) 'Spreading of Rock Avalanche Debris by Mechanical Fluidization', *Rock Mechanics*, 15(1):9-24.

Davies, T.R.H., McSaveney, M.J. and Hodgson, K.A. (1999) 'A fragmentation-spreading model for long-runout rock avalanches', *Canadian Geotechnical Journal*, 36(6):1096-1110.

Davies, T.R.H. and McSaveney, M.J. (2009) 'The role of rock fragmentation in the motion of large landslides', *Engineering Geology*, 109(1-2):67-79.

Davies, T.R.H., McSaveney, M.J. and Kelfoun, K. (2011) 'Runout of the Socompa volcanic debris avalanche, Chile: a mechanical explanation for low basal shear resistance', *Bulletin of Volcanology*, 72(8):933-944.

De Blasio, F.V. and Elverhøi, A. (2008) 'A model for frictional melt production beneath large rock avalanches', *Journal of Geophysical Research: Earth Surface*, 113(F2):13 p.

De Blasio, F.V. (2009) 'Rheology of a wet, fragmenting granular flow and the riddle of the anomalous friction of large rock avalanches', *Granular Matter*, 11(3):179-184.

Deline, P. (2001) 'Recent Brenva rock avalanches (Valley of Aosta): new chapter in an old story', *Geografia Fisica e Dinamica Quaternaria*, 5:55-63.

Deline, P. (2009) 'Interactions between rock avalanches and glaciers in the Mont Blanc massif during the late Holocene', *Quaternary Science Reviews*, 28(11-12):1070-1083

Denham, L.R. (1974) 'Offshore geology of northern West Greenland (69° to 75°N)', *Rapport Grønlands Geologiske Undersøgelse*, 63:24 p.

Denlinger, R.P. and Iverson, R.M. (2001) 'Flow of variably fluidized granular masses across three-dimensional terrain: 2. Numerical predictions and experimental tests', *Journal of Geophysical Research: Solid Earth*, 106(B1):553-566.

Denlinger, R.P. and Iverson, R.M. (2004) 'Granular avalanches across irregular three-dimensional terrain: 1. Theory and computation', *Journal of Geophysical Research: Earth Surface*, 109(F1):14 p.

Devoli, G., De Blasio, F.V., Elverhøi, A. and Høeg, K. (2009) 'Statistical analysis of landslide events in Central America and their run-out distance', *Geotechnical and Geological Engineering*, 27(1):23-42.

Dondin, F., Lebrun, J.-F., Kelfoun, K., Fournier, N. and Randrianasolo, A. (2012) 'Sector collapse at Kick'em Jenny submarine volcano (Lesser Antilles): numerical simulation and landslide behaviour', *Bulletin of Volcanology*, 74(2):595-607.

Dufresne, A. (2009) *Influence of runout path material on rock and debris avalanche mobility: field evidence and analogue modelling*. Unpublished PhD Thesis. University of Canterbury, New Zealand, 284 p.

Dufresne, A. and Davies, T.R.H. (2009) 'Longitudinal ridges in mass movement deposits', *Geomorphology*, 105(3-4):171-181.

Dufresne, A., Davies, T.R.H. and McSaveney, M.J. (2010) 'Influence of runout-path material on emplacement of the Round Top rock avalanche, New Zealand', *Earth Surface Processes and Landforms*, 35(2):190-201.

Dufresne, A. (2012) 'Granular flow experiments on the interaction with stationary runout path materials and comparison to rock avalanche events', *Earth Surface Processes and Landforms*, 37(14):1527-1541.

Dunning, S.A. (2006) 'The grain-size distribution of rock-avalanche deposits in valley confined settings', *The Italian Journal of Engineering Geology and Environment*, 1:117-121.

Dunning, S.A., Mitchell, W.A., Rosser, N.J. and Petley, D.N. (2007) 'The Hattian Bala rock avalanche and associated landslides triggered by the Kashmir Earthquake of 8 October 2005', *Engineering Geology*, 93(3-4):130-144.

Dykstra, J.L. (2013) *The post-LGM evolution of Milford Sound, Fiordland, New Zealand, timing of ice retreat, the role of mass wasting & implications for hazards*. Unpublished PhD Thesis, University of Canterbury, New Zealand, 313 p.

Egashira, S., Honda, N. and Itoh, T. (2001) 'Experimental study on the entrainment of bed material into debris flow', *Physics and Chemistry of the Earth (C)*, 26(9):645-650.

Eidsvig, U.M., Medina-Cetina, Z., Kveldsvik, V., Glimsdal, S., Harbitz, C.B. and Sandersen, F. (2011) 'Risk assessment of a tsunamigenic rockslide at Åknes', *Natural hazards*, 56(2):529-545.

Eisbacher, G.H. (1979) 'Cliff collapse and rock avalanches (sturzströms) in the Mackenzie Mountains, northwestern Canada', *Canadian Geotechnical Journal*, 16(2):309-334.

Eisbacher, G.H. and Clague, J.J. (1984) *Destructive Mass Movements in High Mountains: Hazard and Management. Geological Survey of Canada Paper 84-16*. Ottowa: Geological Survey of Canada, 230 p.

Ekström, G. and Stark, C.P. (2013) 'Simple scaling of catastrophic landslide dynamics', *Science*, 339(6126):1416-1419.

Erismann, T.H. (1979) 'Mechanisms of large landslides', *Rock Mechanics*, 12(1):15-46.

Erismann, T.H. (1986) 'Flowing, rolling, bouncing, sliding: synopsis of basic mechanisms', *Acta Mechanica*, 64(1-2):101-110.

Erismann, T.H. and Abele, G. (2001) *Dynamics of Rockslides and Rockfalls*. New York: Springer, 316 p.

Evans, S.G. and Clague, J.J. (1988) 'Catastrophic rock avalanches in glacial environments', in Bonnard, C. (Ed.) *Landslides - Proceedings of the Fifth International Symposium on Landslides*. Rotterdam: Balkema, pp.1,153-1,158.

Evans, S.G. (1989) 'Rock avalanche run-up record', *Nature*, 340(6231):271.

Evans, S.G., Clague, J.J., Woodsworth, G.J. and Hungr, O. (1989) 'The Pandemonium Creek rock avalanche, British Columbia', *Canadian Geotechnical Journal*, 26(3):427-446.

Evans, S.G., Hungr, O. and Enegren, E.G. (1994) 'The Avalanche Lake rock avalanche, Mackenzie Mountains, Northwest Territories, Canada: description, dating and dynamics', *Canadian Geotechnical Journal*, 31(5):749-768.

Evans, S.G. and Clague, J.J. (1999) 'Rock avalanches on glaciers in the Coast and St. Elias Mountains, British Columbia', *Slope Stability and Landslides: Proceedings of the 13th Annual Vancouver Geotechnical Society Symposium*. Vancouver: BiTech Publishers, pp.115-123.

Evans, S.G., Hungr, O. and Clague, J.J. (2001) 'Dynamics of the 1984 rock avalanche and associated distal debris flow on Mount Cayley, British Columbia, Canada; implications for landslide hazard assessment on dissected volcanoes', *Engineering Geology*, 61(1):29-51.

Evans, S.G. and Couture, R. (2002) 'The 1965 Hope Slide, British Columbia; catastrophic failure of a sagging rock slope', *Geological Society of America: Abstracts with Programs*, 34:16-26.

Evans, S.G. (2006) 'Single-event landslides resulting from massive rock slope failure: characterising their frequency and impact on society', in Evans, S.G., Mugnozza, G.S., Strom, A.

and Hermanns, R.L. (Eds.) *Landslides from Massive Rock Slope Failure. Proceedings of the NATO Advanced Research Workshop on Massive Rock Slope Failure: New Models for Hazard Assessment, Celano, Italy, 16-21 June 2002*. Netherlands: Springer, pp.53-73.

Evans, S.G., Scarascia Mugnozza, G., Strom, A.L., Hermanns, R.L., Ischuk, A. and Vinnichenko, S. (2006) 'Landslides from massive rock slope failure and associated phenomena', in Evans, S.G., Mugnozza, G.S., Strom, A. and Hermanns, R.L. (Eds.) *Landslides from Massive Rock Slope Failure. Proceedings of the NATO Advanced Research Workshop on Massive Rock Slope Failure: New Models for Hazard Assessment, Celano, Italy, 16-21 June 2002*. Netherlands: Springer, pp.3-52.

Evans, S.G., Bishop, N.F., Smoll, L.F., Murillo, P.V., Delaney, K.B. and Oliver-Smith, A. (2009) 'A re-examination of the mechanism and human impact of catastrophic mass flows originating on Nevado Huascarán, Cordillera Blanca, Peru in 1962 and 1970', *Engineering Geology*, 108(1-2):96-118.

Fannin, R.J. and Wise, M.P. (2001) 'An empirical-statistical model for debris flow travel distance', *Canadian Geotechnical Journal*, 38(5):982-994.

Fischer, L., Kääb, A., Huggel, C. and Noetzli, J. (2006) 'Geology, glacier retreat and permafrost degradation as controlling factors of slope instabilities in a high-mountain rock wall: the Monte Rosa east face', *Natural Hazards and Earth System Sciences*, 6(5):761-772.

Fischer, L., Purves, R.S., Huggel, C., Noetzli, J. and Haeberli, W. (2012a) 'On the influence of topographic, geological and cryospheric factors on rock avalanches and rockfalls in high-mountain areas', *Natural Hazards and Earth System Sciences*, 12(1):241-254.

Fischer, J.T., Kowalski, J. and Pudasaini, S.P. (2012b) 'Topographic curvature effects in applied avalanche modeling', *Cold Regions Science and Technology*, 74-75:21-30.

Fort, M. and Peulvast, J.-P. (1995) 'Catastrophic mass-movements and morphogenesis in the Peri-Tibetan Ranges: examples from West Kunlun, East Pamir, and Ladakh', in Slaymaker, O. (Ed.) *Steepland Geomorphology*. New York: John Wiley & Sons, pp.171-198.

Fort, M. (2000) 'Glaciers and mass wasting processes: their influence on the shaping of Kali Gandaki Valley, Nepal', *Quaternary International*, 65-66:101-119.

Francis, P.W. and Wells, G.L. (1988) 'Landsat thematic mapper observation of debris avalanche deposits in Central Andes', *Bulletin of Volcanology*, 50(4):258-278.

Frayssines, M. and Hantz, D. (2006) 'Failure mechanisms and triggering factors in calcareous cliffs of the Subalpine Ranges (French Alps)', *Engineering Geology*, 86(4):256-270.

Friedmann, S.J. (1997) 'Rock avalanches of the Miocene Shadow Valley basin, eastern Mojave Desert, California: Processes and Problems', *Journal of Sedimentology*, 67(5):792-804.

Friedmann, S.J., Kwon, G. and Losert, W. (2003) 'Granular memory and its effect on the triggering and distribution of rock avalanche events', *Journal of Geophysical Research: Solid Earth*, 108(B8):12 p.

Fuganti, A. (1969) 'Studio geologico di sei grandi frane di roccia nella regione Trentino-Alto Adige', *Memorie del Museo Tridentino di Scienze Naturali*, 17(3):1-72.

Funder, S. and Hansen, L. (1996) 'The Greenland ice sheet – a model for its culmination and decay during and after the last glacial maximum', *Geological Survey of Denmark and Greenland Bulletin*, 42:16 p.

Geertsema, M., Clague, J.J., Schwab, J.W. and Evans, S.G. (2006) 'An overview of recent large catastrophic landslides in northern British Columbia, Canada', *Engineering Geology*, 83(1-3):120-143.

Geronimo-Catane, S. (1994) 'Mode of emplacement of two debris-avalanche deposits at Banahao

volcano, southern Luzon, Philippines', *Bulletin of the Volcanological Society of Japan*, 39(3):113-127.

Giachetti, T., Paris, R., Kelfoun, K. and Perez-Torrado, F.J. (2011) 'Numerical modelling of the tsunami triggered by the Güìmar debris avalanche, Tenerife (Canary Islands): Comparison with field-based data', *Marine Geology*, 284(1-4):189-202.

Giachetti, T., Paris, R., Kelfoun, K. and Ontowirjo, B. (2012) 'Tsunami hazard related to a flank collapse of Anak Krakatau Volcano, Sunda Strait, Indonesia', *Geological Society, London, Special Publications*, 361(1):79-90.

Gigli, G., Fanti, R., Canuti, P. and Casagli, N. (2011) 'Integration of advanced monitoring and numerical modelling techniques for the complete risk scenario analysis of rockslides: The case of Mt. Beni (Florence, Italy)', *Engineering Geology*, 120(1-4):48-59.

Giribabu, D., Kumar, P., Mathew, J., Sharma, K.P. and Murthy, Y.V.N.K. (2013) 'DEM generation using Cartosat-1 stereo data: issues and complexities in Himalayan terrain', *European Journal of Remote Sensing*, 46:431-443.

Glade, T. and Crozier, M.J. (2005) 'The nature of landslide hazard impact', in Glade, T., Anderson, M.G. and Crozier, M.J. (Eds.) *Landslide Hazard and Risk*. Chichester: John Wiley & Sons, pp.43-74.

Goguel, J. and Pachoud, A. (1972) 'Geology and dynamics of the rockfall of the Granier Range which occurred in November 1248', *Bulletin: Bureau de Récherches Geologiques et Miniéres, Hydrogeologie, Lyon*, 1:29-38.

Golts, S. and Rosenthal, E. (1993) 'A morphotectonic map of the northern Arava in Israel, derived from isobase lines', *Geomorphology*, 7(4):305-315.

Gruber, S. and Haeberli, W. (2007) 'Permafrost in steep bedrock slopes and its temperature-related destabilization following climate change', *Journal of Geophysical Research: Earth Surface*, 112(F2):10 p.

Hadley, J.B. (1959) 'The Madison Canyon Landslide', *Geotimes*, 4(3):14-17.

Harbitz, C.B., Glimsdal, S., Løvholt, F., Kveldsvik, V., Pedersen, G.K. and Jensen, A. (2014) 'Rockslide tsunamis in complex fjords: 'From an unstable rock slope at Åkerneset to tsunami risk in western Norway', *Coastal Engineering*, 88:101-122.

Harrison, J.V. and Falcon, N.L. (1938) 'An ancient landslip at Saidmarreh in south-western Iran', *The Journal of Geology*, 46(3):296-309.

Harrison, K.P. and Grimm, R.E. (2003) 'Rheological constraints on Martian landslides', *Icarus*, 163(2):347-362.

Hayashi, J.N. and Self, S. (1992) 'A comparison of pyroclastic flow and debris avalanche mobility', *Journal of Geophysical Research: Solid Earth*, 97(B6):9063-9071.

Heim, A. (1882) 'Der Bergstürz von Elm', *Zeitschrift der Deutschen Geologischen Gesellschaft*, 34(1):74-115.

Heim, A. (1932) *Bergstürz und Menschenleben*. Zürich: Fretz & Wasmuth Verlag, 218 p.

Henderson, G. (1969) 'Oil and gas prospects in the Cretaceous–Tertiary basin of West Greenland', *Rapport Grønlands Geologiske Undersøgelse*, 22:63 p.

Hermanns, R.L. and Strecker, M.R. (1999) 'Structural and lithological controls on large Quaternary rock avalanches (stürzstroms) in arid northwestern Argentina', *Geological Society of America Bulletin*, 111(6):934-948.

Hermanns, R.L., Sepúlveda, S.A., Amblas, D., Canals, M., Azpiroz, M., Bascuñán, I, Calafat, A.M.,

Duhart, P., Frigola, J., Iglesias, O., Kempf, P., Lafuerza, S., Longva, O., Micallef, A., Oppikofer, T., Rayo, X., Vargas, G. and Molina, F.Y. (2014) 'Earthquake-triggered subaerial landslides that caused large scale fjord sediment deformation: combined subaerial and submarine studies of the 2007 Aysén Fjord event, Chile' in Lollino, G., Manconi, A., Locat, J., Huang, Y. and Artigas, M.C. (Eds.) *Engineering Geology for Society and Territory. Volume 4: Marine and Coastal Processes.* London: Springer, pp.67-70.

Heuberger, H., Masch, L., Preuss, E. and Strecker, A. (1984) 'Quaternary landslides and rock fusion in Central Nepal and the Tyrolean Alps', *Mountain Research and Development*, 4(4):345-362.

Hewitt, K. (1999) 'Quaternary Moraines vs Catastrophic Rock Avalanches in the Karakoram Himalaya, Northern Pakistan', *Quaternary Research*, 51(3):220-237.

Hewitt, K. (2002) 'Styles of rock-avalanche depositional complexes conditioned by very rugged terrain, Karakoram Himalaya, Pakistan', in Evans, S.G. and DeGraff, J.V. (Eds.) *Catastrophic landslides: effects, occurrence and mechanisms, Reviews in Engineering Geology Volume XV*. Boulder, Colorado: Geological Society of America. pp.345-377.

Hewitt, K. (2006) 'Rock avalanches with complex run out and emplacement, Karakoram Himalaya, Inner Asia' in Evans, S.G., Mugnozza, G.S., Strom, A. and Hermanns, R.L. (Eds.) *Landslides from Massive Rock Slope Failure. Proceedings of the NATO Advanced Research Workshop on Massive Rock Slope Failure: New Models for Hazard Assessment, Celano, Italy, 16-21 June 2002*. Netherlands: Springer, pp.521-550.

Hewitt, K., Clague, J.J. and Orwin, J.F. (2008) 'Legacies of catastrophic rock slope failures in mountain landscapes', *Earth Science Reviews*, 87(1-2):1-38.

Hoek, E. and Bray, J. (1981) *Rock Slope Engineering*. 3rd Edn. London: Taylor & Francis, 368 p.

Hogan, K.A., Dowdeswell, J.A. and Ó Cofaigh, C. (2012) 'Glacimarine sedimentary processes and depositional environments in an embayment fed by West Greenland ice streams', *Marine Geology*, 311-314:1-16.

Holland, D.M., Thomas, R.H., deYoung, B., Ribergaard, M.H. and Lyberth, B. (2008) 'Acceleration of Jakobshavn Isbrae triggered by warm sub-surface ocean waters', *Nature Geoscience*, 1(10):659-664.

Hovius, N., Stark, C. and Allen, P. (1997) 'Sediment flux from a mountain belt derived by landslide mapping', *Geology*, 25(3):231-234.

Howat, I.M., Negrete, A. and Smith, B.E. (2014) 'The Greenland Ice Mapping Project (GIMP) land classification and surface elevation datasets', *The Cryosphere*, 8(4):1509-1518.

Hsü, K.J. (1975) 'Catastrophic debris streams (struzströms) generated by rockfalls', *Geological Society of America Bulletin*, 86(1):129-140.

Hsü, K.J. (1978) 'Albert Heim: observations of landslides and relevance to modern interpretations', in Voight, B. (Ed.) *Rockslides and Avalanches 1: Natural Phenomena.* Amsterdam: Elesvier, pp.70-93.

Huggel, C., Kääb, A., Haeberli, W. and Krummenacher, B. (2003) 'Regional-scale GIS-models for assessment of hazards from glacier lake outbursts: evaluation and application in the Swiss Alps', *Natural Hazards and Earth System Science*, 3(6):647-662.

Huggel, C., Zgraggen-Oswald, S., Haeberli, W., Kääb, A., Polkvoj, A., Galushkin, I. and Evans, S.G. (2005) 'The 2002 rock/ice avalanche at Kolka/Karmadon, Russian Caucasus: assessment of extraordinary avalanche formation and mobility, and application of QuickBird satellite imagery', *Natural Hazards and Earth System Science*, 5(2):173-187.

Huggel, C., Caplan-Auerbach, J., Waythomas, C.F. and Wessels, R.L. (2007) 'Monitoring and modeling ice–rock avalanches from ice-capped volcanoes: a case study of frequent large

avalanches on Iliamna Volcano, Alaska', *Journal of Volcanology and Geothermal Research*, 168(1-4):114-136.

Huggel, C., Fischer, L., Schneider, D. and Haeberli, W. (2010) 'Research advances on climate-induced slope instability in glacier and permafrost high-mountain environments', *Geographica Helvetica*, 65(2):146-156.

Humlum, O. (1992) 'Observations on rock moisture variability in gneiss and basalt under natural Arctic conditions', *Geografiska Annaler*, 74A:197-205.

Hungr, O. (1981) *Dynamics of rock avalanches and other types of mass movements*. Unpublished PhD Thesis. University of Alberta, Canada, 500 p.

Hungr, O. (1995) 'A model for the runout analysis of rapid flow slides, debris flows, and avalanches', *Canadian Geotechnical Journal*, 32(4):610-623.

Hungr, O. and Evans, S.G. (1996) 'Rock avalanche runout prediction using a dynamic model', in Senneset, K. (Ed.) *Proceedings of the 7th International Symposium on Landslides, Trondheim, Norway, 16-21 June 1996.* Rotterdam: Balkema, 1:223-238.

Hungr, O. and Evans, S.G. (2004) 'Entrainment of debris in rock avalanches: An analysis of a long run-out mechanism', *Geological Society of America Bulletin*, 116(9-10):1240-1252.

Hungr, O., Corominas, J. and Eberhardt, E. (2005) 'Estimating landslide motion mechanism, travel distance and velocity', in Hungr, O., Fell, R., Couture, R. and Eberhardt, E. (Eds.) *Landslide risk management.* London: Taylor & Francis, pp.99-128.

Hungr, O. (2006) 'Rock avalanche occurrence, process and modelling', in Evans, S.G., Mugnozza, G.S., Strom, A. and Hermanns, R.L. (Eds.) *Landslides from Massive Rock Slope Failure*. *Proceedings of the NATO Advanced Research Workshop on Massive Rock Slope Failure: New Models for Hazard Assessment, Celano, Italy, 16-21 June 2002*. Netherlands: Springer, pp.243-266.

Hungr, O., Morgenstern, N. and Wong, H.N. (2007) 'Review of benchmarking exercises on landslide debris run-out and mobility modelling', in Ho, K. and Hong, V.L. (Eds.) *Proceedings of the 2007 International Forum on Landslide Disaster Management*. Hong Kong: Hong Kong Geotechnical Engineering Office, pp.755-812.

Hungr, O. and McDougall, S. (2009) 'Two numerical models for landslide dynamic analysis', *Computers and Geosciences*, 35(5):978-992.

Hunter, G. and Fell, R. (2003) 'Travel distance angle for "rapid" landslides in constructed and natural soil slopes', *Canadian Geotechnical Journal*, 40(6):1123-1141.

Hutchinson, J.N. (1986) 'A sliding-consolidation model for flow slides', Canadian Geotechnical Journal, 23(2):115-126.

Hutter, K., and Nohguchi, U. (1990) 'Similarity solutions for a Voellmy model of snow avalanches with finite mass', *Acta Mechanica*, 82(1-2):99-127.

Hutter, K., Koch, T., Pluss, C. and Savage, S.B. (1995) 'The dynamics of avalanches of granular materials from initiation to runout. Part II. Experiments', *Acta Mechanica*, 109(1-4):127-165.

Imre, B., Laue, J. and Springman, S.M. (2010) 'Fractal fragmentation of rocks within sturzströms: insight derived from physical experiments within the ETH geotechnical drum centrifuge', *Granular Matter*, 12(3):267-285.

Iverson, R.M., Reid, M. and Lahusen, R. (1997) 'Debris flow mobilization from landslides', *Annual Reviews Earth Planetary Sciences*, 25:85-138.

Iverson, R.M., Schilling, S.P. and Vallance, J.W. (1998) 'Objective delineation of lahar-inundation hazard zones', *Geological Society of America Bulletin*, 110(8):972-984.

Iverson, R.M. and Denlinger, R.P. (2001) 'Flow of variably fluidized granular masses across three-dimensional terrain: 1. Coulomb mixture theory', *Journal of Geophysical Research: Solid Earth*, 106(B1):537-552.

Iverson, R.M. and Vallance, J.W. (2001) 'New views of granular mass flows', *Geology*, 29(2):115-118.

Iverson, R.M. (2003) 'How should mathematical models of geomorphic processes be judged?', in Wilcock, P.R. and Iverson, R.M. (Eds.) *Prediction in Geomorphology*. Washington, D.C.: *American Geophysical Union*, pp.83-94.

Iverson, R.M. (2006) 'Forecasting runout of rock and debris avalanches', in Evans, S.G., Mugnozza, G.S., Strom, A. and Hermanns, R.L. (Eds.) *Landslides from Massive Rock Slope Failure. Proceedings of the NATO Advanced Research Workshop on Massive Rock Slope Failure: New Models for Hazard Assessment, Celano, Italy, 16-21 June 2002*. Netherlands: Springer, pp.197-209.

Iverson, R.M., Reid, M.E., Logan, M., LaHusen, R.G., Godt, J.W. and Griswold, J.P. (2010) 'Positive feedback and momentum growth during debris-flow entrainment of wet bed sediment', *Nature Geoscience*, 4(2):116-121.

Iverson, R.M. (2012) 'Elementary theory of bed-sediment entrainment by debris flows and avalanches', *Journal of Geophysical Research: Earth Surface*, 117(F3):17 p.

Iverson, R.M. (2014) 'Debris flows: behaviour and hazard assessment', *Geology Today*, 30(1):15-20.

Jaboyedoff, M., Baillifard, F., Couture, R., Locat, J. and Locat, P. (2004) 'Toward preliminary hazard assessment using DEM topographic analysis and simple mechanic modeling', in Lacerda, W.A., Ehrlich, M., Fontoura, A.B. and Sayo, A. (Eds.) *Landslides Evaluation and Stabilization*. Rotterdam: Balkema, pp.191-197.

Jaboyedoff, M., Couture, R. and Locat, P. (2009) 'Structural analysis of Turtle Mountain (Alberta) using digital elevation model: Toward a progressive failure', *Geomorphology*, 103(1):5-16.

Jaboyedoff, M., Oppikofer, T., Derron, M.-H., Blikra, L.H., Böhme, M. and Saintot, A. (2011) 'Complex landslide behaviour and structural control: a three-dimensional conceptual model of Åknes rockslide, Norway', *Geological Society, London, Special Publications*, 351:147-161.

Jaboyedoff, M., Daicz, S., Derron, M.H., Penna, I. and Rudaz, B. (2013) 'Defining the volume and geometry of the landslide failure surfaces: a review with emphasis on the Sloping Local Base Level (SLBL)', *EGU General Assembly Conference Abstracts*, 15:9431.

James, L.A., Hodgson, M.E., Ghoshal, S., Latiolais, M.M. (2012) 'Geomorphic change detection using historic maps and DEM differencing: The temporal dimension of geospatial analysis', *Geomorphology*, 137(1):181-198.

Jibson, R.W., Harp, E.L., Schulz, W. and Keefer, D.K. (2006) 'Large rock avalanches triggered by the M 7.9 Denali fault, Alaska, earthquake of 3 November 2002', *Engineering Geology*, 83(1-3):144-160.

Jiskoot, H. (2011) 'Long-runout rockslide on glacier at Tsar Mountain, Canadian Rocky Mountains: potential triggers, seismic and glaciological implications', *Earth Surface Processes and Landforms*, 36(2):203-216.

Johnson, B. (1978) 'Blackhawk landslide, California, USA', in *Rockslides and avalanches 1: natural phenomena.* Amsterdam: Elsevier, pp.481-504.

Jop, P., Forterre, Y. and Pouliquen, O. (2006) 'A constitutive law for dense granular flow', *Nature*, 441(7094):727-730.

Joughin, I., Das, S.B., King, M.A., Smith, B.E., Howat, I.M. and Moon, T. (2008) 'Seasonal speedup

along the Western flank of the Greenland Ice Sheet', *Science*, 320(5877):781-783.

Kargel, J., Bush, A. and Leonard, G. (2013) 'Arctic warming and sea ice diminution herald changing glacier and cryospheric hazard regimes', *EGU General Assembly Conference Abstracts*, 15:14188.

Keefer, D.K. (1984) 'Rock avalanches caused by earthquakes: Source characteristics', *Science*, 223(4642):1288-1290.

Keefer, D.K. and Larsen, M.C. (2007) 'Assessing landslide hazards', *Science*, 316(5828):1136-1138.

Kelfoun, K. and Druitt, T.H. (2005) 'Numerical modelling of the emplacement of Socompa rock avalanche, Chile', *Journal of Geophysical Research: Solid Earth*, 110(B12):13 p.

Kelfoun, K., Druitt, T.H., de Vries, B.V.W. and Guilbaud, M.-N. (2008) 'Topographic reflection of the Socompa debris avalanche, Chile', *Bulletin of Volcanology*, 70(10):1169-1187.

Kelfoun, K., Samaniego, P., Palacios, P. and Barba, D. (2009) 'Testing the suitability of frictional behaviour for pyroclastic flow simulation by comparison with a well-constrained eruption at Tungurahua volcano (Ecuador)', *Bulletin of Volcanology*, 71(9):1057-1075.

Kelfoun, K., Giachetti, T. and Labazuy, P. (2010) 'Landslide-generated tsunamis at Reunion Island', *Journal of Geophysical Research: Earth Surface*, 115(F4):17 p.

Kelfoun, K. (2011) 'Suitability of simple rheological laws for the numerical simulation of dense pyroclastic flows and long-runout volcanic avalanches', *Journal of Geophysical Research: Solid Earth*, 116(B8):14 p.

Kilburn, C.R.J. and Sørensen, S.-A. (1998) 'Runout length of sturzströms: The control of initial conditions and of fragment dynamics', *Journal of Geophysical Research: Solid Earth*, 103(B8):17877-17884.

Kirkbride, M.P. and Winkler, S. (2012) 'Correlation of Late Quaternary moraines: impact of climate variability, glacier response, and chronological resolution', *Quaternary Science Reviews*, 46:1-29.

Kojan, E. and Hutchinson, J.D. (1978) 'Mayunmarca rockslide and debris flow, Peru' in Voight, B. (Ed.) *Rockslides and Avalanches - I, Natural phenomena.* Amsterdam: Elesvier, pp.315-361.

Körner, H. (1976) 'Reichweite und Geschwindigkeit von Bergstürzen und Fleiβschneelawinen', *Rock Mechanics*, 1(8):225-256.

Korup, O. (2006) 'Effects of large deep-seated landslides on hillslope morphology, western Southern Alps, New Zealand', *Journal of Geophysical Research: Earth Surface*, 111(F1):18 p.

Korup, O., Clague, J.J., Hermanns, R.L., Hewitt, K., Strom, A.L. and Weidinger, J.T. (2007) 'Giant landslides, topography and erosion', *Earth and Planetary Science Letters*, 261(3-4):578-589.

Korup, O. and Dunning, S.A. (In Press) 'Catastrophic mass wasting in high mountains', in Huggel, C., Clague, J.J., Kääb, A. and Carey, J. (Eds.) *The High Mountain Cryosphere: Environmental Changes and Human Risks*. Cambridge University Press.

Kwam, J.S.H. and Sun, H.W. (2006) 'An improved landslide mobility model', *Canadian Geotechnical Journal*, 43(5):531-539.

Larsen, I.J., Montgomery, D.R. and Korup, O. (2010) 'Landslide erosion controlled by hillslope material', *Nature Geoscience*, 3(4):247-251.

Lauknes, T.R., Piyush Shanker, A., Dehls, J.F., Zebker, H.A., Henderson, I.H.C. and Larsen, Y. (2010) 'Detailed rockslide mapping in northern Norway with small baseline and persistent

scatterer interferometric SAR time series methods', *Remote Sensing of Environment*, 114(9):2097-2109.

Lecointre, J.A., Neall, V.E., Wallace, C.R. and Prebble, W.M. (2002) 'The 55-to 60-ka Te Whaiau Formation: a catastrophic, avalanche-induced, cohesive debris-flow deposit from Proto-Tongariro Volcano, New Zealand', *Bulletin of Volcanology*, 63(8):509-525.

Legros, F., Cantagrel, J.-M. and Bertrand, D. (2000) 'Pseudotachylyte (frictionite) at the base of the Arequipa volcanic landslide deposit (Peru): Implications for emplacement mechanisms', *Journal of Geology*, 108(5):601-611.

Legros, F. (2003) 'The mobility of long-runout landslides', *Engineering Geology*, 63(3-4):301-331.

Leith, K., Moore, J.M., Amann, F. and Loew, S. (2014) 'In situ stress control on microcrack generation and macroscopic extensional fracture in exhuming bedrock', *Journal of Geophysical Research: Solid Earth*, 119(1):594-615.

Long, A.J. and Roberts, D.H. (2003) 'Late Weichselian deglacial history of Disko Bugt, West Greenland, and the dynamics of the Jakobshavns Isbræ ice stream', *Boreas*, 32(1):208-226.

Long, A.J., Woodroffe, S.A., Roberts, D.H. and Dawson, S. (2011) 'Isolation basins, sea-level changes and the Holocene history of the Greenland Ice Sheet', *Quaternary Science Reviews*, 30(27):3748-3768.

Louge, M.Y. (2003) 'A model for dense granular flows down bumpy inclines', *Physical Review E*, 76(6):11 p.

Løvholt, F., Pedersen, G. and Gisler, G. (2008) 'Oceanic propagation of a potential tsunami from the La Palma Island', *Journal of Geophysical Research: Oceans*, 113(C9):21 p.

Lu, Z.Y., Rollerson, T. and Geertsema, M. (2003) 'The Mosque Mountain rock slide, Sustut watershed, Fort St. James, northern British Columbia, Canada', *Proceedings of the 3rd Canadian Conference on Geotechnique and Natural Hazards*. Edmonton: The Canadian Geotechnical Society, p.325.

Lucchitta, B.K. (1979) 'Landslides in Valles Marineris, Mars', *Journal of Geophysical Research: Solid Earth*, 84(B14):8097-8113.

Luhr, J.F. and Prestegaard, K.L. (1988) 'Caldera formation at Volcán de Colima, Mexico, by large Holocene volcanic debris avalanche', *Journal of Volcanology and Geothermal Research*, 35(4):335-348.

Luna, B.Q., van Westen, C.J., Jetten, V., Cepeda, J., Stumpf, A., Malet, J.P. and van Asch, T.W.J. (2010) 'A preliminary compilation of calibrated rheological parameters used in dynamic simulations of landslide run-out', in Malet, J.-P., Glade, T. and Casagli, N. (Eds.) *Mountain risks: bringing science to society. Proceedings of the Mountain Risks International Conference*. Firenze, Italy: CERG Strasbourg, pp.255-260.

Luna, B.Q., Cepeda, J., Stumpf, A., van Westen, C.J., Remaître, A., Malet, J.-P. and van Asch, T.W.J. (2013) 'Analysis and uncertainty quantification of dynamic run-out model parameters for landslides' in Margottini, C., Canuti, P. and Sassa, K. (Eds.) *Landslide Science and Practice, Volume 3: Spatial analysis and modelling*. pp.315-318.

Malamud, B.D., Turcotte, D.L., Guzzetti, F. and Reichenbach, P. (2004) 'Landslide inventories and their statistical properties', *Earth Surface Processes and Landforms*, 29(6):687-711.

Mangeney, A., Heinrich, P. and Roche, R. (2000) 'Analytical solution for testing debris avalanche numerical models', *Pure and Applied Geophysics*, 157(6-8):1081-1096.

Mangeney-Castelnau, A., Bouchut, F., Vilotte, J.P., Lajeunesse, E., Aubertin, A. and Pirulli, M. (2005) 'On the use of Saint Venant equations to simulate the spreading of a granular mass', *Journal of Geophysical Research: Solid Earth*, 110(B9):17 p.

Mangeney, A., Bouchut, N. Thomas, J.P. Vilotte and Bristeau, M.O. (2007), Numerical modeling of self-channeling granular flows and of their levee-channel deposits, *Journal of Geophysical Research: Earth Surface*, 112(F2):21 p.

Manzella, I. and Labiouse, V. (2013) 'Empirical and analytical analyses of laboratory granular flows to investigate rock avalanche propagation', *Landslides*, 10(1):23-36.

Marcussen, C., Chalmers, J.A., Andersen, H.L., Rasmussen, R. and Dahl-Jensen, T. (2001) 'Acquisition of high-resolution multichannel seismic data in the offshore part of the Nuussuaq Basin, central West Greenland', *Geological Survey of Denmark and Greenland Bulletin*, 189:34-40.

Matthews, W.H. and McTaggart, K.C. (1969) 'The Hope Landslide, British Columbia', *Proceedings of the Geological Association of Canada*, 20:65-75.

Mauthner, T.E. (1995) *Observations and preliminary assessment of the Kshwan Glacier rock avalanche, near Stewart in northwestern British Columbia*. Unpublished BA Sc. Thesis, University of British Columbia, Canada.

McArdell, B.W., Bartelt, P. and Kowalski, J. (2007) 'Field observations of basal forces and fluid pore pressure in a debris flow', *Geophysical Research Letters*, 34(7):L07406.

McConnell, R.G. and Brock, R.W. (1904) *Report on the great landslide at Frank, Alberta.* Ottawa, Canada: Department of the Interior, Part 8:1-17.

McColl, S.T. (2012) 'Paraglacial rock-slope stability', *Geomorphology*, 153-154:1-16.

McCoy, S.W., Kean, J.W., Coe, J.A., Tucker, G.E., Staley, D.M. and Wasklewicz, T.A. (2012) 'Sediment entrainment by debris flows: in situ measurements from the headwaters of a steep catchment', *Journal of Geophysical Research: Earth Surface*, 117(F3):25 p.

McDougall, S. and Hungr, O. (2004) 'A model for the analysis of rapid landslide motion across three-dimensional terrain', *Canadian Geotechnical Journal*, 41(6):1084-1097.

McDougall, S. and Hungr, O. (2005) 'Dynamic modelling of entrainment in rapid landslides', *Canadian Geotechnical Journal*, 42(5):1437-1448.

McDougall, S. (2006) *A new continuum dynamic model for the analysis of extremely rapid landslide motion across complex 3D terrain*. Unpublished PhD thesis. University of British Columbia, Canada, 268 p.

McDougall, S., Pirulli, M., Hungr, O. and Scavia, C. (2008) 'Advances in landslide continuum dynamic modelling', in Chen, Z., Zhang, J., Li, Z., Wu, F. and Ho, K. (Eds.) *Proceedings of the 10th International Symposium on Landslides and Engineered Slopes*. London: Taylor and Francis, pp.145-157.

McDougall, S., McKinnon, M. and Hungr, O. (2012) 'Developments in landslide runout prediction', in Clague, J.J. and Stead, D. (Eds.) *Landslides: Types, Mechanisms and Modeling*. New York: Cambridge University Press, pp.187-195.

McEwen, A.S. and Malin, M.C. (1989) 'Dynamics of Mount St. Helens' 1980 pyroclastic flows, rockslide-avalanche, lahars, and blast', *Journal of Volcanology and Geothermal Research*, 37(3-4):205-231.

McKinnon, M. (2010) *Landslide runout: Statistical analysis of physical characteristics and model parameters.* Unpublished MSc thesis. University of British Columbia, Canada, 405 p.

McLellan, P.J, and Kaiser, P.K. (1984) 'The Rockslide Pass rock avalanche, Mackenzie Mountains, N.W.T.', *Canadian case histories: Landslides. Preprint volume for the 37th Canadian Geotechnical Conference*. Toronto: Canadian Geotechnical Society, pp.135-140.

McSaveney, M.J. (1978) 'Sherman glacier rock avalanche, Alaska, USA', *in* Voight, B. (Ed.)

Rockslides and Avalanches, Natural Phenomena. Amsterdam: Elsevier, pp.197-258.

McSaveney, M.J. and Davies, T.R.H. (2007) 'Rockslides and their motion', in Sassa, K., Fukuoka, H., Wang, F.W. and Wang, G. (Eds.) *Progress in Landslide Science*. Berlin: Springer, pp.113-133.

Medina, V., Hürlimann, M. and Bateman, A. (2008) 'Application of FLATModel, a 2D finite volume code, to debris flows in the northeastern part of the Iberian Peninsula', *Landslides*, 5(1):127-142.

Mehl, K.W. and Schmincke, H.U. (1999) 'Structure and emplacement of the Pliocene Roque Nublo debris avalanche deposit, Gran Canaria, Spain', *Journal of Volcanology and Geothermal Research*, 94(1):105-134.

Melosh, H.J. (1979) 'Acoustic fluidisation: a new geologic process?', *Journal of Geophysical Research: Solid Earth*, 84(B13):7513-7520.

Melosh, H.J. (1986) 'The physics of very large landslides', *Acta Mechanica*, 64(1-2):89-99.

Middleton, G.V. and Wilcock, P.R. (1994) *Mechanics in the Earth and Environmental Sciences*. Cambridge: Cambridge University Press, 459 p.

Miller, D.J., (1960) 'The Alaska earthquake of July 10, 1958: giant wave in Lituya Bay', *Bulletin of the Seismological Society of America*, 50(2):253-266.

Mollard, J.D. (1977) 'Regional landslide types in Canada', in Coates, D.R. (Ed.) *Landslides: Reviews in Engineering Geology Volume III*. Boulder, Colorado: Geological Society of America, pp.29-56.

Moore, D.P. and Matthews, W.H. (1978) 'The Rubble Creek landslide, southwestern British Columbia', *Canadian Journal of Earth Sciences*, 15(7):1039-1052.

Mudge, M.R. (1965) 'Rock avalanche and rockslide avalanche deposits at Sawtooth Range, Montana', *Geological Society of America Bulletin*, 76(9):1003-1014.

Mulligan, M. and Wainwright, J. (2013) 'Modelling and Model Building', in Wainwright, J. and Mulligan, M. (Eds.) *Environmental Modelling: Finding Simplicity in Complexity*. 2nd Edn. Chichester: John Wiley & Sons, pp.7-26.

Murty, T.S. (1979) 'Submarine slide-generated water waves in Kitimat, British Columbia', *Journal of Geophysical Research: Oceans*, 84(C12):7777-7779.

Nicoletti, P.G. and Sorriso-Valvo, M. (1991) 'Geomorphic controls of the shape and mobility of rock avalanches', *Geological Society of America Bulletin*, 103(10):1365-1373.

O'Brien, J.S., Julien, P.Y. and Fullerton, W.T. (1993) 'Two-dimensional water flood and mudflow simulation', *Journal of Hydraulic Engineering*, 119(2):244-261.

Okura, Y., Kitahara, H., Kawanami, A. and Kurokawa, U. (2003) 'Topography and volume effects on travel distance of surface failure', *Engineering Geology*, 67(3-4):243-254.

Olesen, O., Blikra, L.H., Braathen, A., Dehls, J.F., Olsen, L., Rise, L., Roberts, D., Riis, F., Faleide, J.I. and Anda, E. (2004) 'Neotectonic deformation in Norway and its implications: a review', *Norwegian Journal of Geology*, 84:3-34.

Ostermann, M., Sanders, D., Ivy-Ochs, S., Alfimov, V., Rockenschaub, M. and Römer, A. (2012) 'Early Holocene (8.6 ka) rock avalanche deposits, Obernberg valley (Eastern Alps): Landform interpretation and kinematics of rapid mass movement', *Geomorphology*, 171-172:83-93.

Paris, R., Giachetti, T., Chevalier, J., Guillou, H. and Frank, N. (2011) 'Tsunami deposits in Santiago Island (Cape Verde archipelago) as possible evidence of a massive flank failure of Fogos volcano', *Sedimentary Geology*, 239(3-4):129-145.

Pedersen, S.A.S., Foged, N. and Frederiksen, J. (1989) 'Extent and economic significance of landslides in Denmark, Faroe Islands and Greenland', in Brabb, E.E. and Harrod, B.L. (Eds.) *Landslides, extent and economic significance*. Rotterdam: Balkema, pp.153-156.

Pedersen, G.K. and Pulvertaft, T.C.R. (1992) 'The nonmarine Cretaceous of the West Greenland basin, onshore West Greenland', *Cretaceous Research*, 13:263-272.

Pedersen, S.A.S., Larsen, L.M., Dahl-Jensen, T., Jepsen, H.F., Pedersen, G.K., Nielsen, T., Pedersen, A.K., Platen-Hallermund, F.V. and Weng, W. (2002) 'Tsunami-generating rock fall and landslide on the south coast of Nuussuaq, central West Greenland', *Geological Survey of Denmark and Greenland Bulletin*, 191:73-83.

Pirulli, M. (2008) 'The Thurweiser rock avalanche (Italian Alps): Description and dynamic analysis', *Engineering Geology*, 109(1):80-92.

Pirulli, M. and Mangeney, A. (2008) 'Results of back-analysis of the propagation of rock avalanches as a function of the assumed rheology', *Rock Mechanics and Rock Engineering*, 41(1):59-84.

Pirulli, M. (2009) 'The Thurwieser rock avalanche (Italian Alps): Description and dynamic analysis', *Engineering Geology*, 109:80-92.

Pirulli, M. and Pastor, M. (2012) 'Numerical study on the entrainment of bed material into rapid landslides', *Geotechnique*, 62(11):959-972.

Pitman, E.B., Nichita, C., Patra, A., Bauer, A., Bursik, M. and Weber, A. (2003) 'A model of granular flows over an erodible surface', *Discrete and Continuous Dynamical Systems – Series B*, 3(4):589-600.

Pitman, E.B. and Le, L. (2005) 'A two-fluid model for avalanche and debris flow', *Philosophical Transactions of the Royal Society A*, 363(1832):1573-1601.

Poisel, R. and Preh, A. (2007) 'Landslide detachment mechanisms: An overview of their mechanical models', in Ho., K. and Li., V. (Eds.) *Proceedings of the 2007 International Forum on Landslide Disaster Management*. Hong Kong: Hong Kong Geotechnical Engineering Office, pp.1043-1058.

Poli, D., Remondino, F., Angiuli, E. and Agugiaro, G. (In Press) 'Radiometric and geometric evaluation of GeoEye-1, WorldView-2 and Pléiades-1A stereo images for 3D information extraction', *ISPRS Journal of Photogrammetry and Remote Sensing*, DOI: 10.1016/j.isprsjprs.2014.04.007.

Ponomareva, V.V., Melekestsev, I.V. and Dirksen, O.V. (2006) 'Sector collapses and large landslides on Late Pleistocene–Holocene volcanoes in Kamchatka, Russia', *Journal of Volcanology and Geothermal Research*, 158(1):117-138.

Porter, S.C. and Orombelli, G. (1980) 'Catastrophic rockfall of September 12, 1717 on the Italian flank of the Mont Blanc massif', *Zeitschrift für Geomorphologie*, 24(2):200-218.

Post, A.S. (1967) 'Effects of the March 1964 Alaska earthquake on glaciers', *United States Geological Survey Professional Paper 544-D*, 42 p.

Prager, C., Krainer, K., Seidl, V. and Chwatal, W. (2006) 'Spatial features of Holocene struzström-deposits inferred from subsurface investigations (Fernpass rockslide, Tyrol, Austria)', *Geo.Alp*, 3:147-66.

Prudencio, M. and Van Sint Jan, M. (2007) 'Strength and failure modes of rock mass models with non-persistent joints', *International Journal of Rock Mechanics and Mining Sciences*, 44(6):890-902.

Pudasaini, S.P. and Hutter, K. (2003) 'Rapid shear flows of dry granular masses down curved and twisted channels', *Journal of Fluid Mechanics*, 495:193-208.

Pudasaini, S.P. and Domnik, B. (2009) 'Energy consideration in accelerating rapid shear granular flows', *Nonlinear Processes in Geophysics*, 16(3):399-407.

Pudasaini, S.P. (2012) 'A general two-phase debris flow model', *Journal of Geophysical Research: Earth Surface*, 117(F3):28 p.

Pudasaini, S.P. and Krautblatter, M. (In Press) 'A two-phase mechanical model for rock-ice avalanches', *Journal of Geophysical Research: Earth Surface*, DOI: 10.1002/2014JF003183.

Quantin, C., Allemand, P. and Delacourt, C. (2004) 'Morphology and geometry of Valles Marineris landslides', *Planetary and Space Science*, 52(11):1011-1022.

Rait, K.L., Bowman, E.T. and Lambert, C. (2012) 'Dynamic fragmentation of rock clasts under normal compression in stürzstrom', *Géotechnique Letters*, 2:167-172.

Raggam, H. (2006) 'Surface mapping using image triplets', *Photogrammetric Engineering and Remote Sensing*, 72(5):551-563.

Reubi, O. and Hernandez, J. (2000) 'Volcanic debris avalanche deposits of the upper Maronne valley (Cantal Volcano, France): evidence for contrasted formation and transport mechanisms', *Journal of Volcanology and Geothermal Research*, 102(3):271-286.

Revellino, P., Hungr, O., Guadagno, F.M. and Evans, S.G. (2004) 'Velocity and runout simulation of destructive debris flows and debris avalanches in pyroclastic deposits, Campania region, Italy', *Environmental Geology*, 45(3):295-311.

Reznichenko, N.V., Davies, T.R.H., Shulmeister, J. and Winkler, S. (2012a) 'Influence of rock avalanches upon the formation of moraines and their subsequent palaeoclimatic interpretation: a critical appraisal', *Zeitschrift für Geomorphologie*, 56(4):37-54.

Reznichenko, N.V., Davies, T.R.H., Shulmeister, J. and Larsen, S.H. (2012b) 'A new technique for identifying rock avalanche-sourced sediment in moraines and some palaeoclimatic implications', *Geology*, 40(4):319-322.

Rickenmann, D. and Zimmermann, M. (1993) 'The 1987 debris flows in Switzerland: documentation and analysis', *Geomorphology*, 8(2-3):175-189.

Rickenmann, D. (1999) 'Empirical relationships for debris flows', *Natural Hazards*, 19(1):47-77.

Rickenmann, D. (2005) 'Runout prediction methods', in Jakob, M. and Hungr, O. (Eds.) *Debris-flow hazards and related phenomena*. Berlin: Springer, pp.305-324.

Rignot, E. and Kanagaratnam, P. (2006) 'Changes in the velocity structure of the Greenland Ice Sheet', *Science*, 311(5763):986-990.

Rignot, E., Velicogna, I., van den Broeke, M.R., Monaghan, A. and Lenaerts, J.T.M. (2011) 'Acceleration of the contribution of the Greenland and Antarctic ice sheets due to sea level rise', *Geophysical Research Letters*, 38(L05503):5 p.

Roberts, D.H., Long, A.J., Schnabel, C., Davies, B.J., Xu, S., Simpson, M.J.R. and Huybrechts, P. (2009) 'Ice sheet extent and early deglacial history of the southwestern sector of the Greenland Ice Sheet', *Quaternary Science Reviews*, 28(25-26):2760-2773.

Sassa, K., Fukuoka, H., Wang, F.W. and Evans, S.G. (1998) 'Sliding surface liquefaction and undrained loading mechanism in rapid landslides in Japan and Canada', *Panel Report for 8th Congress of the International Association for Engineering Geology, Volume 3*. Rotterdam: Balkema, pp.1923-1930.

Savage, S.B. and Hutter, K. (1989) 'The motion of a finite mass of granular material down a rough incline', *Journal of Fluid Mechanics*, 199:177-215.

Scheidegger, A.E. (1973) 'On the prediction of the reach and velocity of catastrophic landslides', *Rock mechanics*, 5(4):231-236.

Scheidegger, A.E. (1998) 'Tectonic predesign of mass movements, with examples from the Chinese Himalaya', *Geomorphology*, 26(1-3):37-46.

Scheidl, C., Rickenmann, D. and McArdell, B.W. (2013) 'Runout prediction of debris flows and similar mass movements', in Margottini, C., Canuti, P. and Sassa, K. (Eds.) *Landslide Science and Practice, Volume 3: Spatial Analysis and Modelling*. Berlin: Springer, pp.221-229.

Schneider, D., Bartelt, P., Caplan-Auerbach, J., Christen, M., Huggel, C. and McArdell, B.W. (2010) 'Insights into rock-ice avalanche dynamics by combined analysis of seismic recordings and a numerical avalanche model', *Journal of Geophysical Research: Earth Surface*, 115(F4):20 p.

Schneider, D., Huggel, C., Haeberli, W. and Kaitna, R. (2011) 'Unravelling driving factors for large rock-ice avalanche mobility', *Earth Surface Processes and Landforms*, 36(14):1948-1966.

Schwab, J.W., Geertsema, M. and Evans, S.G. (2003) 'Catastrophic rock avalanches, west-central B.C., Canada', *Proceedings of the 3rd Canadian Conference on Geotechnique and Natural Hazards*. Edmonton: The Canadian Geotechnical Society, pp.252-259.

Schwaiger, H.F. (2008) 'Smoothed Particle Hydrodynamics simulations of cavity generation/collapse and resulting wave heights from the impact of tsunamigenic, subaerial landslides', *AGU Fall Meeting Abstracts*, 1:0961.

Sepúlveda, S. and Serey, A. (2009) 'Tsunamigenic, earthquake-triggered rock slope failures during the April 21, 2007 Aisén earthquake, southern Chile (45.5°S)', *Andean Geology*, 36(1):131-136.

Shea, T., de Vries, B.V.W. and Pilato, M. (2008) 'Emplacement mechanisms of contrasting debris avalanches at Volcán Mombacho (Nicaragua), provided by structural and facies analysis', *Bulletin of Volcanology*, 70(8):899-921.

Sheridan, M.F., Stinton, A.J., Patra, A., Pitman, E.B., Bauer, A. and Nichita, C.C. (2005) 'Evaluating Titan 2D mass-flow model using the 1963 Little Tahoma Peak avalanches, Mount Rainier, Washington', *Journal of Volcanology and Geothermal Research*, 139:89-102.

Shreve, R.L. (1968) 'The Blackhawk Landslide', *Geological Society of America Special Papers*, 108:1-48.

Shugar, D.H., Clague, J.J. and Giardino, M. (2013) 'A quantitative assessment of the sedimentology and geomorphology of rock avalanche deposits', in Margottini, C., Canuti, P. and Sassa, K. (Eds.) *Landslide Science and Practice, Volume 3: Spatial Analysis and Modelling*. Berlin: Springer, pp.321-326.

Shulmeister, J., Davies, T.R.H., Evans, D.J.A., Hyatt, O.M. and Tovar, D.S. (2009) 'Catastrophic landslides, glacier behaviour and moraine formation – A view from an active plate margin', *Quaternary Science Reviews*, 28(11-12):1085-1096.

Siebe, C., Komorowski, J.C. and Sheridan, M.F. (1992) 'Morphology and emplacement collapse of an unusual debris-avalanche deposit at Jocotitlán Volcano, Central Mexico', *Bulletin of Volcanology*, 54(7):573-589.

Siebert, L. (1984) 'Large volcanic debris avalanches: characteristics of source areas, deposits and associated eruptions', *Journal of Volcanology and Geothermal Research*, 22(3-4):163-197.

Siebert, L., Glicken, H. and Ui, T. (1987) 'Volcanic hazards from Bezymianny- and Bandai-type eruptions', *Bulletin of Volcanology*, 49(1):435-459.

Simpson, M.J.R., Milne, G.A., Huybrechts, P. and Long, A.J. (2009) 'Calibrating a glaciological

model of the Greenland ice sheet from the Last Glacial Maximum to present-day using field observations of relative sea level and ice extent', *Quaternary Science Reviews*, 28(17-18):1631-1657.

Smelror, M., Ahlstrom, A., Ekelund, L., Hansen, J.M., Nenonen, K. and Mortensen, A.K. (2008) 'The Nordic geological surveys: Geology for society in practice', *Episodes*, 31(1):193-200.

Smith, G.M., Davies, T.R.H., McSaveney, M.J. and Bell, D.H. (2006) 'The Acheron rock avalanche, Canterbury, New Zealand - morphology and dynamics', *Landslides*, 3(1):62-72.

Sørensen, S.A. and Bauer, B. (2003) 'On the dynamics of the Köfels stürzstrom', *Geomorphology*, 54(1):11-19.

Sosio, R., Crosta, G.B. and Hungr, O. (2008) 'Complete dynamic modeling calibration for the Thurwieser rock avalanche (Italian Central Alps)', *Engineering Geology*, 100(1):11-26.

Sosio, R., Crosta, G.B., Chen, J.H. and Hungr, O. (2012) 'Modelling rock avalanche propagation onto glaciers', *Quaternary Science Reviews*, 47:23-40.

Spotila, J.A., Buscher, J.T., Meigs, A.J. and Reiners, P.W. (2004) 'Long-term glacial erosion of active mountain belts; example of the Chugach-St. Elias Range, Alaska', *Geology*, 32(6):501-504.

Špůrek, M. (1974) 'Sesuvne jevy u Dřinova na Mostecku', *Věstnik Ustředniho ustavu geologickeho*, 49:231-234.

Stoopes, G.R. and Sheridan, M.F. (1992) 'Giant debris avalanches from the Colima Volcanic Complex, Mexico: Implications for long-runout landslides (>100 km) and hazard assessment', Geology, 20(4):299-302.

Strahler, A.N. (1964) 'Quantitative geomorphology of drainage basins and channel networks', in Chow, V.T. (Ed.) *Handbook of Applied Hydrology*. New York: McGraw Hill, pp.439-476.

Straub, S. (1997) 'Predictability of long runout landslide motion: implications from granular flow mechanics', *Geologische Rundschau*, 86(2):415-425.

Strom, A.L. (1999) 'Giant ancient rock slides and rock avalanches in the Tien Shan Mountains, Kyrgyzstan', *Landslide News*, 11:20-23.

Strom, A.L. (2004) 'Rock avalanches of the Ardon River valley at the southern foot of the Rocky Range, Northern Caucasus, North Osetia', *Landslides*, 1(3):237-241.

Strom, A.L. and Korup, O. (2006) 'Extremely large rockslides and rock avalanches in the Tien Shan Mountains, Kyrgyzstan'. *Landslides*, 3(2):125-136.

Suckro, S.K., Gohl, K., Funck, T., Heyde, I., Schreckenberger, B., Gerlings, J. and Damm, V. (2013) 'The Davis Strait crust – a transform margin between two oceanic basins', *Geophysical International Journal*, 193(1):78-97.

Suriñach, E., I. Vilajosana, G. Khazaradze, B. Biescas, G. Furdada, and J. M. Vilaplana (2005) 'Seismic detection and characterization of landslides and other mass movements', *Natural Hazards and Earth System Sciences*, 5(6):791-798.

Szczuciński, W., Rosser, N.J., Strzelecki, M.C., Long, A.J., Lawrence, T., Buchwal, A., Chague-Goff, C. and Woodroffe, S. (2012) 'Sedimentary record and morphological effects of a landslide-generated tsunami in a Polar region: The AD 2000 tsunami in Vaigat Strait, West Greenland', *American Geophysical Union, Fall Meeting 2012*, Abstract #OS33B-1820.

Takahashi, T. and Tsujimoto, H. (2000) 'A mechanical model for Merapi-type pyroclastic flow', *Journal of Volcanology and Geothermal Research*, 98(1-4):91-115.

Takahashi, T (2001) 'Mechanism and simulation of snow avalanches, pyroclastic flows and debris

flows', in McCaffrey, W., Kneller, B. and Peakall, J. (Eds.) *Particulate Gravity Currents.* Oxford: Blackwell, pp.9-43.

Tappin, D.R., Watts, P. and Grilli, S.T. (2008) 'The Papua New Guinea tsunami of 17 July 1998: anatomy of a catastrophic event', *Natural Hazards and Earth System Science*, 8(2):243-266.

Toro, E.F. (2001) *Shock-Capturing Methods for Free-Surface Shallow Flows*. New Jersey: John Wiley & Sons, 309 p.

Travelletti, J., Demand, J., Jaboyedoff, M. and Marillier, F. (2010) 'Mass movement characterization using a reflexion and refraction seismic survey with the sloping local base level concept', *Geomorphology*, 116(1):1-10.

Ui, T., Takarada, S. and Yoshimoto, M. (2000) 'Debris avalanches' in Sigurdsson, H., Houghton, B., McNutt, S.R., Rymer, H. and Stix, J. (Eds.) *Encyclopaedia of Volcanoes*. London: Academic Press, pp.617-626.

Vallance, J.W., Siebert, L., Rose Jr, W.I., Girón, J. R. and Banks, N.G. (1995) 'Edifice collapse and related hazards in Guatemala', *Journal of Volcanology and Geothermal Research*, 66(1):337-355.

van Westen, C.J., van Asch, T.W.J. and Soeters, R. (2005) 'Landslide hazard and risk zonation; why is it still so difficult?', *Bulletin of Engineering Geology and the Environment*, 65(2):167-184.

Voellmy, A. (1955) 'Über die Zerstorunskraft von Lawinen (On breaking force of avalanches)', *Schweizerische Bauzeitung*, 73:212-285.

Voight, B. and Faust, C. (1982) 'Frictional heat and strength loss in some rapid landslides', *Géotechnique*, 32(1):43-54.

Voight, B., Janda, R.J., Glicken, H. and Douglass, P.M. (1983) 'Nature and mechanics of the Mount St. Helens rockslide-avalanche of 18 May 1980', *Géotechnique*, 33(3):243-273.

Voight, B. and Sousa, J. (1994) 'Lessons from Ontake-San: a comparative analysis of debris avalanche dynamics', *Engineering Geology*, 38(3-4):261-297.

Völker, D., Scholz, F. and Geersen, J. (2011) 'Analysis of submarine landsliding in the rupture area of the 27 February 2010 Maule earthquake, Central Chile', *Marine Geology*, 288(1):79-89.

von Poschinger, A., Wassmer, P. and Maisch, M. (2006) 'The Flims rockslide: History of interpretation and new insights', in Evans, S.G., Mugnozza, G.S., Strom, A. and Hermanns, R.L. (Eds.) *Landslides from Massive Rock Slope Failure. Proceedings of the NATO Advanced Research Workshop on Massive Rock Slope Failure: New Models for Hazard Assessment, Celano, Italy, 16-21 June 2002*. Netherlands: Springer, pp.329-356.

Voss, P., Poulsen, S.K., Simonsen, S.B. and Gregersen, S. (2007) 'Seismic hazard assessment of Greenland', *Geological Survey of Denmark and Greenland Bulletin*, 13:57-60.

Wadge, G., Jackson, P., Bower, S.M., Woods, A.W. and Calder, E. (1998) 'Computer simulations of pyroclastic flows from dome collapse', *Geophysical Research Letters*, 25(19):3677-3680.

Wassmer, P., Schneider, J.L., Pollet, N. and Schmitter-Voirin, C. (2004) 'Effects of the internal structure of a rock-avalanche dam on the drainage mechanism of its impoundment, Flims stürzstrom and Ilanz paleo-lake, Swiss Alps', *Geomorphology*, 61(1-2):3-17.

Weidick, A. and Bennike, O. (2007) 'Quaternary glaciation history and glaciology of Jakobshavn Isbræ and the Disko Bugt region, West Greenland: a review', *Geological Survey of Denmark and Greenland Bulletin*, 14:78 p.

Weidinger, J.T. and Korup, O. (2009) 'Frictionite as evidence for a large Late Quaternary

rockslide near Kanchenjunga, Sikkim Himalayas, India – implications for extreme events in mountain relief destruction', *Geomorphology*, 103(1):57-65.

Weidinger, J.T., Korup, O., Munack, H., Altenberger, U., Dunning, S.A., Tippelt, G. and Lottermoser, W. (2014) 'Giant rockslides from the inside', *Earth and Planetary Science Letters*, 389:62-73.

Weiss, R., Fritz, H.M. and Wunnemann, K. (2009) 'Hybrid modeling of the mega-tsunami runup in Lituya Bay after half a century', *Geophysical Research Letters*, 36(9):L09602.

Whitehouse, I.E. (1983) 'Distribution of large rock avalanche deposits in the central Southern Alps, New Zealand', *New Zealand Journal of Geology and Geophysics*, 26(3):271-279.

Whitehouse, I.E. and Griffiths, G.A. (1983) 'Frequency and hazard of large rock avalanches in the central Southern Alps, New Zealand', *Geology*, 11(6):331-334.

Wieczorek, G.F. (1996) 'Landslide triggering mechanisms', in Turner, A.K. and Schuster, R.L. (Eds.) *Landslides: Investigation and Mitigation*. Washington: National Academy Press, pp.76-90.

Wieczorek, G.F. (2002) 'Catastrophic rockfalls and rockslides in the Sierra Nevada, USA', in Evans, S.G. and DeGraff, J.V. (Eds.) *Catastrophic landslides: effects, occurrence and mechanisms, Reviews in Engineering Geology Volume XV*. Boulder, Colorado: Geological Society of America. pp.165-190.

Willenberg, H., Eberhardt, E., Loew, S., McDougall, S. and Hungr, O. (2009) 'Hazard assessment and runout analysis for an unstable rock slope above an industrial site in the Riviera valley, Switzerland', *Landslides*, 6(2):111-116.

Willgoose, G. and Hancock, G. (1998) 'Revisiting the hypsometric curve as an indicator of form and process in transport-limited catchments', *Earth Surface Processes and Landforms*, 23(7):611-623.

Wright, C.A. (1998) 'The AD 930 long-runout Round Top debris avalanche, Westland, New Zealand', *New Zealand Journal of Geology and Geophysics*, 41(4):493-497.

Yarnold, J.C. and Lombard, J.P. (1989) 'Litho-kinematic facies model for large landslide deposits in arid settings', *Bulletin of the American Association of Petroleum Geologists*, 73:554-555.

Yarnold, J.C. (1993) 'Rock-avalanche characteristics in dry climates and the effect of flow into lakes: Insights from the mid-Tertiary sedimentary breccias near Artillery Peak, Arizona', *Geological Society of America Bulletin*, 105(3):345-360.

Appendices

Appendix A

Rock avalanche database

The database given here has been compiled from a literature review of 258 rock avalanche events. Only events with estimates for failure volume, vertical drop height and run-out are included.

Subaerial, non-volcanic landslides and rock avalanches					
Event	Volume (x10⁶ m³)	Height (H; m)	Run-out (L; m)	H/L (-)	Reference
Acheron R.	6	550	2,000	0.28	Whitehouse (1983)
Airolo	1	-	-	0.64	Heim (1932)
Aksu	1,500	1,900	4,600	0.41	Strom and Korup (2006)
Allan 4	23	1,300	7,700	0.17	Nicoletti and Sorriso-Valvo (1991)
Allen 4	23	1,300	7,700	0.17	Nicoletti and Sorriso-Valvo (1991)
Antronapiana	12	1,650	4,190	0.39	Nicoletti and Sorriso-Valvo (1991)
Antronapiana	12	1,650	4,190	0.39	Nicoletti and Sorriso-Valvo (1991)
Ashburton R. (North Br.)	11	600	1,800	0.33	Whitehouse (1983)
Ashburton R. (North Br.)	1	200	500	0.40	Whitehouse (1983)
Ashburton R. (South Br.)	7	700	900	0.78	Whitehouse (1983)
Bering 2	12	-	6,500	0.39	Schneider *et al.* (2011)
Bering 3	7	-	5,400	0.37	Schneider *et al.* (2011)
Beshkiol	10,000	2,500	10,500	0.24	Strom and Korup (2006)
Blackhawk	283	1,100	9,860	0.11	Shreve (1968)
Boulder B	152	400	4,000	0.10	Hermanns and Strecker (1999)
Brealito	30	700	2,250	0.31	Hermanns and Strecker (1999)
Broken R. (Leith Hill)	4	350	1,300	0.27	Whitehouse (1983)
Casa de los Loros II	163	1,100	3,500	0.31	Hermanns and Strecker (1999)
Cerro Paranilla I	23	500	2,200	0.23	Hermanns and Strecker (1999)
Cerro Paranilla II	32	700	3,100	0.23	Hermanns and Strecker (1999)
Chisca	1	-	1,500	0.24	Geertsema *et al.* (2006)
Chukurchak	1,000	1,200	7,500	0.16	Strom and Korup (2006)
Claps de Luc	2	370	800	0.46	Scheidegger (1973)
Clyde R.	10	500	1,900	0.26	Whitehouse (1983)
Clye R. (McCoy Stm)	15	500	600	0.83	Whitehouse (1983)
Constantino	20	940	2,240	0.42	Guerricchio and Melidoro (1973)
Corno di Dosté	20	1,200	3,700	0.32	Heim (1932)
Craigieburn Rg.	500	1,200	2,700	0.44	Whitehouse (1983)
Damocles	27	550	3,400	0.16	Nicoletti and Sorriso-Valvo (1991)
Damocles	27	550	3,400	0.16	Eisbacher (1979)

Dead Lakes	2,500	1,800	7,700	0.23	Strom and Korup (2006)
Diablerets	30	1,200	5,500	0.22	Heim (1932)
Diablerets	30	1,200	5,500	0.22	Eisbacher and Clague (1984)
Disentis	20	740	2,100	0.35	Heim (1932)
Djamantau	1,000	1,300	6,000	0.22	Strom and Korup (2006)
Dřínov	19	410	1,560	0.26	Špůrek (1974)
Dřínov	19	410	1,560	0.26	Nicoletti and Sorriso-Valvo (1991)
Dulung Bar-Darkot	400	1,900	8,200	0.23	Hewitt (2006)
Dusty Creek	7	970	2,490	0.39	Clague and Souther (1982)
El Capitan	40	1,300	6,800	0.19	Yarnold and Lombard (1989)
El Paso I	210	1,100	4,750	0.23	Hermanns and Strecker (1999)
El Paso II	225	700	2,850	0.25	Hermanns and Strecker (1999)
Elm	11	600	2,300	0.26	Heim (1932)
Engelberg	2,500	1,600	7,400	0.22	Scheidegger (1973)
Eperon de la Brenva	6	-	5,500	0.39	Deline (2001)
Fairweather	26	3,300	10,000	0.33	Post (1967)
Flims	12,000	2,000	15,600	0.13	Scheidegger (1973)
Frank	37	800	3,290	0.24	Daly *et al.* (1912)
Ghoro Choh I	60	1,300	7,000	0.19	Hewitt (1999)
Glärnisch	800	1,900	7,500	0.25	Heim (1932)
Goldau	40	1,120	6,100	0.18	Heim (1932)
Gros Ventre	38	660	4,350	0.15	Alden (1928)
Harper R. (Cass Sd)	2	500	850	0.59	Whitehouse (1983)
Hope BC	47	1,220	4,240	0.29	Matthews and McTaggart (1969)
Huascarán (1962)	13	3,600	15,520	0.23	Nicoletti and Sorriso-Valvo (1991)
Huascarán (1970)	75	3,850	15,600	0.25	Nicoletti and Sorriso-Valvo (1991)
Jonas Creek (N)	2	880	3,250	0.27	Scheidegger (1973)
Jonas Creek (S)	5	920	2,500	0.37	Scheidegger (1973)
Kandertal	140	1,900	9,900	0.19	Heim (1932)
Karakudjur	10,000	1,600	6,000	0.27	Strom and Korup (2006)
Katzarah	120	2,400	11,000	0.22	Hewitt (1999)
Khait	75	1,421	7,410	0.19	Evans *et al.* (2009)
Köfels	2,500	800	2,500	0.32	Sørensen and Bauer (2003)
Kokmeren	1,000	1,800	4,500	0.40	Strom and Korup (2006)
Kugart	2,500	700	7,750	0.09	Strom and Korup (2006)
Kuzulu	13	950	3,300	0.29	Scheidegger (1973)
La Madeleine	71	1,561	4,500	0.35	Scheidegger (1973)
Lavini di Marco	200	1,170	5,650	0.21	Nicoletti and Sorriso-Valvo (1991)
Lavini di Marco	200	1,170	5,650	0.21	Fuganti (1969)
Lawrence R.	3	600	2,700	0.22	Whitehouse (1983)
Lawrence R.	6	900	2,000	0.45	Whitehouse (1983)
Lecco	0	-	-	0.88	Heim (1932)
Little Tahoma Pk	11	-	-	0.29	Crandell and Fahnestock (1965)
Loma d. Aspereza	62	1,000	7,000	0.14	Hermanns and Strecker (1999)
Loma Redonda	65	1,000	7,000	0.14	Hermanns and Strecker (1999)
Luzon	20	810	3,800	0.21	Nicoletti and Sorriso-Valvo (1991)
Madison Canyon	29	430	1,680	0.26	Hadley (1959)

Maligne Lake	667	980	5,470	0.18	Mollard (1977)
Martin River 2	12	-	4,000	0.28	Sosio *et al.* (2012)
Martin River 3	9	-	5,000	0.28	Sosio *et al.* (2012)
Martin River 4	11	-	5,900	0.40	Sosio *et al.* (2012)
Martin River 5	4	-	3,700	0.32	Sosio *et al.* (2012)
Martinez Mountain	380	1,850	8,560	0.22	Baldwin (1987)
Mathias R. (Boundary Ck)	280	900	1,300	0.69	Whitehouse (1983)
Mayunmarca	1,600	1,800	8,000	0.23	Kojan and Hutchinson (1978)
Medicine Lake	86	320	1,220	0.26	Scheidegger (1973)
Mombiel	1	370	800	0.46	Scheidegger (1973)
Mont Granier	210	1,520	7,690	0.20	Eisbacher and Clague (1984)
Monte Zandilla	40	1,390	3,950	0.35	Nicoletti and Sorriso-Valvo (1991)
Mosque Mountain	5	-	1,200	0.42	Lu (2003)
Mount Cayley	1	1,180	3,460	0.34	Nicoletti and Sorriso-Valvo (1991)
Mystery Creek	35	1,250	4,000	0.31	Eisbacher (1983)
Nomash River	0	560	2,270	0.25	Nicoletti and Sorriso-Valvo (1991)
North Long John	25	1,338	1,560	0.86	Blair (1999)
Nozzle	67	1,050	6,420	0.16	Eisbacher (1979)
Obersee	120	1,800	5,000	0.36	Heim (1932)
Pamir	2,000	1,500	6,200	0.24	Scheidegger (1973)
Parpan	500	1,340	6,550	0.20	Abele (1974)
Pink Mountain	1	450	1,950	0.23	Nicoletti and Sorriso-Valvo (1991)
Poschiavo	150	1,500	4,100	0.37	Heim (1932)
Poulter R (Casey Hut)	23	900	1,600	0.56	Whitehouse (1983)
Poulter R (Mt Binser)	5	400	2,000	0.20	Whitehouse (1983)
Poulter R (Thompson Stm)	5	500	800	0.63	Whitehouse (1983)
Punta Thurweiser	3	-	2,900	0.48	Schneider *et al.* (2011)
Queen Elizabeth	45	950	2,645	0.36	Nicoletti and Sorriso-Valvo (1991)
Rangitata R. (Bush Stm)	99	500	3,200	0.16	Whitehouse (1983)
Rangitata R. (Forest Ck)	7	500	1,200	0.42	Whitehouse (1983)
Rangitata R. (L. Camp)	2	300	900	0.33	Whitehouse (1983)
Rangitata R. (Pudding Val.)	10	600	1,400	0.43	Whitehouse (1983)
Rincón Ruins I	49	800	5,500	0.15	Hermanns and Strecker (1999)
Rockslide Pass	493	1,000	6,330	0.16	McLellan and Kaiser (1984)
Round Top	45	570	4,800	0.12	Wright (1998)
Rubble Creek	33	1,040	6,900	0.15	Moore and Matthews (1978)
Saidmarreh	38,000	1,500	18,900	0.08	Scheidegger (1973)
Sarychelek	2,500	1,700	6,250	0.27	Strom and Korup (2006)
Sasso Englar	13	370	1,680	0.22	Nicoletti and Sorriso-Valvo (1991)
Sasso Englar	13	370	1,680	0.22	Fuganti (1969)
Satpura	300	1,700	9,000	0.19	Hewitt (1999)
Schächental	1	1,800	3,100	0.58	Heim (1932)
Schwan	27	1,550	6,100	0.25	Post (1967)
Scimada Saoseo	80	1,500	5,500	0.27	Heim (1932)
Sherman	13	1,080	5,950	0.18	Shreve (1966)
Sierra Carahuasi I	143	700	3,750	0.19	Hermanns and Strecker (1999)
Sierra Carahuasi II	54	700	3,100	0.23	Hermanns and Strecker (1999)
Sierra Laguna Blanca VIII	264	1,600	15,000	0.11	Hermanns and Strecker (1999)

Silver Reef	227	760	6,670	0.11	Shreve (1968)
Stalk Lakes	53	700	3,000	0.23	Mollard (1977)
Steller I	20	1,200	6,700	0.18	Post (1967)
Taipo R. (Hunts Ck)	35	650	1,750	0.37	Whitehouse (1983)
Tamins	1,300	1,300	13,500	0.10	Scheidegger (1973)
Taramakau R. (Otehake R.)	57	500	3,200	0.16	Whitehouse (1983)
Tonco Syncline I	70	650	2,300	0.28	Hermanns and Strecker (1999)
Triple Slide	47	550	3,970	0.14	Eisbacher (1979)
Turnoff Creek	4	-	2,000	0.28	Geertsema *et al.* (2006)
Twin Slide (I)	7	900	4,670	0.19	Eisbacher (1978)
Twin Slide (II)	7	820	4,400	0.19	Eisbacher (1978)
Vaiont	250	500	1,500	0.33	Müller (1968)
Val Lagone	1	1,050	2,400	0.44	Heim (1932)
Val Pola	40	1,200	1,500	0.80	Crosta *et al.* (2004)
Verney - Bishop's Bay	1	-	1,100	0.59	Geertsema *et al.* (2006)
Villa Vil I	184	300	2,500	0.12	Hermanns and Strecker (1999)
Villa Vil II	247	350	2,250	0.16	Hermanns and Strecker (1999)
Villa Vil III	375	400	2,500	0.16	Hermanns and Strecker (1999)
Villa Vil IV	243	400	2,750	0.15	Hermanns and Strecker (1999)
Villa Vil V	34	400	1,500	0.27	Hermanns and Strecker (1999)
Villa Vil VI	15	250	1,000	0.25	Hermanns and Strecker (1999)
Voralpsee	30	1,100	3,400	0.32	Heim (1932)
Waimakariri R. (Hawdon Stm)	12	600	1,000	0.60	Whitehouse (1983)
Waimakariri R. (Mt Binser)	40	400	1,800	0.22	Whitehouse (1983)
Wengen	6	590	1,400	0.42	Altmann (1959)
Wengen S	3	500	1,100	0.45	Altmann (1959)
Wilberforce R.	9	650	800	0.81	Whitehouse (1983)
Zarzo I	37	900	6,500	0.14	Hermanns and Strecker (1999)
Zarzo II	15	650	4,000	0.16	Hermanns and Strecker (1999)
Zymoetz	1	1,245	4,200	0.30	Boultbee *et al.* (2006)

Rock avalanches onto glaciers					
Event	**Volume (x10⁶ m³)**	**Height (H; m)**	**Run-out (L; m)**	**H/L (-)**	**Reference**
Black Rapids Glacier (W)	6	730	3,400	0.21	Shugar *et al.* (2013)
Devastation Glacier	13	1,190	7,000	0.17	Nicoletti and Sorriso-Valvo (1991)
Howson II	2	1,296	2,700	0.48	Schwab *et al.* (2003)
Illiamna - Red Glacier	17	-	8,600	0.23	Huggel (2007)
Kendall Glacier	0	204	1,200	0.17	Evans and Couture (2002)
Kshwan Glacier	3	675	2,205	0.31	Mauthner (1995)
Mount Meager	1	1,340	3,700	0.36	Jiskoot (2011)
Mount Munday	3	875	4,700	0.19	Jiskoot (2011)
Mt Steele	80	1,860	5,760	0.32	Jiskoot (2011)
North Creek	2	745	2,800	0.27	Evans and Clague (1999)
Pandemonium Creek Glacier	7	2,000	8,600	0.23	Jiskoot (2011)
Tim Williams Glacier	3	935	3,700	0.25	Jiskoot (2011)
Triolet Glacier	18	1,860	6,900	0.27	Porter and Orombelli (1980)
Tsar Mountain	3	615	2,230	0.28	Jiskoot (2011)

Subaerial volcanic rock avalanches					
Event	**Volume** **(x10⁶ m³)**	**Height** **(H; m)**	**Run-out** **(L; m)**	**H/L** **(-)**	**Reference**
Akagi	4,000	2,400	19,000	0.13	Siebert (1984)
Allan Hills	1,800	500	10,000	0.05	Ui (2000)
Allan Hills	2,000	1,800	20,000	0.09	Ui (2000)
Allan Hills	18,000	3,000	30,000	0.10	Ponomareva *et al.* (2006)
Asakusa	40	1,000	6,500	0.15	Hayashi and Self (1992)
Asama	2,000	1,800	20,000	0.09	Hayashi and Self (1992)
Bakening	450	1,800	12,000	0.15	Ponomareva *et al.* (2006)
Banáhao	5,000	1,700	26,000	0.07	Geronimo-Catane (1994)
Bandai-san 1888	1,500	1,200	11,000	0.11	Hayashi and Self (1992)
Bezymianni	800	2,400	18,000	0.13	Hayashi and Self (1992)
Bezymianny	800	2,500	17,500	0.14	Ui (2000)
Callaqui	150	3,100	15,000	0.21	Siebert *et al.* (1987)
Cantal	1,000	3,500	30,000	0.12	Reubi and Hernandez (2000)
Chaos Crags	150	650	5,000	0.13	Ui (2000)
Chimborazo	8,100	3,600	35,000	0.10	Siebert (1984)
Chokai	1,800	4,000	85,000	0.05	Ui (2000)
Chokai	10,000	4,100	70,000	0.06	Luhr and Prestegaard (1988)
Chokai	3,500	2,200	25,000	0.09	Hayashi and Self (1992)
Colima	12,500	4,000	40,000	0.10	Hayashi and Self (1992)
Dikii Greben'	2,250	900	8,000	0.11	Ponomareva (2006)
Dikii Greben'	400	1,500	14,000	0.11	Ui (2000)
Egmont (Opua)	350	2,500	27,000	0.09	Hayashi and Self (1992)
Egmont (Pungarehu)	7,500	2,600	31,000	0.08	Hayashi and Self (1992)
Fuji	1,800	2,500	24,000	0.10	Hayashi and Self (1992)
Galunggung	2,900	1,900	25,000	0.08	Hayashi and Self (1992)
Iliinsky (Ilynsky)	10,000	1,800	15,000	0.12	Ponomareva (2006)
Iriga	1,500	1,050	11,000	0.10	Siebert (1984)
Ivao Group	1,000	1,400	6,600	0.21	Belousov and Belousova (2007)
Iwaki	1,300	1,600	14,000	0.11	Hayashi and Self (1992)
Jocotitlán	2,800	1,150	12,000	0.10	Siebe *et al.* (1992)
Kamen	5,000	4,400	30,000	0.15	Ponomareva (2006)
Kharimkotan (Harimkotan)	400	1,200	7,000	0.17	Belousova and Belousov (1995)
Kharimkotan (Harimkotan)	400	1,200	7,000	0.17	Belousova and Belousov (1995)
Kharimkotan (Harimkotan)	400	1,200	7,000	0.17	Belousova and Belousov (1995)
Komagatake	1,100	1,200	15,000	0.08	Ui (2000)
Komagatake	250	1,000	11,500	0.09	Hayashi and Self (1992)
Kozel'sky	750	2,000	10,000	0.20	Ponomareva (2006)
Kurohime	120	800	6,000	0.13	Siebert (1984)
Mageik	90	800	9,000	0.09	Hayashi and Self (1992)
Mawenzi	7,100	4,500	60,000	0.08	Siebert (1984)
Meru	15,000	3,900	50,000	0.08	Siebert (1984)
Mombacho	1,200	1,345	11,900	0.11	Shea *et al.* (2008)
Mombacho	1,880	1,500	12,400	0.12	Shea *et al.* (2008)
Monbacho	1,000	1,300	12,000	0.11	Hayashi and Self (1992)
Mt. St. Helens (1980)	2,500	2,550	24,000	0.11	Hayashi and Self (1992)
Mt. St. Helens (20 ka)	1,000	1,750	16,000	0.11	Siebert (1984)

Mutnovsky	500	2,000	10,000	0.20	Ponomareva *et al.* (2006)
Myoko (Sekikawa)	800	2,000	19,000	0.11	Siebert (1984)
Myoko (Taguchi)	230	1,400	8,000	0.18	Siebert (1985)
Nevado de Colima	27,000	4,800	120,000	0.04	Stoopes and Sheridan (1992)
Nevado de Toluca I	2,000	2,200	55,000	0.05	Capra *et al.* (2002)
Ontake (Ontake San)	340	1,550	12,900	0.12	Voight and Sousa (1994)
Orizaba, Pico de (Citlaltépetl)	20,000	4,750	95,000	0.05	Capra *et al.* (2002)
Orizaba, Pico de (Citlaltépetl)	1,800	4,130	85,000	0.05	Capra *et al.* (2002)
Pacaya	650	2,500	25,000	0.10	Vallance *et al.* (1995)
Pallas	1,000	900	4,800	0.19	Belousova and Belousov (1995)
Papandayan	140	1,500	11,000	0.14	Ui (2000)
Parinacota	6,000	1,900	22,000	0.09	Francis and Wells (1988)
Peleroa	16,000	3,900	85,000	0.05	Siebert *et al.* (1987)
Peteroa	16,000	3,900	85,000	0.05	Hayashi and Self (1992)
Pico de Orizaba II	1,800	3,400	85,000	0.06	Carrasco-Núñez *et al.* (1993)
Popa	800	1,200	11,000	0.11	Hayashi and Self (1992)
Popocatépetl	28,000	4,000	33,000	0.12	Capra *et al.* (2002)
Roque Nublo	14,000	3,360	28,750	0.12	Mehl and Schmincke (1999)
Shasta	26,000	3,550	50,000	0.07	Ui (2000)
Shiveluch	1,500	2,000	12,000	0.17	Hayashi and Self (1992)
Shiveluch	2,000	2,100	21,000	0.10	Ponomareva (2006)
Shiveluch	1,200	2,600	20,000	0.13	Ponomareva (2006)
Shiveluch	3,000	2,850	24,000	0.12	Ponomareva (2006)
Shiveluch	1,000	2,250	15,000	0.15	Ponomareva (2006)
Shiveluch	1,500	2,550	16,000	0.16	Ponomareva (2006)
Shiveluch	1,500	2,550	17,000	0.15	Ponomareva (2006)
Shiveluch	10,000	3,300	40,000	0.08	Ponomareva (2006)
Sierra Velluda	500	3,400	25,000	0.14	Siebert *et al.* (1987)
Socompa	17,000	3,250	35,000	0.09	Hayashi and Self (1992)
Soufriere Guadeloupe	500	1,350	9,500	0.14	Siebert (1984)
Tashiro	550	700	8,800	0.08	Ui *et al.* (2000)
Tateshina	350	1,400	12,500	0.11	Hayashi and Self (1992)
Taunshitz	400	1,600	19,000	0.08	Belousova and Belousov (1995)
Taunshitz	700	1,600	25,000	0.06	Belousova and Belousov (1995)
Tongariro	500	1,200	15,000	0.08	Lecointre *et al.* (2002)
Unzen	340	850	6,500	0.13	Siebert (1984)
Usu	300	500	6,500	0.08	Ui (2000)
Volcan de Colima	8,000	1,720	43,000	0.09	Luhr and Prestegaard (1988)
Yatsugatake (Nirasaki)	9,000	2,400	32,000	0.08	Hayashi and Self (1992)
Yatsuhatake (Otsukigawa)	270	1,400	12,500	0.11	Hayashi and Self (1992)
Zempoala	4,000	3,200	80,000	0.04	Capra *et al.* (2002)

Appendix B

VolcFlow: Model details and numerical scheme

Numerical scheme

The governing momentum equations are solved using a shock-capturing, finite difference numerical method based on a single (more stable) or double (more accurate) upwind Eulerian scheme, as defined by the user. This scheme is able to handle shocks, granular jumps and rarefaction waves, implying that the model is highly stable even when simulating rapid mass movements across complex topographies and on numerically 'wet' or 'dry' surfaces (Toro, 2001). Using this scheme, scalars (flow depth, h and elevation, z) are defined and computed at the centre of each cell while vectors (fluxes of mass and momentum, and velocities, u and v) are at the edge of each cell. Mean values of h are computed at the edges of the cells, and mean values of u and v at the centres of cells. The source terms of the mass conservation equations are computed, followed by the advection terms, at every time step. The three acceleration source terms are:

$$a_w = (-g \sin \theta_z \sin \alpha , -g \cos \theta_z \sin \alpha) \tag{1}$$

$$a_p = \left(-gk_{actpass} \cos \alpha \frac{dh}{dx}, -gk_{actpass} \cos \alpha \frac{dh}{dy}\right) \tag{2}$$

$$a_r = \left(-\frac{\tau}{\rho h}\frac{u}{||\mathbf{u}||} - \frac{\tau}{\rho h}\frac{v}{||\mathbf{u}||}\right) \tag{3}$$

where θ_z is the horizontal azimuth of the local ground slope, α. The source acceleration terms a_w and a_p are first used to define a first order approximation of velocity. From these terms the algorithm then calculates the retarding acceleration, a_r, in the direction opposed to this velocity. The advection terms are then computed using an upwind scheme to calculate the fluxes of mass and momentum, thereby generating a new estimate of the mean flow thickness and velocity at the centre of each cell (as detailed in the governing momentum equations in *Section 4.3.1*). Finally, a second upwind scheme is used to calculate the *x* and *y* components of the new velocities, *u* and *v*, at the cell edges as modified by advection.

Numerical implementation and model requirements

VolcFlow consists of a graphical user interface, an input file and a representation file. The user can load in topography, define variables and code erosion/sedimentation laws in a number of steering files; these parameters and their linked files are displayed in the user interface prior to running the model. The model can output a variety of data files at user-defined intervals, which are displayed using the representation file.

VolcFlow requires a path and a source topography file, both of which are gridded using kriging interpolation at 25 m spacing. In addition to the input topography files, the user is required to define a series of variables in the input .m file, including: rheology, unit weight, internal friction angle, basal friction angle, cohesion, material density, collisional stress, viscosity and curvature. A

series of control parameters may also be defined and adjusted, which include: the choice of a single or double upwind scheme, whether or not the path morphology is recalculated at each time step (to be used in conjunction with erosion/sedimentation laws), the maximum simulation time, time step and slide margin cut-off velocity. The model calculates the depth and velocity of the flow and its position at each time step based on the model spatial discretisation. These outputs are saved in a file that is run through a Reader, which populates multidimensional arrays of the variables required for analysis and saves them for later analysis.

Appendix C

Scheme for *VolcFlow* calibration

VolcFlow model calibration

Inputs

Boundary conditions
Section 5.1.1

Path topography (P)
Source depth (S)

1. Downsample pre- and post-event DEMs to 25 m (cubic convolution).
2. Clip to size.
3. Calculate DEM of difference.
4. Mask area of erosion (= source depth, S).
   4i. Convert source depths from vertical to normal.
   4ii. Subtract area of erosion from pre-event DEM to create path topography (P).
5. Mask area of deposition.
   5i. Smooth using 5x5 moving average filter (= observed deposit, D).
6. Grid S, P and D using kriging with 25 m spacing.
7. Save S and P for input and D for comparison with modelled deposits.

Mechanical behaviour
Section 5.1.2

Rheology

1. Select rheology to be modelled:
   1i. Coulomb frictional (1 angle).
   1ii. Coulomb frictional (2 angles).
   1iii. Voellmy.
   1iv. Plastic.
   1v. Plastic + u^2.
2. Adjust ϕ_{bed}, ϕ_{int}, T_0, and ξ accordingly.

Control parameters

1. Set time step (0.02 s).
2. Set plotting step (1 s).
3. Set max. simulation time (variable).
4. Enable en masse sliding.

Run VolcFlow
Section 5.1.2

Output .dat file

Run reader file — Calculates the following for each timestep:
1. Depth (min., mean, max.),
2. Velocity (min., mean, max.),
3. Centre of mass.
Outputs .mat file.

Final outputs

1. Max. run-out
2. Max. flow velocity
3. Duration
4. Max. depth
5. Lateral extent
6. Surface area
7. Hypsometric curves
8. COM displacement
9. Average flow velocity
10. Average deposit thickness
11. Min. velocity of slide through bypass zone

Validation
Section 5.1.3

Comparison with observed characteristics

1. Calculate % difference between observed and modelled deposit characteristics.
2. Plot and compare hypsometric curves for modelled deposits with D.
3. Plot and compare cross-sections for modelled deposits with D.
4. Rank all simulations in order of best-fit to observed deposit.

Select best rheological parameters

Appendix D

Conversion from vertical to normal source depths

Source depths were converted from vertical (h_v) to normal (h_n) depths by first calculating the gradient of the four nearest neighbours of each cell in the path topography DEM (z). In a three-dimensional Cartesian coordinate system, the gradient, ∇F, is a vector field whose components are the partial derivatives of F:

$$\nabla F = \frac{\partial F}{\partial x}\,\hat{\imath} + \frac{\partial F}{\partial y}\,\hat{\jmath} + \frac{\partial F}{\partial z}\,\hat{k} \qquad [4]$$

where $\hat{\imath}$, $\hat{\jmath}$, and $\hat{k}$, are the unit x-,y- and z-vectors, respectively. The rate of change of the surface in the horizontal and the vertical directions from the centre cell defines the slope, α, which is calculated as follows:

$$\alpha = \tan^{-1} \nabla F \qquad [5]$$

The source depth normal to the ground is then calculated using the cosine of the local slope:

$$h_n = h_v \cos \alpha \qquad [6]$$

Appendix E

'En masse sliding' using *VolcFlow*

If *lA* is defined (e.g. *lA*>0 in the input .m file) the mass is initially forced to slide as a block before its cohesion then decreases in time following an exponential law. This capability was enabled in *Chapter 5* for the purpose of simulating the early sliding phase of the rock avalanche. To simulate this, *VolcFlow* first calculates the velocity of each cell, *v*, independently. The mean velocity, v_m, weighted by the thickness of the flow, *h*, is then calculated:

$$v_m = \frac{\Sigma(vh)}{\Sigma h}$$ [7]

Finally, the new velocity of each cell, v_n, is calculated by its previous velocity and the mean velocity of the flow:

$$v_n = v(1 - A) + (v_m A)$$ [8]

Where *A* is defined by:

$$A = e^{\left(\frac{-t}{lA}\right)}$$ [9]

This allows a decrease of coherency with time (*t*), following an exponential law. In the simulations run in *Chapter 5*, a value of *lA* = 1 was used.

Appendix F

Scheme for defining source conditions and application to other cases (3D)

Application to other cases (3D)

Inputs

Boundary conditions
Section 5.2.1

Mechanical behaviour

Path topography (P)
Source depth (S)

Rheology

1. Calculate volume of event using volume-area scaling.
2. Clip 25 m post-event DEM to size.
3. Adjust DEM contours to simulate pre-event topography (= path topography, P; assume pre-event topography is similar to adjacent topography at present).
4. Use cut-fill to check that deposit volume is close to that given by volume-area scaling.
5. Calculate DEM of difference.
6. Mask area of erosion (= source depth, S).
   6i. Convert source depths from vertical to normal.
7. Mask area of deposition.
   7i. Smooth using 5x5 moving average filter (= observed deposit, D).
8. Grid S, P and D using kriging with 25 m spacing.
9. Save S and P for input and D for comparison with modelled deposits.

1. Select calibrated rheology:
   1i. Plastic + u^2.
2. Adjust T_0 (250 kPa) and ξ (0.01) accordingly.

Control parameters

1. Set time step (0.02 s).
2. Set plotting step (1 s).
3. Set max. simulation time (variable).
4. Enable en masse sliding.

Run VolcFlow
Section 5.2.2

Output .dat file

Run reader file —— Calculates the following for each timestep:
1. Depth (min., mean, max.),
2. Velocity (min., mean, max.),
3. Centre of mass.
Outputs .mat file.

Final outputs

1. Max. run-out
2. Max. flow velocity
3. Duration
4. Max. depth
5. Lateral extent
6. Surface area
7. Hypsometric curves
8. COM displacement
9. Average flow velocity
10. Average deposit thickness
11. Min. velocity of slide through bypass zone

Validation
Section 5.2.2

Comparison with observed characteristics

1. Calculate % difference between observed and modelled deposit characteristics.
2. Plot and compare hypsometric curves for modelled deposits with D.
3. Plot and compare cross-sections for modelled deposits with D.
4. Plot and compare observed vs. modelled outputs.

Sensitivity analysis
Section 5.3

Appendix G

Scheme for defining source conditions and application to other cases (contour-parallel 3D)

Application to other cases (contour-parallel 3D)

Inputs

Boundary conditions
Section 5.2.1

Path topography (P)
Source depth (S)

1. Calculate volume of event using volume-area scaling.
2. Clip 25 m post-event DEM to size.
3. Extract pre-event elevation profile at 25 m spacing (assume that pre-event topography is similar to adjacent topography at present).
4. Grid path topography (P) using 25 m spacing in the X and Y directions and the pre-event elevation profile as Z.
5. Measure surface area of the scar.
6. Divide volume by scar surface area to obtain an average thickness of the initial sliding mass.
7. Grid source depths (S) using kriging with 25 m spacing and place source mass in grid cells that correspond to the observed scar elevations in the P grid.
8. Save S and P for input.

Mechanical behaviour

Rheology

1. Select calibrated rheology:
   1i. Plastic + u^2.
2. Adjust T_0 (250 kPa) and ξ (0.01) accordingly.

Control parameters

1. Set time step (0.02 s).
2. Set plotting step (1 s).
3. Set max. simulation time (variable).
4. Enable en masse sliding.

Run VolcFlow
Section 5.2.2

Output .dat file

Run reader file ——— Calculates the following for each timestep:
1. Depth (min., mean, max.),
2. Velocity (min., mean, max.),
3. Centre of mass.
Outputs .mat file.

Final outputs

1. Max. run-out   4. Lateral extent
2. Max. flow velocity   5. Surface area
3. Max. depth   6. H/L

Validation
Section 5.2.2

Comparison with observed characteristics

1. Calculate % difference between observed and modelled deposit characteristics.
2. Plot and compare observed vs. modelled outputs.

Sensitivity analysis
Section 5.3

Appendix H – Rock avalanche characteristics in Vaigat: measurements and errors

Observed geometric characteristics associated with each event. Deposit volumes were calculated using the volume-area scaling detailed in *Section 5.2.1.1*. Run-out, lateral extent at the toe, total vertical drop height (H) and the apparent coefficient of friction (H/L) were all measured as defined in *Chapter 3*. The concavity index for each event represents the ratio between the integral of a longitudinal profile of the path topography and a straight line fit through that topography, indicating relative concavity. The approximate angle of each drop zone was measured by masking and averaging the slope map of the scar in question.

Event	Notes	Deposit								
		Surface area (A; m²)	Error (m²)	Volume (lower; m³)	Volume (V; m³)	Volume (upper; m³)	Run-out (L; m)	Error (m)	Lateral extent (m)	Error (m)
1	Paatuut (AD 2000) – tsunamigenic	4,138,971	± 433,750	79,739,992	94,144,204	109,324,391	4,383	± 100	1,325	±100
2	Stalls above bench (1)	997,500	± 117,702	9,226,338	11,138,440	13,166,956	2,084	± 100	312	±100
3	Stalls above bench (2)	1,577,271	± 180,067	18,464,805	22,146,972	26,045,802	1,927	± 100	674	±100
4	Stalls at bench (elevation 330-350 m asl)	1,930,000	± 180,817	25,864,734	29,977,193	34,287,101	2,843	± 100	650	±100
5	Stalls above bench (3)	735,941	± 143,870	5,093,488	7,058,614	9,226,549	1,740	± 100	440	±100
6	Superimposed onto alluvial fan (1)	650,626	± 132,737	4,166,869	5,867,483	7,751,740	1,501	± 100	1,070	±100
7	Superimposed onto alluvial fan (2)	669,057	± 124,869	4,488,266	6,118,564	7,909,055	1,270	± 100	618	±100
8	Runs out to sea level (1)	1,037,008	± 170,558	9,017,166	11,806,682	14,836,141	2,340	± 100	396	±100
9	Runs out to sea level (2)	1,294,899	± 167,066	13,391,275	16,474,363	19,763,339	2,416	± 100	958	±100
10	Tupasaat – stalls above alluvial fan (1)	603,125	± 104,405	3,937,681	5,236,800	6,653,836	1,821	± 100	736	±100
11	Tupasaat – stalls above alluvial fan (2)	504,392	± 103,261	2,840,436	4,005,045	5,295,882	1,848	± 100	180	±100
12	Tupasaat – stalls above alluvial fan (3)	739,482	± 136,741	5,231,801	7,109,620	9,170,160	1,995	± 100	233	±100
13	Tupasaat – long run-out, stalls above alluvial fan	2,424,193	± 257,394	35,660,133	42,199,354	49,095,632	3,710	± 100	370	±100
14	Tupasaat – runs out to sea level	2,095,625	± 193,438	29,331,545	33,917,619	38,720,551	3,196	± 100	921	±100
15	Adjoining to (14) – stalls at bench	964,611	± 173,173	7,871,913	10,592,135	13,568,915	2,107	± 100	279	±100
16	1952 event – tsunamigenic	1,408,750	± 143,489	15,912,022	18,694,158	21,621,845	2,345	± 100	1,028	±100
17	Small event – stalls at bench (1)	405,274	± 85,974	2,017,221	2,884,546	3,849,506	1,313	± 100	281	±100
18	Small event – stalls at bench (2)	397,689	± 95,588	1,856,449	2,803,950	3,873,390	1,550	± 100	122	±100
19	Runs out to sea level	1,477,118	± 312,520	14,051,388	20,071,407	26,767,186	3,129	± 100	1,214	±100
20	Stalls at bench - channelised	633,119	± 108,068	4,253,606	5,632,259	7,134,213	2,320	± 100	113	±100

Event	Notes	Deposit						Scar		
		H (m)	Error (m)	*H/L* (lower)	*H/L* (-)	*H/L* (upper)	Concavity Index (-)	Drop zone angle (°)	Surface area (m²)	Error (m²)
1	Paatuut (AD 2000) – tsunamigenic	1,466	± 18	0.32	0.33	0.34	0.71	61	411,202	± 113,856
2	Stalls above bench (1)	965	± 18	0.43	0.46	0.50	0.95	70	224,876	± 47,594
3	Stalls above bench (2)	965	± 18	0.47	0.50	0.54	0.91	69	284,041	± 77,353
4	Stalls at bench (elevation 330-350 m asl)	1,095	± 18	0.37	0.39	0.41	0.77	75	98,912	± 50,554
5	Stalls above bench (3)	861	± 18	0.46	0.49	0.54	0.82	67	94,189	± 38,019
6	Superimposed onto alluvial fan (1)	627	± 18	0.38	0.42	0.46	0.95	48	95,982	± 43,872
7	Superimposed onto alluvial fan (2)	406	± 18	0.28	0.32	0.36	0.91	43	54,971	± 41,250
8	Runs out to sea level (1)	994	± 18	0.40	0.42	0.45	0.79	46	118,493	± 42,281
9	Runs out to sea level (2)	969	± 18	0.38	0.40	0.43	0.74	53	201,107	± 57,097
10	Tupasaat – stalls above alluvial fan (1)	840	± 18	0.43	0.46	0.50	0.73	72	224,866	± 40,968
11	Tupasaat – stalls above alluvial fan (2)	811	± 18	0.41	0.44	0.47	0.88	40	74,052	± 40,888
12	Tupasaat – stalls above alluvial fan (3)	658	± 18	0.31	0.33	0.36	0.86	35	74,507	± 35,022
13	Tupasaat – long run-out, stalls above alluvial fan	1,241	± 18	0.32	0.33	0.35	0.73	48	655,043	± 77,816
14	Tupasaat – runs out to sea level	1,278	± 18	0.38	0.40	0.42	0.62	56	248,756	± 66,524
15	Adjoining to (14) – stalls at bench	1,190	± 18	0.53	0.56	0.60	0.82	56	226,836	± 75,803
16	1952 event – tsunamigenic	1,128	± 18	0.45	0.48	0.51	0.79	77	113,556	± 50,470
17	Small event – stalls at bench (1)	966	± 18	0.67	0.74	0.81	0.82	62	164,577	± 51,672
18	Small event – stalls at bench (2)	977	± 18	0.58	0.63	0.69	0.76	66	157,404	± 51,032
19	Runs out to sea level	1,453	± 18	0.44	0.46	0.49	0.61	57	171,469	± 53,454
20	Stalls at bench - channelised	1,328	± 18	0.54	0.57	0.61	0.58	55	62,402	± 39,090

Surface areas

Error

The error for each surface area measurement was calculated by measuring the perimeter of the corresponding shapefile and then multiplying this by 25 m (cell resolution of the GIMP DEM; Howat *et al.*, 2014).

Volume

Error

Deposit volumes were calculated using the following volume-area scaling, which was detailed in *Section 5.2.1.1*:

$$V = 0.05A^{1.5} \tag{10}$$

This has been successfully applied for bedrock landslides in a number of settings (after Hovius *et al.*, 1997; Malamud *et al.*, 2004; Larsen *et al.*, 2010). Lower and upper bounds for the estimated deposit volumes were then derived using the corresponding estimates for surface area.

Run-out and lateral extent

Error

The maximum horizontal measurement error for any given point on the 25 m GIMP DEM is 50 m. Given that both the run-out and lateral extent of a deposit is measured between two points, this gives both characteristics an overall measurement error of ±100 m.

Total vertical drop height

Error

The error of total vertical drop height measurements was simply calculated by assuming an error of ±9.1 m (overall RMS error of the GIMP DEM; Howat *et al.*, 2014) for both the height as measured from the crest of the pre-failure rock mass to the height at the lowest point of its reach (= ±18 m).

Apparent coefficient of friction

Error

Lower and upper bounds for the estimated apparent coefficient of friction (*H/L*) were derived by using the corresponding estimates for total vertical drop height (*H*) and run-out (*L*).

Appendix I – *VolcFlow* calibration: simulation results

Simulations performed using a Coulomb frictional rheology (one equation), with en masse sliding enabled. All model runs were performed assuming a density of 2850 kg m^{-3} and with a time step of 0.02 s, a plotting step of 1.0 s and a maximum simulation time of 200 s. ***** = Flowed out of domain space.

Coulomb frictional – 1 angle (ϕ_{bed})

Input parameters								
Basal friction angle, ϕ_{bed} (°)	20	19	18	17	16	15	14	13*
Model outputs								
Max. run-out (m)	**3,096**	**3,328**	**3,585**	**3,821**	**4061**	**4,250**	**4,503**	**4,750**
	(-29%)	(-24%)	(-18%)	(-13%)	(-7%)	(-3%)	(+3%)	(+8%)
Max. flow velocity (m s^{-1})	**72**	**76**	**78**	**82**	**85**	**87**	**89**	**97**
	(+29%)	(+36%)	(+39%)	(+46%)	(+52%)	(+55%)	(+59%)	(+73%)
Duration of emplacement (s)	**148**	**154**	**159**	**164**	**172**	**177**	**184**	**192**
	(+85%)	(+93%)	(+99%)	(+105%)	(+115%)	(+121%)	(+130%)	(+140%)
Max. deposit thickness (m)	**167**	**156**	**142**	**127**	**111**	**109**	**106**	**90**
	(+178%)	(+160%)	(+137%)	(+112%)	(+85%)	(+82%)	(+77%)	(+50%)
Lateral extent at toe (m)	**87**	**152**	**193**	**536**	**891**	**1,138**	**1,353**	**1,593**
	(-93%)	(-89%)	(-85%)	(-60%)	(-33%)	(-14%)	(+2%)	(+20%)
Surface area (m^2)	**2,172,500**	**2,413,750**	**2,742,500**	**3,378,750**	**4,186,875**	**4,865,625**	**5,579,375**	**6,151,250**
	(-48%)	(-42%)	(-34%)	(-18%)	(+1%)	(+18%)	(+35%)	(+49%)
Hypsometric integral (-)	**0.201**	**0.189**	**0.178**	**0.165**	**0.164**	**0.141**	**0.138**	**0.153**
	(-14%)	(-20%)	(-24%)	(-30%)	(-30%)	(-40%)	(-41%)	(-35%)
X-displacement of the centre of mass (m)	**93**	**291**	**437**	**603**	**841**	**1,180**	**1,617**	**2,133**
	(-96%)	(-88%)	(-81%)	(-74%)	(-64%)	(-50%)	(-31%)	(-9%)
Average flow velocity (m s^{-1})	**12**	**13**	**14**	**16**	**19**	**21**	**25**	**28**
	(-68%)	(-65%)	(-62%)	(-57%)	(-49%)	(-43%)	(-32%)	(-24%)
Average deposit thickness (m)	**34**	**30**	**25**	**21**	**18**	**16**	**15**	**14**
	(+89%)	(+67%)	(+39%)	(+17%)	(0%)	(-11%)	(-17%)	(-22%)

Simulations performed using a Coulomb frictional rheology (two equations), with en masse sliding enabled. All model runs were performed assuming a density of 2850 kg m^{-3} and with a time step of 0.02 s, a plotting step of 1.0 s and a maximum simulation time of 300 s.

Coulomb frictional – 2 angles (ϕ_{bed}, ϕ_{int})

Input parameters

Basal friction angle, ϕ_{bed} (°)	10	11	12	13	14	15	10	11	12	13	14	15
Internal friction angle, ϕ_{int} (°)	30	30	30	30	30	30	35	35	35	35	35	35

Model outputs

Max. run-out (m)	4,869	4,609	4,319	3,982	3,696	3,311	4,871	4,580	4,339	3,970	3,622	3,292
	(+11%)	(+5%)	(-2%)	(-9%)	(-16%)	(-25%)	(+11%)	(+5%)	(-1%)	(-9%)	(-17%)	(-25%)
Max. flow velocity (m s^{-1})	110	107	100	100	91	87	110	105	101	96	92	87
	(+96%)	(+91%)	(+79%)	(+79%)	(+63%)	(+55%)	(+96%)	(+88%)	(+80%)	(+71%)	(+64%)	(+55%)
Duration of emplacement (s)	300	274	249	240	218	198	295	282	268	247	222	202
	(+275%)	(+243%)	(+211%)	(+200%)	(+173%)	(+148%)	(+269%)	(+253%)	(+235%)	(+209%)	(+178%)	(+153%)
Max. deposit thickness (m)	73	94	111	112	125	129	88	103	113	119	123	127
	(+22%)	(+57%)	(+85%)	(+87%)	(+108%)	(+115%)	(+47%)	(+72%)	(+88%)	(+98%)	(+105%)	(+112%)
Lateral extent at toe (m)	1,618	1,271	984	933	344	153	1,755	1,234	873	553	226	104
	(+9%)	(-17%)	(-39%)	(-43%)	(-87%)	(-102%)	(+19%)	(-20%)	(-47%)	(-71%)	(-96%)	(-105%)
Surface area (m²)	6,121,875	5,523,750	4,155,625	4,059,375	2,479,375	2,206,875	6,245,000	5,285,000	4,014,375	2,974,375	2,482,500	2,251,875
	(+48%)	(+33%)	(+0.4%)	(-2%)	(-40%)	(-47%)	(+51%)	(+28%)	(-3%)	(-28%)	(-40%)	(-46%)
Hypsometric integral (-)	0.121	0.097	0.100	0.110	0.134	0.155	0.086	0.078	0.093	0.109	0.132	0.154
	(-49%)	(-59%)	(-57%)	(-53%)	(-43%)	(-34%)	(-63%)	(-67%)	(-60%)	(-54%)	(-44%)	(-34%)
X-displacement of the centre of mass (m)	1,615	832	308	290	69	48	1,040	447	193	106	79	61
	(-31%)	(-65%)	(-87%)	(-88%)	(-97%)	(-98%)	(-56%)	(-81%)	(-92%)	(-96%)	(-97%)	(-97%)
Average flow velocity (m s^{-1})	34	30	29	28	24	23	35	33	30	28	25	22
	(-8%)	(-19%)	(-22%)	(-24%)	(-35%)	(-38%)	(-5%)	(-11%)	(-19%)	(-24%)	(-32%)	(-41%)
Average deposit thickness (m)	10	10	11	12	17	20	6	8	11	13	16	19
	(-44%)	(-44%)	(-39%)	(-33%)	(-6%)	(+11%)	(-67%)	(-56%)	(-39%)	(-28%)	(-11%)	(+6%)

Simulations performed using a Voellmy rheology, with en masse sliding enabled. All model runs were performed assuming a density of 2850 kg m^{-3} and with a time step of 0.02 s, a plotting step of 1.0 s and a maximum simulation time of 300 s.

Voellmy (ϕ_{bed}, ξ)						
Input parameters						
Basal friction angle, ϕ_{bed} (°)	13	12	11	15	14	13
Collisional stress coefficient, ξ (-)	0.1	0.1	0.1	0.01	0.01	0.01
Model outputs						
Max. run-out (m)	**3,564**	**3,874**	**4,180**	**3,665**	**3,850**	**4,134**
	(-19%)	(-12%)	(-5%)	(-16%)	(-12%)	(-6%)
Max. flow velocity (m s^{-1})	**32**	**34**	**36**	**44**	**46**	**48**
	(-43%)	(-39%)	(-36%)	(-21%)	(-18%)	(-14%)
Duration of emplacement (s)	**223**	**245**	**271**	**194**	**223**	**243**
	(+179%)	(+206%)	(+239%)	(+143%)	(+179%)	(+204%)
Max. deposit thickness (m)	**113**	**100**	**83**	**121**	**120**	**110**
	(+88%)	(+67%)	(+38%)	(+102%)	(+100%)	(+83%)
Lateral extent at toe (m)	**1,073**	**1,442**	**1,811**	**992**	**1,250**	**1,546**
	(-19%)	(+9%)	(+37%)	(-25%)	(-6%)	(+17%)
Surface area (m^2)	**4,127,500**	**4,719,375**	**5,083,125**	**3,858,750**	**4,329,375**	**4,898,750**
	(-0.3%)	(+14%)	(+23%)	(-7%)	(+5%)	(+18%)
Hypsometric integral (-)	**0.170**	**0.171**	**0.195**	**0.170**	**0.153**	**0.150**
	(-28%)	(-27%)	(-17%)	(-28%)	(-35%)	(-36%)
X-displacement of the centre of mass (m)	**1,398**	**1,784**	**2,188**	**1,056**	**1,429**	**1,885**
	(-41%)	(-24%)	(-7%)	(-55%)	(-39%)	(-20%)
Average flow velocity (m s^{-1})	**5**	**5**	**5**	**5**	**6**	**7**
	(-86%)	(-86%)	(-86%)	(-86%)	(-84%)	(-81%)
Average deposit thickness (m)	**19**	**17**	**16**	**21**	**18**	**16**
	(+6%)	(-6%)	(-11%)	(+17%)	(0%)	(-11%)

Simulations performed using a plastic rheology, with en masse sliding enabled. All model runs were performed assuming a density of 2850 kg m^{-3} and with a time step of 0.02 s, a plotting step of 1.0 s and a maximum simulation time of 130 s.

Plastic (T_0)

Input parameters						
Cohesion (kPa)	235	260	265	270	275	300
Model outputs						
Max. run-out (m)	**4,725**	**4,391**	**4,378**	**4,334**	**4,264**	**3,978**
	(+8%)	(+0.2%)	(-0.1%)	(-1%)	(-3%)	(-9%)
Max. flow velocity (m s^{-1})	**79**	**74**	**73**	**72**	**71**	**66**
	(+41%)	(+32%)	(+30%)	(+29%)	(+27%)	(+18%)
Duration of emplacement (s)	**107**	**96**	**92**	**87**	**84**	**82**
	(+34%)	(+20%)	(+15%)	(+9%)	(+5%)	(+3%)
Max. deposit thickness (m)	**63**	**68**	**69**	**71**	**73**	**78**
	(+5%)	(+13%)	(+15%)	(+18%)	(+22%)	(+30%)
Lateral extent at toe (m)	**1,103**	**878**	**846**	**821**	**807**	**759**
	(-17%)	(-34%)	(-36%)	(-38%)	(-39%)	(-43%)
Surface area (m^2)	**5,349,375**	**4,766,875**	**4,664,375**	**4,563,125**	**4,458,750**	**4,009,375**
	(+29%)	(+15%)	(+13%)	(+10%)	(+8%)	(-3%)
Hypsometric integral (-)	**0.264**	**0.275**	**0.276**	**0.272**	**0.270**	**0.279**
	(+12%)	(+17%)	(+17%)	(+16%)	(+15%)	(+19%)
X-displacement of the centre of mass (m)	**2,065**	**1,777**	**1,743**	**1,694**	**1,642**	**1,430**
	(-12%)	(-24%)	(-26%)	(-28%)	(-30%)	(-39%)
Average flow velocity (m s^{-1})	**10**	**10**	**10**	**10**	**10**	**7**
	(-73%)	(-73%)	(-73%)	(-73%)	(-73%)	(-81%)
Average deposit thickness (m)	**17**	**18**	**19**	**19**	**20**	**22**
	(-6%)	(0%)	(+6%)	(+6%)	(+11%)	(+22%)

Simulations performed using a plastic rheology with a velocity-dependent law, with en masse sliding enabled. All model runs were performed assuming a density of 2850 kg m^{-3} and with a time step of 0.02 s, a plotting step of 1.0 s and a maximum simulation time of 110 s.

Plastic with a velocity-dependent law (T_0, ξ)

Input parameters

Cohesion (kPa)	250	255	260	250	255	260	200	210	220
Collisional stress coefficient, ξ (-)	0.01	0.01	0.01	0.005	0.005	0.005	0.05	0.05	0.05

Model outputs

Max. run-out (m)	4,368	4,340	4,216	4,387	4,345	4,306	4,260	4,061	3,922
	(-0.3%)	(-1%)	(-4%)	(+0.1%)	(-1%)	(-2%)	(-3%)	(-7%)	(-11%)
Max. flow velocity (m s^{-1})	66	65	64	69	68	67	56	56	55
	(+18%)	(+16%)	(+14%)	(+23%)	(+21%)	(+20%)	(0%)	(0%)	(-2%)
Duration of emplacement (s)	92	89	86	94	90	87	103	98	90
	(+15%)	(+11%)	(+8%)	(+18%)	(+13%)	(+9%)	(+29%)	(+23%)	(+13%)
Max. deposit thickness (m)	72	74	76	66	69	70	74	75	77
	(+20%)	(+23%)	(+27%)	(+10%)	(+15%)	(+17%)	(+23%)	(+25%)	(+28%)
Lateral extent at toe (m)	1,101	1,042	1,005	1,120	1,064	1,020	1,142	965	944
	(-17%)	(-21%)	(-24%)	(-15%)	(-20%)	(-23%)	(-14%)	(-27%)	(-29%)
Surface area (m^2)	4,545,000	4,211,250	4,005,000	4,309,375	4,238,750	4,156,875	4,247,500	4,076,250	3,833,125
	(+10%)	(+2%)	(-3%)	(+4%)	(+2%)	(+0.4%)	(+3%)	(-2%)	(-7%)
Hypsometric integral (-)	0.269	0.268	0.264	0.273	0.271	0.268	0.244	0.242	0.238
	(+14%)	(+14%)	(+12%)	(+16%)	(+15%)	(+14%)	(+4%)	(+3%)	(+1%)
X-displacement of the centre of mass (m)	1,776	1,730	1,627	1,808	1,781	1,720	1,823	1,745	1,683
	(-25%)	(-26%)	(-31%)	(-23%)	(-24%)	(-27%)	(-23%)	(-26%)	(-29%)
Average flow velocity (m s^{-1})	19	19	19	20	19	19	16	16	17
	(-49%)	(-49%)	(-49%)	(-46%)	(-49%)	(-49%)	(-57%)	(-57%)	(-54%)
Average deposit thickness (m)	19	20	20	18	19	19	19	19	20
	(+6%)	(+11%)	(+11%)	(0%)	(+6%)	(+6%)	(+6%)	(+6%)	(+11%)

Appendix J

Simulation results for all cases

Results of the simulations performed for all 20 cases. All model runs were performed using the best-fit rheological calibration obtained in *Section 5.1*. Numbers in brackets represent the normalised index, Δ, which compares the modelled and observed measurement for each output.

Event	Max. run-out (m)		H/L (-)		Lateral extent (m)		Surface area (m²)	
	Observed	**Modelled**	**Observed**	**Modelled**	**Observed**	**Modelled**	**Observed**	**Modelled**
1	4,383	4,368	0.33	0.32	1,325	1,101	4,139,000	4,545,000
	-	(-0.3%)	-	(-3%)	-	(-17%)	-	(+10%)
2	2,084	2,060	0.46	0.46	312	241	998,000	1,120,625
	-	(-1%)	-	(0%)	-	(-23%)	-	(+12%)
3	1,927	1,894	0.50	0.36	674	629	1,577,000	1,928,750
	-	(-2%)	-	(-28%)	-	(-7%)	-	(+22%)
4	2,843	2,829	0.39	0.36	650	702	1,930,000	2,233,125
	-	(-0.5%)	-	(-8%)	-	(+8%)	-	(+16%)
5	1,740	1,691	0.49	0.44	440	422	736,000	1,084,375
	-	(-2%)	-	(-10%)	-	(-4%)	-	(+47%)
6	1,501	1,125	0.42	0.31	1,070	491	651,000	503,750
	-	(-25%)	-	(-26%)	-	(-54%)	-	(-23%)
7	1,270	1,013	0.32	0.31	618	435	669,000	721,250
	-	(-20%)	-	(-3%)	-	(-29%)	-	(+8%)
8	2,340	2,191	0.42	0.39	396	339	1,037,000	1,360,000
	-	(-6%)	-	(-5%)	-	(-14%)	-	(+31%)
9	2,416	2,357	0.40	0.39	958	821	1,295,000	1,960,768
	-	(-2%)	-	(-3%)	-	(-14%)	-	(+51%)
10	1,821	1,643	0.46	0.44	736	716	603,000	804,375
	-	(-9%)	-	(-4%)	-	(-3%)	-	(+33%)
11	1,848	1,516	0.44	0.43	180	237	504,000	565,000
	-	(-18%)	-	(-2%)	-	(+32%)	-	(+12%)
12	1,995	1,530	0.33	0.39	233	368	739,000	885,000
	-	(-23%)	-	(+18%)	-	(+58%)	-	(+20%)
13	3,710	3,670	0.33	0.31	370	541	2,424,000	3,722,500
	-	(-1%)	-	(-6%)	-	(+46%)	-	(+53%)
14	3,196	3,123	0.40	0.39	921	889	2,096,000	2,294,375
	-	(-2%)	-	(-3%)	-	(-4%)	-	(+9%)
15	2,107	2,080	0.56	0.46	279	287	965,000	1,333,125
	-	(-1%)	-	(-18%)	-	(+3%)	-	(+38%)
16	2,345	2,299	0.48	0.49	1,028	1,055	1,409,000	1,773,125
	-	(-2%)	-	(+2%)	-	(+3%)	-	(+26%)
17	1,313	1,135	0.74	0.75	281	243	405,000	427,500
	-	(-14%)	-	(+1%)	-	(-14%)	-	(+5%)
18	1,550	1,328	0.63	0.64	122	134	398,000	497,500
	-	(-14%)	-	(+2%)	-	(+10%)	-	(+25%)
19	3,129	2,988	0.46	0.46	1,214	1,097	1,477,000	2,305,800
	-	(-4%)	-	(0%)	-	(-10%)	-	(+56%)
20	2,320	2,038	0.57	0.58	113	212	633,000	1,156,250
	-	(-12%)	-	(+2%)	-	(+88%)	-	(+83%)

Appendix K

Regressions

Presented below are the results and associated diagnostics for a number of regression models fit throughout this work.

Summary of diagnostics for Reduced Major Axis Regressions fit to observed versus modelled values of rock avalanche run-out, *H/L*, lateral extent at toe and surface area, for all 20 cases (Fig. 6.11). Source data are found in *Appendix J*.

Run-out (observed vs. modelled)	Reduced major axis regression - estimated coefficients			
	Estimate	**SE**	***t* statistic**	***p* value**
Intercept	-357.26 m	83.654 m	-4.0106	0.00082031
x1	1.0913 m	0.0345 m	31.404	3.5713×10^{-17}
	RMSE	**R²**	$\bar{x}$	$\bar{y}$
	121 m	0.991	2292 m	2144 m

H/L (observed vs. modelled)	Reduced major axis regression - estimated coefficients			
	Estimate	**SE**	***t* statistic**	***p* value**
Intercept	-0.0515	0.0489	-0.19564	0.84708
x1	1.0636	0.1045	9.5033	1.9446×10^{-8}
	RMSE	**R²**	$\bar{x}$	$\bar{y}$
	0.0477	0.913	0.4565	0.4340

Lateral extent (observed vs. modelled)	Reduced major axis regression - estimated coefficients			
	Estimate	**SE**	***t* statistic**	***p* value**
Intercept	58.015	56.9314	1.8132	0.086519
x1	0.8221	0.0811	9.4574	2.0927×10^{-8}
	RMSE	**R²**	$\bar{x}$	$\bar{y}$
	132	0.912	596	548

Surface area (observed vs. modelled)	Reduced major axis regression - estimated coefficients			
	Estimate	**SE**	***t* statistic**	***p* value**
Intercept	6.730×10^{4}	1.1460×10^{5}	1.0564	0.30477
x1	1.2103	0.0758	15.548	7.057×10^{-12}
	RMSE	**R²**	$\bar{x}$	$\bar{y}$
	2.95×10^{5}	0.965	1.234×10^{6}	1.561×10^{6}

Summary of diagnostics for a linear regression fit to the normalised index, Δ, of run-out ($\log_{10}$) versus volume ($\log_{10}$; Fig 6.12a). Source data is found in *Appendices H* and *J*.

Normalised index of run-out vs volume ($\log_{10}$)	Linear regression model ($y\sim1+x1$) estimated coefficients			
	Estimate	**SE**	**t statistic**	**p value**
Intercept	8.9645	1.2948	6.9233	1.8001×10^{-6}
x1	-1.1833	0.18321	-6.4586	4.4671×10^{-6}
	RMSE	**R^2**	**Adjusted R^2**	**F-statistic**
	0.326	0.699	0.682	41.7

Summary of diagnostics for a linear regression fit to the volume of material remaining stalled in the source area: total deposit volume ($\log_{10}$) against total deposit volume ($\log_{10}$; Fig. 6.12b). Source data is found in *Appendix L*.

Vol. in source area vs total deposit vol. ($\log_{10}$)	Linear regression model ($y\sim1+x1$) estimated coefficients			
	Estimate	**SE**	**t statistic**	**p value**
Intercept	5.8468	0.9048	6.462	4.4368×10^{-6}
x1	-0.69939	0.12803	-5.4629	3.4479×10^{-5}
	RMSE	**R^2**	**Adjusted R^2**	**F-statistic**
	0.228	0.624	0.603	3.45×10^{-5}

Appendix L

Volumetric data

Presented below are the source data for Fig. 6.12b. The volume of material stalled in the source area following each simulation was calculated using a mask of the scar. The ratio represents the ratio of this volume: total deposit volume.

Event	Volume (m^3)		
	Total	**Stalled in source**	**Ratio**
1	94,144,204	2,803,500	0.02978
2	11,138,440	601,875	0.05404
3	22,146,972	850,480	0.03840
4	29,977,193	1,291,250	0.04307
5	7,058,614	549,000	0.07778
6	5,867,483	1,619,500	0.27601
7	6,118,564	1,029,000	0.16818
8	11,806,682	643,730	0.05452
9	16,474,363	1,378,200	0.08366
10	5,236,800	328,600	0.06275
11	4,005,045	595,430	0.14867
12	7,109,620	633,680	0.08913
13	42,199,354	2,929,700	0.06943
14	33,917,619	940,625	0.02773
15	10,592,135	1,606,200	0.15164
16	18,694,158	604,375	0.03233
17	2,884,546	1,009,800	0.35007
18	2,803,950	1,391,300	0.49619
19	20,071,407	775,390	0.03863
20	5,632,259	423,150	0.07513